Planar nano-antennas for spectroscopy and sensing

DISSERTATION
zur Erlangung des Grades eines Doktors
der Naturwissenschaften

vorgelegt von

Dipl.-Ing. Navid Soltani

eingereicht bei der Naturwissenschaflich-Technischen Fakultät
der Universität Siegen

September 15, 2023

Tag der Mündliche Prüfung: 15.06.2023

Betreuer und Gutachter: Prof. Dr. Mario Agio

Gutachter: Prof. Dr. Stephan Götzinger

Prüfer 1: Prof. Dr. Holger Schönherr

Prüfer 2: Prof. Dr. Stefan Nimmrichter

Abstract

Molecular sensing and detection have been established over the past decades with biochemistry and medical diagnostics applications. Among the various sensing methods, fluorescence detection is considered to be one of the most promising ones, especially in vitro diagnostics. Dye molecules used as a label in fluorescence detection are generally dipolar light sources emitting in a random direction, and a significant fraction of the emitted photons can not reach the detectors. This dramatically reduces the brightness of the dye molecules. A practical approach to overcome this problem relies on enhanced light-matter interaction obtained using optical nano-antennas.

In this work, we investigate a planar antenna configuration, which beams the radiation pattern of the dye into a narrow cone. It mimics the operation of a Yagi–Uda antenna, where reflector and director elements are made of thin metal films. Here, the reflector element of the planar Yagi–Uda antenna is an etched flat gold wire, and the director element is made of 10 nm gold film evaporated on the glass coverslip. Our first goal is to elucidate the antenna effects when the reflector-director gap changes (scanning antenna). By scanning the reflector in the axial direction, the radiation pattern of a single fluorescent bead changes, and the emission narrows down to angles of 45° (full width at half maximum) at the antenna resonance. Afterward, we focus on detecting double-stranded DNA molecules labeled by fluorescent Atto-647N in a buffer to determine the sample concentration.

Moreover, a practical way to guide the fluorescence signal to a detector is through an optical fiber. By coating the director on the tip of an etched fiber and using a gold substrate as a reflector, we can direct the emission into the fiber with high efficiency. A numerical simulation has been developed to evaluate the coupling efficiency of a horizontally oriented dipole into a fiber. The result determines more than 70% coupling efficiency, which would only scale by a factor of 2/3 for emitters with a random orientation. This configuration can not only collect the emitted light but also excite the molecule through the same fiber. However, in practice, the fiber shows a high autofluorescence in excitation due to doping or defects in the core material, which needs further investigation. This method is a compact solution to enhance the sensitivity and dynamic range of molecules detection, and it can replace the bulk optics conventionally employed for fluorescence measurements.

Zusammenfassung

Die molekulare Sensorik und Detektion hat sich in den letzten Jahrzehnten mit Anwendungen in der Biochemie und der medizinischen Diagnostik etabliert. Unter den verschiedenen Sensormethoden ist die Fluoreszenzdetektion eine der vielversprechendsten, insbesondere für die In-vitro-Diagnostik. Farbstoffmoleküle, die als Markierung in der Fluoreszenzdetektion verwendet werden, sind im Allgemeinen dipolare Lichtquellen, die in zufälliger Richtung emittieren und ein großer Teil der emittierten Photonen kann die Detektoren nicht erreichen. Dadurch wird die Helligkeit der Farbstoffmoleküle drastisch reduziert. Ein effektiver Ansatz zur Überwindung dieses Problems beruht auf einer verbesserten Licht-Materie-Wechselwirkung, die mit optischen Nanoantennen erzielt wird.

In dieser Arbeit untersuchen wir eine planare Antennenkonfiguration, die das Strahl- ungsmuster des Farbstoffs in einem schmalen Kegel bündelt. Es ahmt den Betrieb der Yagi–Uda Antenne nach, bei der Reflektor- und Direktor aus dünnen Metallfilmen bestehen. Hier ist das Reflektorelement der planaren Yagi–Uda Antenne ein geätzter flacher Golddraht und das Direktorelement besteht aus einem 10-nm-Goldfilm, der auf das Deckglas aufgedampft ist. Unser erstes Ziel ist es, die Antenneneffekte bei Reflektor-Direktor Lückenänderungen (Scanning-Antenne) aufzuklären. Durch Abtasten des Reflektors in axialer Richtung ändert sich das Strahlungsmuster einer einzelnen Fluoreszenzbead, und die Emission verengt sich bei der Antennenresonanz auf einen Winkel von 45° (Halbwertsbreite). Anschließend konzentrieren wir uns auf den Nachweis von doppelsträngigen DNA-Molekülen, die mit fluoreszierendem Atto-647N in einem Puffer markiert sind, um die Probenkonzentration zu bestimmen.

Darüber hinaus ist die Verwendung einer optischen Faser ein praktischer Weg, um das Fluoreszenzsignal zu einem Detektor zu leiten. Indem wir den Direktor auf die Spitze einer geätzten Faser auftragen und ein Goldsubstrat als Reflektor verwenden, können wir die Emission mit hoher Effizienz in die Faser lenken. Eine numerische Simulation wurde entwickelt, um die Kopplungseffizienz eines horizontal ausgerichteten Dipols in eine Faser zu bewerten. Das Ergebnis ergibt über 70% Kopplungseffizienz, die bei Emittern mit zufälliger Ausrichtung nur um den Faktor 2/3 skalieren würde. Diese Konfiguration kann nicht nur das emittierte Licht sammeln, sondern auch das Molekül durch dieselbe Faser anregen. In der Praxis zeigt die Faser jedoch eine hohe Autofluoreszenz bei Anregung aufgrund von Dotierung oder Defekten in der atomaren Struktur des Kernmaterials, was weitere Untersuchungen erfordert. Dieses Verfahren ist eine kompakte Lösung, um die Empfindlichkeit und den dynamischen Bereich der Moleküldetektion zu verbessern und es kann die herkömmlich verwendete Bulk-Optik für Fluoreszenzmessungen ersetzen.

Acknowledgments

This work has been to a great extent the contribution of many peoples. First and foremost, I am deeply indebted to my supervisor Prof. Mario Agio for giving me this opportunity in his group and I thank him for his continuous support and advice. Also, I would like to express my gratitude to Dr. Nemanja Markešević and Dr. Assegid Mengistu Flatae for their devoted guidance, as well as to Elham Rabbany Esfahany, my colleague and friend, who worked closely with me and made significant contributions to many of the findings presented in this work. I am also thankful to Dr. Sergey I. Druzhinin and Prof. Holger Schönherr from the Physical Chemistry I group, as well as Dr. Julian Müller and Prof. Benjamin Butz from the Research Center of Micro- and Nanochemistry and (Bio)Technology (Cμ).

This work could not have been done without the laboratory expertise and guidance provided by Gregor Schulte and Dr. Rainer Bornemann. I am grateful that I have their support. I acknowledge stimulating discussions with Costanza Toninelli, Ambra Giannetti, Steffen Howitz, and Pietro Lombardi during the FASPEC project, which is an integral part of this dissertation. Furthermore, it is my honor that I collaborated with Florian Sledz, Ankur Das, and Philipp Reuschel, as well as Lukas Hunold, Amr Farrag, Lukas Strauch, and Haritha Kambalathmana as both colleagues and friends in the Laboratory of Nano-Optics group. I am deeply grateful to all of them for the enriching discussions and the positive environment that we fostered in the lab.

I would like to express my sincere gratitude to Prof. Dr. Stephan Götzinger for his invaluable contribution to this thesis through his meticulous reading and insightful comments, which have greatly enhanced the quality of my work.

Special thanks to Sharon Harvey for her exceptional administrative assistance and the considerable amount of time she devoted to supporting me. Additionally, I extend my heartfelt appreciation to the mechanical workshop team Uwe Krüger, Jörn Falke and Olaf Meyer for manufacturing the experimental components of the setup with high quality.

Friends are always the first port of call when help is needed. Special thanks to Pedram, Elham, Danial, Sam, Zohreh, Golnoush, and Pooria for their support. This journey without them would have been significantly more difficult. Most importantly, none of this would have been possible without love and patience of my parents, my brother Pouya and my partner Ava, who shared with me both the joys and challenges of these intense years, and for that, I am incredibly grateful. Lastly, I would like to dedicate this dissertation to Prof. Siamak Khademi, who not only enlightened me with the beauty of physics but also gave me the confidence to pursue knowledge.

Contents

Chapter 1

Introduction

Interest in materials at the nanoscale has rapidly increased in science and engineering due to their unique physical and chemical properties caused by their geometry. Although nano-physics is associated with modern science, artisans used nanoparticles as far back as the ninth century in Mesopotamia or the middle ages in Europa to create a glittering effect on the surface of pots and glasses [1].

The term "nanotechnology" was first used by Norio Taniguchi in a 1974 conference to describe thin film deposition and ion beam milling [2] and later by Kim Eric Drexler in his 1987 book Engines of Creation: The Coming Era of Nanotechnology [3]. The experimental research, however, took off in the early 1980s with the invention of the scanning tunneling microscope (STM) [4,5]. Later, the invention of carbon nanotubes in the 1990's [6] and nanoscale gate metal–oxide–semiconductor field-effect transistors (MOSFET) [7] introduced nanotechnology into industrial applications. Nowadays, nano-lithography, such as extreme ultraviolet (EUV) lithography and etching technology, can fabricate smaller and more complex structures for electronic and sensing applications. The international roadmap for devices and systems (IRDS) predicts the 2 nm process node (this mainly refers to the gate length of transistors) by 2024 [8]. Furthermore, nanotechnology has revolutionized the development of highly sensitive nanobiosensors by capitalizing on their significant surface-to-volume ratios and the diverse optical and electronic properties of nanostructured designs. These compact biosensors are promising analytical tools for diagnosing illnesses in their early stages. Fluorescence-based bioprobes are common examples of such sensors for the detection of biological and chemical agents [9].

With the advent of advanced nanoscale manufacturing, scientists applied well-established concepts in electronics and optics to the nanoscale [10,11]. A successful example of this transition is the optical nanoantenna [12,13]. Antennas have been used since the 1880s for transmitting or receiving electromagnetic waves at radio frequencies [14]. Metallic nanoparticles with their plasmon resonances can be used in the same fashion at optical frequencies [15]. Just as there are several types of antennas in electronics, nanoantennas also fall into several categories. The Yagi–Uda optical antenna is a directional antenna which radiates or receives high power in specific directions, with a similar working principle to the well-known Yagi–Uda antenna. Its structure contains a reflector, one or more directors, and a driving element (feed) between them [16]. The reflector and directors are usually made of metal rods with a length of approximately $\lambda/2$, where λ is the wavelength of the electromagnetic wave.

Optical antennas in the vicinity of fluorescent molecules can modify their spontaneous emission rates in a broad spectral range. Enhancing the emission rate is also an essential characteristic of microcavities, and one of the reasons for using them in sensing applications [17,18]. However, achieving a significant effect requires the creation of cavities with a high-quality factor (Q), which is challenging due to two fundamental issues. First, they are at least several micrometers in size because highly reflective surfaces are bulky. Second, high Q implies narrow resonances, dictating operation with very narrow-band emitters and the need for highly sensitive frequency tuning. The Yagi–Uda optical antenna can enhance the Purcell factor ($F \propto Q/V$) by confining the mode volume V to a broad spectrum [19, 20]. In general, the Yagi–Uda optical antenna exhibits both the beaming effect and emission rate modification characteristics at a compact size, making it a suitable candidate for lab-on-chip and sensing applications.

Despite these benefits, the fabrication of such an antenna is very challenging. The distance between the rods is in subwavelength (80-200 nm for visible light) due to the radiation penetration into metals [21], and their length is also a few hundred nanometers. In addition, placing the emitter between the reflector and director rods, where the electric field is high, makes applying Yagi–Uda optical antennas difficult. Therefore, a more straightforward approach is to use the nanoscale design only in one direction (e.g., the z direction) and use laterally infinite metal plates as the reflector and director. The lateral position of the dye is not critical in a planar geometry, and the axial direction can be controlled more easily. In 2017 S. Checcucci et al. [22] characterized the emission of a single dibenzoterrylene (DBT) molecule sandwiched between two reflector and director gold plates. This structure is known as the planar Yagi–Uda optical antenna. The gap between the reflector and the director was subwavelength. The director is a very thin metal layer (20 nm thick) and partially transparent at the working wavelength. The medium between the reflector and director plates is known as the active medium, made of dielectric materials. Since this structure has a planer surface, it is easier to stack different layers of materials on each other in order to apply the concept of single photon source generation [23] or biosensing applications [24].

The planar Yagi–Uda optical antenna is a new nanosensing concept, which requires further characterization. Therefore, the main goal of this work is to understand such an antenna based on the geometry (reflector-director gap) and material types, implementing a scanning approach. Furthermore, testing the planar Yagi–Uda antenna as a biodetector and finding its technical limitations is a practical approach to realizing the potential of such an antenna in modern diagnostics applications. This work is structured into seven chapters starting with theory followed by experimental results of a scanning planar Yagi–Uda antenna.

The second chapter briefly explains the essential characteristics and parameters of fluorescent detection and introduces three types of emitters. Chapter three focuses on the properties of optical antennas and their ability to modify and direct electromagnetic radiation. There, we introduce the planar Yagi–Uda antenna as an optical system for enhancing a dipole's emission rate and the collection efficiency of the system. Chapter four considers the theoretical and experimental results of detecting fluorescence molecules using a planar Yagi–Uda antenna. These show that the antenna beams the fluorescence emission of a single bead into a narrow cone down to an angle of 45° and enhances the collected signal by a factor of three compared to the case of a glass coverslip. In addition, we investigate the detection limit of the system for DNA-labeled fluorescent dye molecules embedded in a fluid. This characteristic determines the system's ability to detect molecules in a solution with low concentrations, emphasizing the biocompatibility aspect(down to 1 nM). Chapter five investigates the idea of applying a Yagi–Uda antenna on the tip of an optical fiber. The simulation of a practical setting reveals more than 70% coupling efficiency into the fiber for a horizontally oriented dipole with respect to the planar antenna. Moreover, in the same chapter, we highlight the challenges, such as antenna fabrication on the fiber tip and auto-fluorescence of the fiber. As an outlook in chapter six, we suggest ways to improve the fiber-based optical antenna system and use it as a lab-on-chip sensor for detecting fluorescent molecules down to the single molecule level. We summarize this work in the final chapter and discuss the potential applications of such a system in biophysics as well as quantum technology.

Chapter 2

Principles of fluorescence microscopy and spectroscopy

The radiation of light due to deexcitation of organic and inorganic specimens (fluorophores) is typically the result of a physical phenomenon termed luminescence. The relatively narrow spectrum of this radiation makes it distinguishable from background light. This property has made it useful in the detection of targeted molecules and has been a cornerstone of recent microscopy methods such as epifluorescence microscopy, confocal microscopy, and fluorescence lifetime imaging microscopy. One continuously expanding methodology in this century is the usage of fluorescence in biology and sensing to detect the delicate structures of biomolecules such as DNA sequences or antibodies. The combination of high-resolution microscopes and the narrow spectrum of fluorophores opens a broad field of research in cellular and molecular imaging down to the level of single-molecule detection.

This chapter describes the principle of fluorescence and its emission properties. It also briefly explains the energy levels and optical properties of single molecules and the radiation pattern in free space. Finally, the chapter presents three types of emitters commonly used in fluorescence measurements.

2.1 Absorption and emission of light

Fluorescence microscopy is a technique commonly used to detect molecules known as fluorophores interacting with light. They absorb energy at a specific wavelength and then re-emit it at a different wavelength, which depends on the emitter and the chemical environment around it. In an absorption process, an electron of an emitter gains energy and, as a result, moves to a higher energy level. When the excited electron in the higher energy level returns to the ground state, it emits a photon with an energy equal to the energy difference between the levels in accordance with energy-momentum conservation. Depending on the nature of the excited state, this decay is divided into two categories, fluorescence, and phosphorescence [25]. In excited singlet states, the excited electron is paired with a second electron in the ground state. Consequently, returning to the ground state is spin allowed and occurs rapidly by emission of a photon. This process is typically very fast and usually takes a few nanoseconds. The average time for the transition of electrons from an excited state to the ground state is called the lifetime (τ).

In contrast, phosphorescence originates from a weak optical transition, typically spin forbidden, which leads to lifetimes of the order of milliseconds to seconds.

Distinguishing between fluorescence and phosphorescence is not always straightforward. For example, transition metal–ligand complexes (MLCs), which contain a metal and one or more organic ligands, display mixed singlet–triplet states and show a lifetime of hundreds of nanoseconds to several microseconds. Although phosphorescence is a slower process, which can aid detection, it is also more susceptible to deactivation due to faster nonradiative decay or quenching. Therefore, we use fluorescence in our work, as it is a more sensitive method with a higher photon rate.

2.1.1 Jablonski diagram

Electrons in a ground state can gain energy (optically, electrically, or chemically) and move to an excited energy level. However, they lose their energy and decay into the ground state again after some time. The probability per unit time of a specific excited state decaying to a lower energy state by emission of a photon or by other means, such as collisional de-excitation, is defined as the decay rate. It is typically expressed as a decay constant, which is the reciprocal of the average lifetime of the excited state. Decay can be divided into radiative (electron de-excitation to ground state by releasing a photon) and non-radiative (electron de-excitation to ground state without releasing any photon). To illustrate the electronic states of a molecule and the transitions between them, one can use the Jablonski diagram.

The electronic ground state of a molecule is usually a singlet S_0 multiplicity (total spin quantum number equals zero). However, the excited states can be singlets S_i or triplets T_i, while the higher multiplicity (triplet) has the lower energy obeying the first Hund's rule [26]. Following the spin selection rule, the strongest optical transitions are singlet-singlet, e.g., $S_0 \longleftrightarrow S_1$. Triplet-singlet transitions are weakly allowed, hence much less probable. The process of transitioning from S_1 to T_1 and from T_1 to S_0 is commonly known as intersystem crossing, while the transition $T_1 \longrightarrow S_0$ is specifically referred to as phosphorescence (Fig. 2.1) [27].

The sublevels in Fig. 2.1 arise from the vibrational degrees of freedom, which affect the optical properties of a molecule. On exciting an electron to a higher

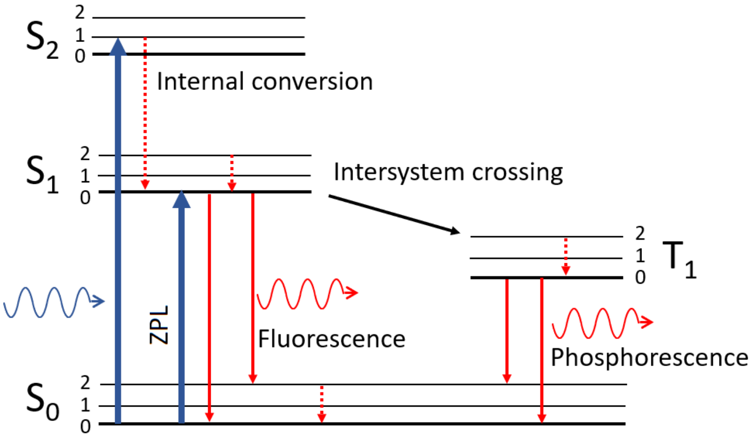

Figure 2.1: ***Jablonski diagram of fluorescence and phosphorescence.*** *Optical excitation of a single molecule from the ground state and the emission via singlet or triplet states is presented. The blue lines signify resonant excitation, whereas the red lines indicate the red-shifted emission. The dotted lines represent non-radiative decay.*

sublevel of an excited state, the electron can lose energy through fast nonradiative transitions. This internal conversion process can reduce the quantum yield, i.e., the ratio between the radiative and total decay rates [27]. Moreover, the vibrational transition causes broadening and asymmetry in the molecule spectrum.

2.1.2 Zero phonon line and molecular spectra

The probability of a transition from one eigenstate to another is commonly described by the transition strength. To a first approximation, transition strengths are governed by selection rules, which determine whether a transition is allowed or not. The transition between the zero vibrational level of the S_0 state of a molecule to zero vibration of S_1 level is called the zero phonon line (ZPL). The rotational degrees of freedom can be neglected for emitters embedded in a solid matrix. However, couplings with the delocalized vibrational excitations of the host lattice, the phonons, must be taken into account. The electron-phonon coupling can be reduced by cooling the system.

When an electron is excited from S_0 to S_1, the nuclear coordinate of the S_1 state shifts owing to the Coulomb force of the excited electron (so-called Frank-Condon shift). This shift is equal to Δ in the equilibrium position. Assuming the vibrational levels are harmonic and based on the Born-Oppenheimer approximation, the dipole matrix element M for an optical transition between the ground and excited states is given by:

$$M = \langle \Psi_f | \, \mathbf{r} \, | \Psi_i \rangle \, \langle \chi'_n | \chi_m \rangle \, , \tag{2.1}$$

where $\mathbf{r}$ is the electronic coordinate (an operator which connects the initial with the final state), $\Psi_{i,f}(\mathbf{r}, q)$ is the electronic wave function of ground and excited state, respectively and $\chi_m(q)$ and $\chi'_n(q)$ are harmonic oscillator wave functions [28]. The square of the first matrix element determines the overall strength of the transition, and the probability that it takes place between the vibrational levels m and n is thus proportional to $|\langle\chi'_n|\chi_m\rangle|^2$ (vibrational overlap integral), which corresponds to the Franck-Condon factor. If the vibrational overlap integral is zero for this transition, then the transition will not be observed, irrespective of the magnitude of the electronic factor. The transition energy is also equal to $S_1 + (n + 1/2)\hbar\omega' - (m + 1/2)\hbar\omega$ as it shown in Fig. 2.2.

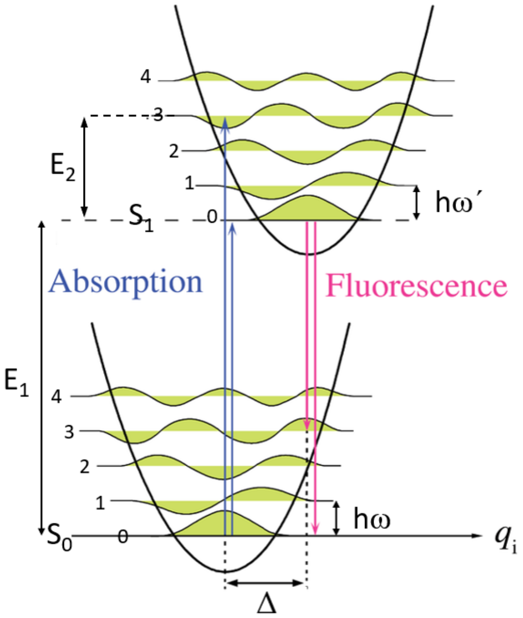

Figure 2.2: ***Energy levels of a single molecule as a function of the normalized nuclear coordinate.*** *Electronic transitions are faster than nuclear motions. Therefore vibrational levels are favored when they correspond to a minimal change in the nuclear coordinates. In the presence of linear electron-phonon coupling for a molecule, the emission spectrum acquires a phonon wing, with a central frequency shifted by Δ from the purely electronic transition at ω_0 [27].*

The spectra originating from a collection of identical molecules in a matrix are inhomogeneously broadened because each molecule is surrounded by a different matrix environment which modifies the energy required for an electronic transition. In an inhomogeneous distribution of molecules, individual ZPL and phonon sideband positions are therefore shifted and overlapping. Therefore, an ensemble molecule's absorption and emission spectrum is very broad.

Typically, the molecular energy levels do not have distinct energy levels far from neighboring levels. As a result, the width of the absorption band is usually several tens of nanometers. This is easy to explain, considering that a typical dye molecule is composed of several atoms, giving rise to multiple vibrations. In addition, when an electron is excited to a higher energy level, its density changes, which is associated with a change in bond length between atoms of the molecule. This couples more vibrations to the electronic transitions and causes increased spectrum broadening. An example of such a broad spectrum is shown for the ATTO-647N dye molecule in Fig.2.7. This molecule is used as a fluorescent label in this work.

On cooling the molecule to cryogenic temperatures, the spectral lines become extremely narrow. The Heisenberg uncertainty principle imposes the lower limit on the linewidth, which relates the excited state lifetime to the so-called natural or lifetime-limited linewidth $\Delta\nu$, which is of the order of a few MHz.

Solvent polarity and the local environment have profound effects on the emission spectral properties and quantum yield (Sec. 2.2) of the molecule. To understand the spectral shifts caused by a solvent, one can use the Lippert–Mataga equation:

$$\bar{\nu}_A - \bar{\nu}_F = \frac{2}{hc}\left(\frac{\epsilon - 1}{2\epsilon + 1} - \frac{n^2 - 1}{2n^2 + 1}\right)\frac{(\mu_E - \mu_G)^2}{a^3} + \text{constant}, \tag{2.2}$$

where $\bar{\nu}_A$ and $\bar{\nu}_F$ are the wavenumbers (cm^{-1}) of the absorption and emission, respectively. h is Planck's constant, c is the speed of light, ϵ is the dielectric constant, a is the radius of the cavity in which the molecule is embedded (it can be the size of the fluorophore), and μ_G and μ_E are the dipole in the ground and excited states, respectively.

The Lippert–Mataga equation is an approximation in which the polarizability of the fluorophore and higher-order terms are neglected. By increasing n the energy loss decreases, whereas an increase in ϵ results in a larger difference between $\bar{\nu}_A$ and $\bar{\nu}_F$ [25]. Calculating Eq. 2.2 for a fluorophore illustrates that the $\Delta\nu$ is very small. However, even in non-polar solvents, absorption and emission maxima are not very close. Excitation generally occurs at higher vibrational levels, and this energy is rapidly dissipated in fluid solvents. In contrast, emission occurs at an excited vibrational level of the ground state. As a result, absorption and emission are generally shifted by an amount at least equal to the vibrational energy, or about 650 cm^{-1}. These energy losses are represented by the constant term in Eq. 2.2. If the excitation takes place at 640 nm, then the emission is around 665 nm. Note that the Lippert–Mataga equation is based on the Franck–Condon principle and contains many assumptions, such as that the fluorophore under consideration is spherical and there is no consideration of specific interactions with the solvent. The Lippert–Mataga equation can estimate the fluorescence shift and potentially reveal the polarity of the fluorophore environment.

2.2 Quantum yield and lifetime

Important optical properties of fluorophores are their quantum yields and lifetimes. Quantum yield is the number of emitted photons relative to the number of absorbed photons, and it is calculated by:

$$\eta = \frac{\Gamma_{\text{rad}}}{\Gamma_{\text{tot}}}, \tag{2.3}$$

where Γ_{rad} is the emission rate of the fluorophore and Γ_{tot} is the summation of radiative and non-radiative decay to S_0 ($\Gamma_{\text{tot}} = \Gamma_{\text{rad}} + \Gamma_{\text{nrad}}$). Γ_{rad} and Γ_{nrad} are functions of the local environment and thus affected by inhomogeneities and environmental changes. This is described more in detail in Sec. 3.1. Due to the unavoidable non-radiative channels, the quantum yield of fluorescence is always less than unity.

To accurately determine the absolute quantum yield of a sample, an integrated or reflective sphere can be utilized. This sphere collects all the emitted light from the sample and directs it towards a spectrometer for analysis. This method necessitates the precise measurement of the emission spectrum as well as the absorbed number of photons.

The measurement of the absorbed photons involves two spectral scans. The first scan measures the Rayleigh scattered light from a reference material with 100% diffuse reflection, denoted as R_{ref}. The second scan measures the reflection (R_{sam}) and emission (E_{sam}) of the sample itself. The quantum yield can be calculated using the following equation:

$$\eta = \frac{E_{\text{sam}}}{R_{\text{ref}} - R_{\text{sam}}}. \tag{2.4}$$

The quantum yield can also be determined by comparing the wavelength-integrated intensity of the unknown sample to that of a reference (standard) sample. In this case, η is calculated using:

$$\eta = \eta_R \frac{I}{I_R} \frac{OD_R}{OD} \frac{n^2}{n_R^2}, \tag{2.5}$$

where I is the integrated intensity, OD is the optical density (absorbance), and n is the refractive index. The subscript R refers to the reference fluorophore of known quantum yield.

The lifetime is the average time the molecule spends in the excited state before returning to the ground state and is equal to:

$$\tau = \frac{1}{\Gamma_{\text{tot}}}. \tag{2.6}$$

The lifetime of the fluorophore in the absence of nonradiative processes is called the intrinsic lifetime ($\tau_{int} = 1/\Gamma_{rad}$) and it can be calculated from the absorption spectra, extinction coefficient (the ability of a molecule to absorb light), and emission spectra of the fluorophore using the Strickler–Berg equation:

$$\Gamma_{rad} = 2.88 \times 10^9 n^2 \frac{\int F(\bar{\nu}) \mathrm{d}\bar{\nu}}{\int F(\bar{\nu}) \mathrm{d}\bar{\nu}/\bar{\nu}^3} \int \frac{\epsilon(\bar{\nu})}{\bar{\nu}} \mathrm{d}\bar{\nu} \tag{2.7}$$

where, $F(\bar{\nu})$ is the emission spectrum plotted on the wavenumber (cm^{-1}) scale, $\epsilon(\bar{\nu})$ is the absorption spectrum, and n is the refractive index of the medium.

One of the organic molecules used in this work is ATTO-647N (Attotech: Eq.ATTO-647N) due to its stability. The spectrum and structure of the ATTO-647N molecule are shown in Fig. 2.3. By calculating Eq. 2.7 for the spectrum of ATTO-647N and substituting it into Eq. 2.3 with $\eta = 0.65$ [29] one can find the lifetime (τ) for different media. Figure 2.4 shows the variation of τ as a function of media refractive index for ATTO-647N and beads 660/680, used in this study. Having knowledge of the theoretical lifetime changes of these emitters provides insight into the expected changes during experiments, but the experimental values may deviate from theory due to interactions of the molecule with the medium (solvent) and refractive index variations between absorption and emission wavelength.

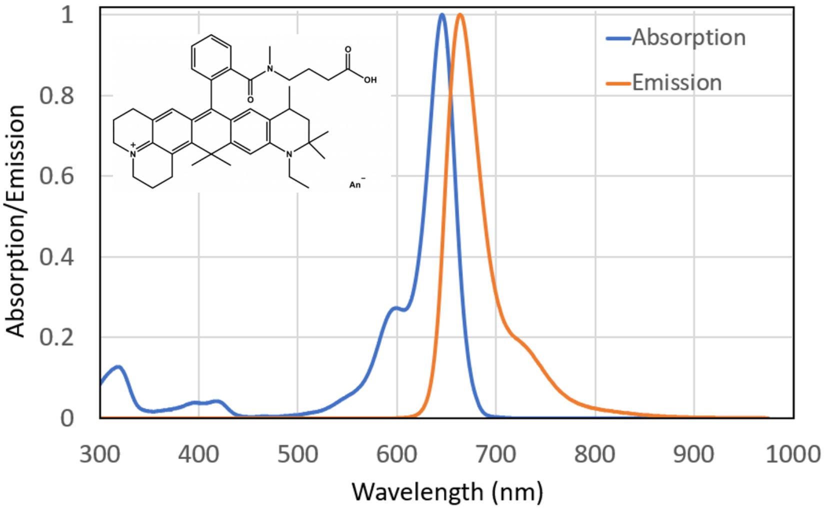

Figure 2.3: ***Absorption and emission spectrum of ATTO-647N****. Inset, the molecular structure of ATTO-647N.*

To measure the lifetimes of molecules one can use the time-domain method. In this method, the sample is excited using a pulsed laser in the excitation wavelength range. The width of the pulse must be shorter than the decay time of the molecules. If the molecules are excited by an infinitely sharp pulse, an initial population of f_0 in the excited state can result. The excited state decays at the rate $\Gamma_{\mathrm{rad}} + \Gamma_{\mathrm{nrad}}$

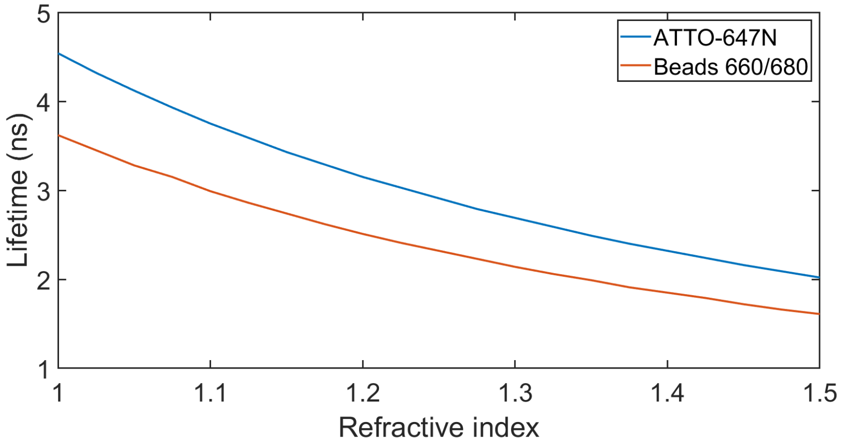

Figure 2.4: ***Lifetime of ATTO-647N and Beads 660/680 in media with different refractive indices.*** *The intrinsic lifetime is calculated using the Strickler–Berg equation with* $\eta_{\text{ATTO}} = 0.65$ *and* $\eta_{\text{Beads}} = 0.7$.

according to

$$\frac{\mathrm{d}f(t)}{\mathrm{d}t} = (\Gamma_{\text{nrad}} + \Gamma_{\text{rad}})f(t) \tag{2.8}$$

where $f(t)$ is the number of excited molecules at time t. Solving equation 2.8 shows that the excited state population undergoes exponential decay,

$$f(t) = f_0 \exp\left(\frac{-t}{(\Gamma_{\text{rad}} + \Gamma_{\text{nrad}})}\right). \tag{2.9}$$

In the experiment, fluorescence intensity corresponds to the number of excited molecules. Hence, by replacing $f(t)$ with $I(t)$ gives:

$$I(t) = I_0 \exp(-t/\tau) \tag{2.10}$$

where lifetime $\tau = 1/(\Gamma_{\text{rad}} + \Gamma_{\text{nrad}})$ and I_0 is the intensity at $t = 0$. By fitting this equation to the experimental data one can find the lifetime τ. This equation is only valid when we have one type of molecular excitation in the sample.

However, most samples contain more than one molecule or temporally correlated background which can change the signal. If the sample contains different types of molecules with different lifetimes, a close estimation of each lifetime can be found using the expansion of Eq. 2.10:

$$I(t) = \sum_i \alpha_i \exp^{-t/\tau_i}, \tag{2.11}$$

where i represents the possible decay channels. On normalizing the data, the values of α_i represent the proportion of each fluorophore. The signal processing requires deconvolution before the lifetime fitting, which is explained in detail in Sec. 4.2.

2.3 Fluorescence quenching and bleaching

Quenching is a phenomenon, which can decrease fluorescence. It can happen via different mechanisms, such as excited state reactions, energy transfer, ground-state complex formation, and quenching due to collisions with other molecules. The latter occurs when the excited-state fluorophore is deactivated upon contact with the quencher molecule in the solution. However quenching causes a reduction in fluorescence, can reveal information about the dynamics of the sample in solution. For example, if a fluorophore in the excited state collides with a quenching molecule, then the fluorophore returns to the ground state without the emission of a photon. Depending on the diffusion coefficient of the quenching molecule (D) and the lifetime of the fluorophores, the average distance of the quencher, which is several nanometers [25], is given by Einstein's equation:

$$\Delta x = \sqrt{2D\tau}. \tag{2.12}$$

When a molecule is situated close to a metal surface, its fluorescence is quenched due to energy transfer to the metal. This quenching effect is attributed to lossy surface waves (LSWs), dissipation losses, ohmic losses, and similar terms, all of which imply a nonradiative dissipation of energy within the metal. To calculate the probability of nonradiative surface energy transfer (SET) of the fluorescent molecule we use Chance–Prock–Silbey–Kuhn theory in terms of the distance between a metal thin film and a dipole. The distance at which the fluorescence drops to 50% (i.e., equal probabilities of energy transfer and spontaneous emission) is [30]:

$$d_0 = \frac{\alpha\lambda}{n_\mathrm{m}}(A\eta)^{(1/4)}\left[\frac{n_\mathrm{r}}{2n_\mathrm{m}}\left(1+\frac{\epsilon_1^2}{|\epsilon_2|^2}\right)\right]^{(1/4)}, \tag{2.13}$$

where λ is the emission wavelength maximum of the donor, and η is its quantum yield. n_m and ϵ_1 are the solvent's refractive index and dielectric function (medium between particle and metal film), respectively. n_r is the refractive index of the metal, and ϵ_2 is the complex dielectric function of the metal, which can be decomposed into real and imaginary components. The orientation of the donor to the metal plasmon vector is α, and it is assumed to be influenced by the averaged vector resulting in $\alpha = (9/2)^{1/4}/4\pi$. A is the absorptivity of a thin film mirror:

$$A = \frac{4\pi k_2 x}{\lambda}. \tag{2.14}$$

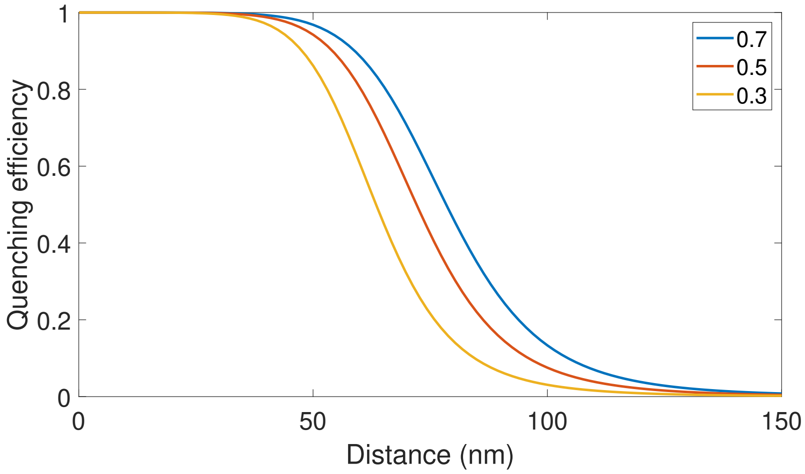

Figure 2.5: ***Theoretical quenching efficiency of a dipole near a thin gold surface.*** *The quenching efficiency of an emitter with* $\lambda = 680$ *nm in the vicinity of a 10 nm gold surface is plotted. Each line corresponds to a different quantum yield of the emitter (*$\eta = 0.7$*,* 0.5*, and* 0.3*). The dipole is randomly oriented.*

Here, k_2 is the extinction component of the metal refractive index, and x is the thickness of the metal film.

The quenching efficiency of a randomly oriented dipole versus the distance (d) between the dipole and metal is determined by Eq. 2.15.

$$Q_{\text{eff}} = \frac{1}{1 + \left(\frac{d}{d_0}\right)^4}. \tag{2.15}$$

Figure 2.5 shows the quenching efficiency of a fluorescent molecule emitted at 680 nm with different quantum yields in the vicinity of a gold plane of 10 nm thickness. These values are chosen close to the actual values in the experiments in this project. Here, we assume that the medium between the dipole and metal is air, and the emission of the dipole is averaged for random orientations. The quenching efficiency drops to almost zero beyond a 150 nm distance from the gold surface. A thin dielectric layer as a spacer can reduce quenching. For example, a 50 nm layer of SiO_2 ($n_m = 1.45$) causes the quenching efficiency to drop to almost zero. Moreover, for thicker gold layers, the effective length of quenching increases (not shown), and a larger spacer is required to avoid intrinsic quenching.

Unlike quenching, which is mainly a reversible process, photobleaching is a dynamic and irreversible process in which fluorescent molecules undergo photoinduced chemical destruction upon absorption of light, thus losing their ability to fluoresce. The amount of bleaching depends on the molecular structure, the local environment around the fluorescent molecule, exposure time, and the energy of the light. Therefore, some fluorophores can bleach quickly, while others have several thousands of excitation and emission cycles before bleaching.

Moreover, in fluids, fluorescence recovery after photobleaching (FRAP) is the term used to describe the diffusion of fluorescent molecules from the surrounding area into a photobleached region, which occurs when the fluorescence intensity of a specific area in a fluorescent sample diminishes due to excessive excitation. This phenomenon is characterized by a time-dependent recovery of fluorescence intensity in the photobleached region. FRAP is a well-known method for determining the kinetics of diffusion as well as interactions of biological molecules in living specimens [31] when the molecules are not immobilized.

In fluorescence intensity measurements, the duration of the experiment should be shorter than the bleaching time of the molecule in order to ensure the bleaching effect does not change the results. A simple method used to measure the bleaching time of a molecule is to expose the molecules to the same excitation power and experimental conditions for a longer time. By fitting the intensity data for a different time, one can calculate the period over which the fluorescence intensity of the molecules drops to 50%. This time is known as the bleaching time.

For fluorescent samples at low concentrations, the bleaching effect can be used to estimate the number of molecules in the sample if the molecules are immobilized, as repeated excitation can cause them to bleach. A more thorough clarification of this matter is presented in Sec. 4.4.

2.4 Intensity and radiation pattern of an emitter

In the context of electrodynamics, a single fluorescent molecule can be modeled as a dipole because molecules exhibit dipole moments caused by non-uniform distributions of positive and negative charges among their atoms. When the molecule's momentum is disturbed by oscillating electrons, it emits light at a frequency similar to the oscillation frequency of the dipole. Therefore, in theory, we can replace an emitter with an oscillating dipole.

Before focusing on the emission of a dipole in the vicinity of an optical antenna, we consider its emission in a homogeneous environment. Two oscillating electric charges q with opposite signs separated by an infinitesimal vector $\mathrm{d}\mathbf{s}$ result in a dipole moment. Using volume integral equations and the fact that the current density of a point source with its origin at the center of the charge distribution is

$\mathbf{j}(\mathbf{r}) = -i\omega\mu\delta(\mathbf{r}-\mathbf{r_0})$, we can derive the electric and magnetic fields.

$$\mathbf{E}(\mathbf{r}) = \omega^2\mu\mu_0^2 \overset{\leftrightarrow}{\mathbf{G}}(\mathbf{r},\mathbf{r_0})\,\boldsymbol{\mu}, \tag{2.16}$$

$$\mathbf{H}(\mathbf{r}) = -i\omega\left[\boldsymbol{\nabla}\times\overset{\leftrightarrow}{\mathbf{G}}(\mathbf{r},\mathbf{r_0})\right]\boldsymbol{\mu}. \tag{2.17}$$

Here, ω is the angular frequency, and μ_0 and μ are permeability in vacuum and medium, respectively. $\overset{\leftrightarrow}{\mathbf{G}}$ $(\mathbf{r},\mathbf{r_0})$ is the dyadic Green's function, which determines the fields of an arbitrarily oriented electric dipole located at $r = r_0$. This Green function for free space can be calculated using the scalar Green function $G(\mathbf{r}-\mathbf{r_0})$ giving:

$$\overset{\leftrightarrow}{\mathbf{G}}(R) = \left[(\overset{\leftrightarrow}{I}-\hat{R}\hat{R}) + \frac{i}{kR}(\overset{\leftrightarrow}{I}-3\hat{R}\hat{R}) - \frac{1}{k^2R^2}(\overset{\leftrightarrow}{I}-3\hat{R}\hat{R})\right]G_0(R), \tag{2.18}$$

where $R = |\mathbf{r}-\mathbf{r_0}|$ and $\hat{R} = (\mathbf{r}-\mathbf{r_0})/|\mathbf{r}-\mathbf{r_0}|$. The Green's function has terms with $(kR)^{-1}$, $(kR)^{-2}$ and $(kR)^{-3}$. In the farfield, for which $R \gg \lambda$, only the terms with $(kR)^{-1}$ remain. In contrast, the dominant terms in the near-field, for which $R \ll \lambda$ are the terms with $(kR)^{-3}$. The terms with $(kR)^{-2}$ dominate the intermediate-field at $R \approx \lambda$. On choosing the dipole in the z direction i.e., $\boldsymbol{\mu} = |\boldsymbol{\mu}|\mathbf{n}_z$ and selecting spherical coordinates $\mathbf{r} = (r,\theta,\phi)$ the field components $E(\phi)$, $H(r)$, and $H(\theta)$ become zero. The dipole radiates if it oscillates in time i.e. $\boldsymbol{\mu}(t) = \mathrm{Re}\{\boldsymbol{\mu}\exp(-i\omega t)\}$. This generates a monochromatic electromagnetic field, which can be calculated using the time-dependent Green's function. The field in a non-dispersive medium is equal to:

$$E_r(t) = \frac{\cos\theta}{4\pi\epsilon_0\epsilon}\left[\frac{2}{r^3} + \frac{2n}{cr^2}\frac{\mathrm{d}}{\mathrm{d}t}\right]|\boldsymbol{\mu}(t-nr/c)|, \tag{2.19}$$

$$E_\theta(t) = \frac{\sin\theta}{4\pi\epsilon_0\epsilon}\left[\frac{1}{r^3} + \frac{n}{cr^2}\frac{\mathrm{d}}{\mathrm{d}t} + \frac{n^2}{c^2r}\frac{\mathrm{d}^2}{\mathrm{d}t^2}+\right]|\boldsymbol{\mu}(t-nr/c)|, \tag{2.20}$$

$$H_\phi(t) = \frac{\sin\theta}{4\pi\epsilon_0\epsilon}\sqrt{\frac{\epsilon_0\epsilon}{\mu_0\mu}}\left[\frac{n}{cr^2}\frac{\mathrm{d}}{\mathrm{d}t} + \frac{n^2}{c^2r}\frac{\mathrm{d}^2}{\mathrm{d}t^2}+\right]|\boldsymbol{\mu}(t-nr/c)|, \tag{2.21}$$

where the term $(t-nr/c)$ is the retarded time and n is index of refraction.

To ascertain the radiation of a dipole in the far-field, we calculate the Poynting vector, where only the r^{-1} term is retained. Therefore, $E_r(t)$ (Eq. 2.19) vanishes and we have:

$$\mathbf{S}(t) = \mathbf{E}(t)\times\mathbf{H}(t) = \frac{\sin^2\theta}{16\pi^2\epsilon_0\epsilon}\frac{n^3}{r^2c^3}\left[\frac{\mathrm{d}^2}{\mathrm{d}t^2}|\boldsymbol{\mu}(t-nr/c)|\right]^2\mathbf{n_r}. \tag{2.22}$$

The radiated power P can be determined by integrating S(t) over a closed spherical surface as

$$\mathbf{P}(t) = \int\int \mathbf{S} \cdot r^2 \sin\theta \, \mathrm{d}\theta \, \mathrm{d}\phi = \frac{1}{4\pi\epsilon_0\epsilon} \frac{2n^3}{3c^3} \left[\frac{\mathrm{d}^2}{\mathrm{d}t^2} |\boldsymbol{\mu}(t - nr/c)| \right]^2 . \tag{2.23}$$

In the far field, the electric and magnetic fields of the wave are largely decoupled from the source, and the time-averaged Poynting vector can be calculated without taking the retarded time into account. This is because any changes in the fields due to the motion of charges in the source have had time to propagate out to the far field before the observer measures the fields.

$$\langle S \rangle = \frac{1}{2} \mathrm{Re}\{\mathbf{E} \times \mathbf{H}^*\} == \frac{|\boldsymbol{\mu}|^2 n^3 \omega^4}{12 c^3 \pi \epsilon_0 \epsilon}. \tag{2.24}$$

Moreover, the normalized radiated power in an infinitesimal unit angle of $\mathrm{d}\Omega = \sin\theta \, \mathrm{d}\theta \, \mathrm{d}\phi$ is equal to:

$$\frac{\bar{\mathbf{P}}}{\langle S \rangle} = \frac{3}{8\pi} \sin^2\theta, \tag{2.25}$$

and plotted in Fig. 2.6.

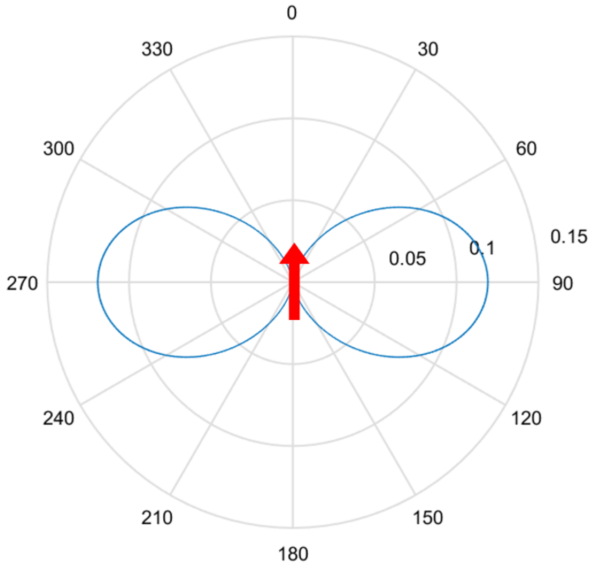

Figure 2.6: ***Emission of a dipole in polar coordinates based on Eq. 2.25.***

The radiation pattern of the dipole changes near an interface such as an air-glass interface. This change can be calculated using the transmission Green function (see Sec. 3.1). In this case, the dipole's radiation is a superposition of traveling and evanescent waves. The traveling waves can be detected in the far-field with a macroscopic device (allowed light). The evanescent waves, on the other hand, decay exponentially. However, they can also be transformed into traveling waves at the interface, and it is possible to detect them in the far-field [32]. These waves appear under an angle larger than the critical angle θ_c for total internal reflection, and they are known as forbidden light.

2.5 Types of emitters

In nanometer-sized structures, continuous scattering and absorption of light will be supplemented or replaced by resonant interactions if the photon energy reaches the energy difference of discrete internal (electronic) energy levels. For some "quantum confined" systems, these resonances are found at optical frequencies. In this section, we consider three main types of emitters: organic dye molecules, semiconductor quantum dots, and impurity centers in wide-bandgap semiconductors such as diamonds.

2.5.1 Fluorescent molecules

The lowest energy electronic transition for an organic molecule occors between the highest occupied molecular orbital (HOMO) and the lowest unoccupied molecular orbital (LUMO). In addition to the electronic energy levels, multi-atomic particles such as molecules have vibrational degrees of freedom. The total wavefunction of the system can be written as a product of a purely electronic and a purely vibrational wavefunction based on the Born–Oppenheimer approximation as the nucleus is much heavier than the electrons, and they can be treated separately. At ambient temperatures, the excitation of a molecule usually starts from the electronic ground state with no vibrational quanta excited.

To ensure coherence between the pump laser and the zero-phonon emission line from the fluorescent molecule, the molecule should be embedded in a crystalline matrix at cryogenic temperatures. This leads to extreme peak absorption cross-sections and to Rabi oscillations [33].

A molecule's three-dimensional orientation interacts with the field primarily through its electric transition dipole moment, and it can be approximated with a dipole, with the matrix element of the dipole operator between the HOMO and the LUMO wavefunctions supplemented by corresponding vibronic states. This matrix element is called the absorption dipole moment of the molecule.

Since the atoms have fixed positions within the molecular structure, the direction of the dipole moment vector is fixed with respect to the molecular structure. On changing the structure of the molecule, the absorption wavelength is shifted. Figure. 2.7 shows the absorption and emission of cyanine consisting of several interconnected aromatic rings.

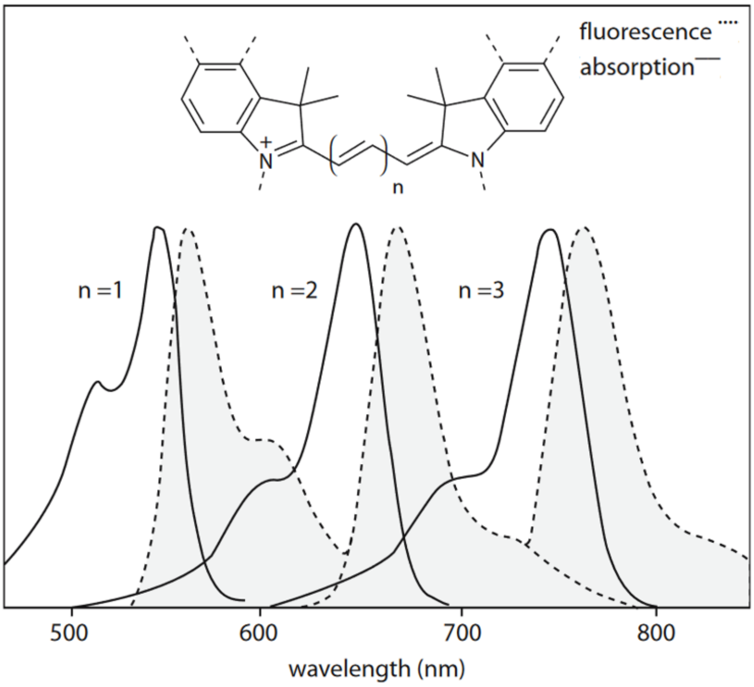

Figure 2.7: ***Typical absorption and fluorescence emission spectra of cyanine dyes.*** *The structure of the molecule determines its absorption and fluorescence emission spectrum. The insertion can cause redshifts by about 100 nm, e.g. with trimethine (n = 1), pentamethine (n = 2), and heptamethine (n = 3) chromophore resulting in the respective wavelength maxima [34].*

The emission dipole moment typically points in the same direction as the absorption dipole (long axis of the structure). However, there are exceptions if the molecule's geometry changes significantly between the electronic ground state and the excited state.

The emission spectrum consists of a sum of Lorentzians, the so-called vibrational progression, corresponding to the different decay pathways into the ground state vibronic levels. At room temperature, dephasing is strong, and leads to additional line broadening such that the vibrational progression is often difficult to observe. For a molecule, the probability of decaying into the vibrational ground state is determined by the overlap integrals of the related LUMO vibrational state wavefunction and the HOMO vibrational state wavefunctions. These overlap integrals, known as Frank–Condon factors, are described in Sec. 2.1.2.

In molecules, the presence of spin-orbit coupling results in a finite torque exerted on the electron's spin in the excited state, leading to a probability of spin reversal for the excited electron. This process is known as intersystem crossing. Normally, the intersystem rate is much lower than a chromophore's excited and decay rates. If a spin flip happens, the total electronic spin of the molecule changes from 0 to 1. Spin 1 has three possible orientations in an external magnetic field leading to a triplet of eigenstates called the triplet state. Once a molecule has undergone an intersystem crossing into the triplet state, it may decay into a singlet ground state. However, this is a spin-forbidden transition. Therefore, triplet states have extremely long lifetimes of the order of milliseconds. This trapping of the electron in the intersystem state for a long time causes no radiation in that period. When the electron relaxes to the ground state it can be excited again and re-emit photons during relaxation. This phenomenon is known as fluorescence blinking and is commonly observed when detecting single molecules.

In this work, we mainly use organic dye molecules with large molecular weights, and containing extended systems of conjugated double bonds. A small sphere made of an amorphous polymer such as polystyrene with diameter 40 nm is filled with dye molecules (TheormoFisher: FluoSpheres Carboxylate-Modified Microspheres 660/680) known as fluorescent beads or ATTO-647N dye labels with high quantum yield ($\eta = 0.65$) and exceptionally high stability towards atmospheric ozone and oxygen are used, depending on the purpose of the experiments.

2.5.2 Semiconductor quantum dots

In a semiconductor material, the bandgap can vary depending on its size. This variation occurs due to the overlap of atomic orbitals within the material. In the bulk state, where a large number of atoms participate in bonding, each atom shares some atomic orbitals, resulting in overlap and a relatively small bandgap. In nanoscale materials, such as quantum dots (QDs) however, the number of atoms and, as a result, the atomic orbitals involved in the overlap are significantly fewer than the bulk, increasing the bandgap (see Fig. 2.8). Once the size of a nanocrystal approaches the limit of the Bohr radius of an exciton, the states of the exciton shift to higher energy as confinement, which causes blue-shifted excitation and emission. This observation is attributed to the so-called quantum confinement effect.

In semiconductors, due to the small effective masses of the electrons and holes, the Bohr radius can be of the order of 10 nm, which means that quantum confinement in semiconductor nanocrystals becomes prominent at length scales much larger than the characteristic sizes of atoms or fluorescent molecules.

Quantum dots can be fabricated using various techniques such as colloidal synthesis, lithography, or epitaxial growth [36]. In the production of QDs, parameters such as crystallinity, shape control, and narrow distribution of size play an important role.

The quantum efficiencies for radiative decay of the confined excitons are relatively high because both the electron and the hole are confined to a nanometer-sized volume inside the dot [33]. This property makes quantum dots very useful in chemical

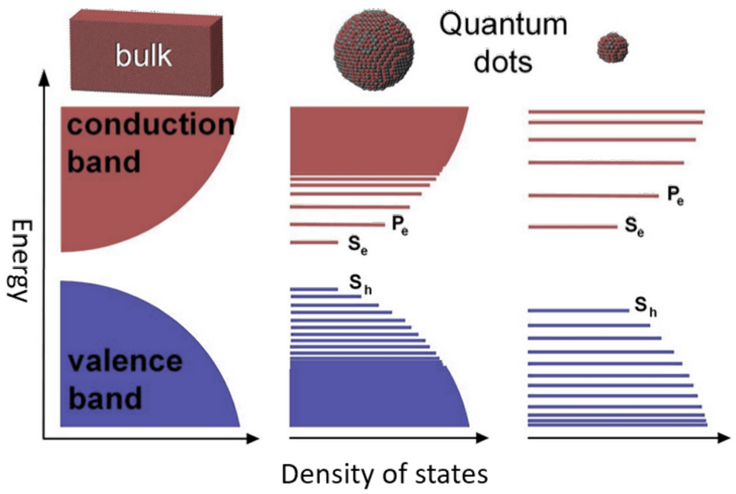

Figure 2.8: ***Energy bandgap in a semiconductor material.*** *Evolution of the electronic structure of inorganic semiconductors from bulk material to QDs of different sizes [35].*

sensing [37], biosensing [38], and opto-electric [39] applications.

2.5.3 Color centers in diamond

Another class of emitters is the defect centers in wide-bandgap semiconductors. Diamond with a very large bandgap (5.5 eV) and transparency from deep UV to IR wavelength is a well-known candidate for hosting luminescent defect centers. One of the notable defect centers in diamonds is the nitrogen-vacancy (NV), which consists of a single substitutional nitrogen and an empty site. Spin-optical properties of NV centers make them a promising candidate for quantum communication [40] and sensing [41] applications. One disadvantage, however, is the broad emission spectrum (∼100 nm) of NV centers of ambient temperatures. This is due to the strong electron-phonon coupling of local oscillation modes. Therefore, only 4% of the emitted light lies within the zero-phonon-line (ZPL).

Another prominent vacancy center in diamonds is the silicon-vacancy (SiV) center. In such a structure, two carbon atoms in the diamond crystal lattice are replaced by one silicon atom located between the two free lattice sites, as shown in Fig. 2.9. Silicon atoms present in the diamond are usually interstitials (located between lattice sites). On annealing, the foreign atoms can find vacancies and combine with the lattice. One of the essential characteristics of SiV centers is the narrow bandwidth of ZPL emission (0.5–5 nm for SiV^- at 737 nm). This is due to the weak electron-phonon interaction for the SiV center. The silicon atom is more than two times heavier than the nitrogen (and the carbon) atom, and the divacancy configuration is much more stable than the NV configuration. This leads to a much

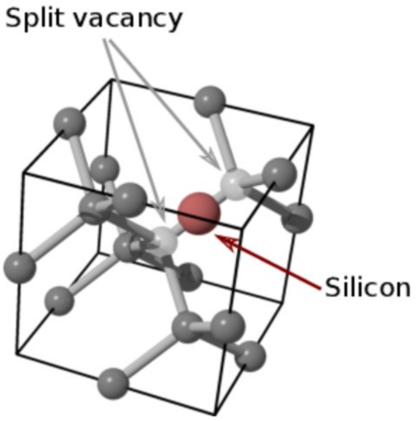

Figure 2.9: ***Diamond lattice containing a silicon-vacancy defect****. The silicon nucleus is located midway between two vacant nearest-neighbor lattice sites [42].*

weaker vibrational excitation during an optical transition in the SiV center. Due to the system's high stability, the configuration's location does not undergo significant changes. Therefore, the Franck–Condon principle supports direct ZPL transitions and suppresses transitions involving phonons, as the wavefunction overlap is maximized in this scenario [43].

SiV and NV centers in bulk diamonds do not show blinking or bleaching. This provides a very photostable system, which can be helpful in experiments with long exposure times. However, nanoparticle diamonds can show blinking due to the center's interaction with the environment [44, 45].

Chapter 3

Controlling emitters with optical antennas

An optical nanoantenna, like a radio frequency (RF) antenna, is a device that converts free propagating radiation into localized energy and vice versa. The geometry and material of an optical antenna can be modified to tailor this energy conversion. In general, optical antennas, made of metal nanostructures, can have a strong interaction with light that localizes the energy of electromagnetic waves and enhance the spontaneous emission of an emitter in its vicinity of the antenna. Moreover, similar to radio frequency antennas, the optical antenna can also direct light thanks to their structure and material. This will improve the signal-to-noise ratio of a fluorophore by directing the fluorescence toward a detector. These distinctive features of optical antennas make them suitable for use as micro- and nanodetectors, which require interdisciplinary efforts across fields such as electrical engineering, physical chemistry, materials science, optics, and photonics.

This chapter begins by discussing the general properties of optical antennas and introduces the Yagi–Uda planar antenna in Sec. 3.1. We then focus on a specific type of optical antenna, the optical planar antenna, which can be made of dielectric or metal films, in Sec. 3.2. We examine the beaming effect of these antennas for a dipole that is embedded between the antenna's planes.

3.1 Optical antennas

An optical antenna is a structure that enhances the local light-matter interaction. Optical antennas share several concepts of radio-wave antennas, but mainly they have smaller structures (from a few nanometers to a few micrometers) with distinctive geometries (see Fig. 3.1). The coupling between the antenna and matter is via displacement currents proportional to the near field vector **E**, which makes a confined mode. This mode is strongly position and polarization-dependent [27]. The mode can be controlled not only by the geometrical shape of the antenna but also by intrinsic material properties of the antenna, such as the optical constants and the electron mean free path.

Generally, the emitter's signal can be amplified using an antenna with high efficiency. Such an antenna can enhance the strength of the electromagnetic field and modify the decay rate and the antenna's directivity. These parameters will be explained as follows.

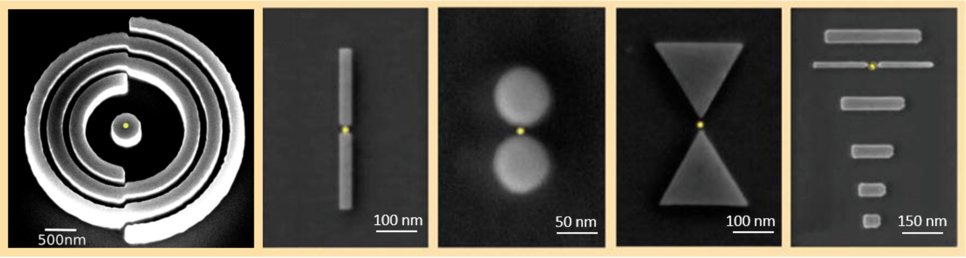

Spiral Two-wire nanodimer Bow tie Yagi-Uda

Figure 3.1: ***Different geometrical structure of optical antenna*** *The geometry and size of the antenna determine its interactions with a material in a specific wavelength. They can modify light directionality and excitation and emission rates. The image is adapted from [46]; the scales are an approximation.*

3.1.1 Antenna efficiency

In general, the aim of an antenna is to enhance the transmission efficiency from a transmitter (e.g., a dipole) to a receiver. This enhancement can be achieved by increasing the total amount of radiation released by the transmitter. This means that by coupling an emitter to an antenna, the total power (P_{tot}) dissipated by the antenna can be increased [33]. This power is the sum of the radiated power (P_{rad}) and the lost power (P_{nr}) due to heating, energy transfer to the environment or quenching by other molecules. The antenna efficiency then is defined as

$$\eta_a = \frac{P_{\text{rad}}}{P_{\text{tot}}} = \frac{P_{\text{rad}}}{P_{\text{rad}} + P_{\text{nr}}}. \tag{3.1}$$

The value of P_{tot} can be determined by the electric field at the dipole's position using the rate of energy dissipation $\mathrm{d}W/\mathrm{d}t$ (Poynting's theorem)

$$\frac{\mathrm{d}W}{\mathrm{d}t} = \frac{\omega}{2}\,\mathrm{Im}\left\{\boldsymbol{\mu}^* \cdot \mathbf{E}(\mathbf{r_0})\right\}, \tag{3.2}$$

where $\mathbf{E}(\mathbf{r_0})$ is the field at the dipole origin $\mathbf{r_0}$. This equation can be rewritten in terms of the Green function using Eq. 2.16. On the other hand, the amount of P_{rad} is evaluated by the calculation of the energy flux through a surface enclosing both the dipole and the antenna (see Eq. 2.23). These parameters can be calculated using the finite-difference time-domain (FDTD) method using a closed detector surface around the dipole and the antenna to calculate P_{rad} and a small detector that takes only the FDTD cell of the dipole in order to compute P [47].

3.1.2 Field enhancement

Field enhancement is a method to place the molecule near a nanostructure that enhances the field locally. There are two main electromagnetic enhancement mechanisms in antennas, both based on surface plasmon polariton (SPP) mode propagation in a metal (dielectric antennas modify the field very weakly). One is SPP resonance (e.g., gold nanosphere resonance), and the other is the lightning rod effect, which occurs in antennas with a sharp tip. The latter is described by slowing down polaritonic waves while proceeding on the surface of a metallic cone toward the tip, which gradually increases the field intensity [48]. Since the near field is directly proportional to the scattering cross-section σ [49], nanoparticles with sharp edges tend to exhibit larger enhancements than nanospheres. The strength of the near field can be magnified more if the particle traps in a nanoscale gap between two (or more) sharp nanostructures [50].

Field enhancement of a metal nanoparticle

As an example of field enhancement with the SPP resonance, we consider a metallic nanosphere facing the electric field $\mathbf{E_0}$ in a medium. Applying boundary conditions between the medium and the metal and the fact that the electric field is unperturbed at large distances from the sphere, i.e., $\lim\limits_{r\to\infty} \Phi_{\text{out}} = -E_0 r\cos\theta = -E_0 z$, the electric field outside of the metal ($\mathbf{E}_{\text{out}}$) is calculable. Here, Φ_{out} is the scalar potential outside the metal nanosphere, and θ is the angle between the incident field and the observation point. Due to the inherent symmetry of the problem, the fields remain unaffected by changes in the azimuthal angle ϕ. As a result, the field enhancement is the intensity ratio between $\mathbf{E}_{\text{out}}$ and $\mathbf{E_0}$ is [51]

$$K = \frac{|\mathbf{E}_{\text{out}}|^2}{|\mathbf{E_0}|^{\mathbf{2}}} = \left|1 + \frac{\alpha}{2\pi r^3}\right|^2, \tag{3.3}$$

where α is the polarizability of the sphere

$$\alpha = 4\pi a^3 \frac{\epsilon - \epsilon_m}{\epsilon + 2\epsilon_m}. \tag{3.4}$$

Here a is the radius of the sphere, and ϵ and ϵ_m represent the permittivity of the metal and the medium, respectively. For resonance condition, $\epsilon = -2\epsilon_m$, the polarizability exhibits a singularity corresponding to the surface plasmon polariton (SPP) mode. This clearly determines that the field enhancement and, as a result, the emission decay rate (subsection 3.1.3) is strongly related to the dipole polarization [27]. Interpretation of the intermediate cases is more complex and requires a numerical analysis.

Field enhancement of a metallic cone-shaped antenna

For a metallic cone-shaped antenna, the near field caused by the electric dipole induced in the antenna $\mathbf{E}_{\text{dip}}$ is related to the antenna susceptibility χ and the geometrical factor L. The latter is also related to the lighting rod effect

$$\mathbf{E}_{\text{dip}} \simeq (1-L)\chi E_0. \tag{3.5}$$

Therefore, the field enhancement can be written as:

$$\frac{|\mathbf{E}_{\text{dip}}|^2}{|\mathbf{E_0}|^2} = \eta_a \frac{P_{\text{tot}}}{P^o_{\text{rad}}}, \tag{3.6}$$

where P^o_{rad} is the radiated power without antenna.

3.1.3 Modification of the decay rates and quantum yield

The substantial modification of the radiative decay rate is associated with a strong field enhancement, which means a strong local electromagnetic environment. The modification of the radiative decay rate can be obtained by measuring the power emitted by a classical dipole placed in proximity to the optical antenna. Moreover, the classical radiation energy becomes proportional to the spontaneous emission rate [52], which means

$$\frac{\Gamma_{\text{rad}}}{\Gamma^o_{\text{rad}}} = \frac{P_{\text{rad}}}{P^o_{\text{rad}}} = \frac{12c}{\omega_0}\,\text{Im}\left\{\mathbf{n}_\mu \cdot \overset{\leftrightarrow}{\mathbf{G}}(\mathbf{r_0},\mathbf{r_0};\omega_\mathbf{0}) \cdot \mathbf{n}_\mu\right\}, \tag{3.7}$$

where Γ^o_{rad} is the fluorescence decay rate of the dipole in free space and $\mathbf{n}_\mu$ is the unit vector in the dipole direction. P_{rad} is the power radiated to the far field when the antenna is present. In addition, the total decay rate Γ is expressed by

$$\frac{\Gamma}{\Gamma^o_{\text{rad}}} = \frac{P}{P^o_{\text{rad}}}, \tag{3.8}$$

where P is the total power dissipated by the dipole. Γ can be written as the summation of radiative and non-radiative decay rates.

$$\Gamma = \Gamma_{\text{rad}} + \Gamma_{\text{nr}} + \Gamma^{o}_{\text{nr}}, \tag{3.9}$$

where Γ_{rad} and Γ_{nr} are the radiative and non-radiative rate in the presence of the optical antenna, respectively, and Γ^{o}_{nr} is the intrinsic non-radiative decay rate.

Enhancing the radiative decay rate is expected to improve the quantum yield of a light emitter. Based on the equivalence between the modification of transition rates in classical and quantum electrodynamics, we define an antenna efficiency based on the radiation decay of the molecule in the antenna. This leads to $\eta_a = \Gamma_{\text{rad}}/\Gamma_{\text{tot}}$ and $\eta_o = \Gamma^{o}_{\text{rad}}/(\Gamma^{o}_{\text{rad}} + \Gamma^{o}_{\text{nr}})$.

The interaction of the molecule with its local environment introduces an additional non-radiative rate Γ_{nr}, thereby modifying the quantum yield to:

$$\eta = \frac{\Gamma_{\text{rad}}}{\Gamma_{\text{rad}} + \Gamma^{o}_{\text{nr}} + \Gamma_{\text{nr}}} = \frac{\Gamma_{\text{rad}}/\Gamma^{o}_{\text{rad}}}{\Gamma_{\text{rad}}/\Gamma^{o}_{\text{rad}} + \Gamma_{\text{nr}}/\Gamma^{o}_{\text{rad}} + (1-\eta_o)/\eta_o}. \tag{3.10}$$

Here, we assume that the emitter is at a distance where the nanoantenna does not affect its electron structure and, therefore, the intrinsic non-radiative decay rate Γ^{o}_{nr} is not disturbed by boundary conditions. If $\eta_o = 1$, the quantum yield η is only determined by the antenna efficiency. We can also rewrite Eq. 3.10 in the form of:

$$\eta = \frac{\eta_o}{(1-\eta_o)\Gamma^{o}_{\text{rad}}/\Gamma_{\text{rad}} + \eta_o/\eta_a}, \tag{3.11}$$

which has been used in Sec. 4.2 for the calculation of the quantum yield of a dipole parallel to a planar Yagi–Uda antenna.

3.1.4 Modification of the radiation pattern

The signal enhancement using an antenna can be achieved by altering the radiation pattern of the emitter such that more power is directed toward the detector. The antenna's ability to concentrate the radiated power in a certain direction is known as directionality. It can be calculated as:

$$D(\theta, \phi) = \frac{4\pi}{P_{\text{rad}}} p(\theta, \phi), \tag{3.12}$$

where $p(\theta, \phi)$ is the angular power density. Since the directivity is calculated in the far-field the field is transverse and it can be written as two polarization directions

$\mathbf{n}_\theta$ and $\mathbf{n}_\phi$. Consequently

$$D_\theta(\theta,\phi) = \frac{4\pi}{P_{\mathrm{rad}}} p_\theta(\theta,\phi) \qquad \textit{and} \qquad D_\phi(\theta,\phi) = \frac{4\pi}{P_{\mathrm{rad}}} p_\phi(\theta,\phi). \tag{3.13}$$

Here, $p_\theta(\theta,\phi)$ and $p_\phi(\theta,\phi)$ are the normalized angular powers measured in $\mathbf{n}_\theta$ and $\mathbf{n}_\phi$ direction, respectively. Since $\mathbf{n}_\theta \cdot \mathbf{n}_\phi = 0$ we have

$$D(\theta,\phi) = D_\theta(\theta,\phi) + D_\phi(\theta,\phi) \tag{3.14}$$

It is important to mention that if the molecule is strongly coupled to the optical antenna, its energy is efficiently transferred to the SPP modes, and as a result, the emission pattern is completely determined by the antenna. On the other hand, if the nanoantenna is polarized by a nearby molecule, the radiation strongly depends on the orientation of the molecular dipole moment.

Back focal plane imaging

The back focal plane (BFP) of an optical system is the plane transverse to the rear focal point of the system. The far-field at the BFP of a lens is directly related to the Fourier transform of the object before the lens known as angular spectrum representation. Using Weyl identity, derived from the angular spectrum representation,

$$\frac{e^{ikr}}{r} = \frac{i}{2\pi} \iint\limits_{-\infty}^{+\infty} \frac{\mathrm{e}^{ik_x x + ik_y y + ik_z |z|}}{k_z} \,\mathrm{d}k_x\,\mathrm{d}k_y \quad \text{for} \quad r = \sqrt{x^2+y^2+z^2} \tag{3.15}$$

one can compute the dyadic Green's functions of a dipole in the form of an angular spectrum. The Green's functions can be separated into reflection ($\overleftrightarrow{\mathbf{G}}_{\mathrm{refl}}$), transmission ($\overleftrightarrow{\mathbf{G}}_{\mathrm{tr}}$) and intrinsic ($\overleftrightarrow{\mathbf{G}}_0$) terms for a dipole in the vicinity of a planar interface. The asymptotic far-field forms of the Green's functions are driven by

$$\overleftrightarrow{\mathbf{G}}_{\mathrm{tr}\infty}\left(\frac{x}{r},\frac{y}{r}\right) = -ik\frac{z}{r}\hat{\overleftrightarrow{\mathbf{G}}}_{\mathrm{tr}}\left(k\frac{x}{r},k\frac{y}{r};0\right)\frac{e^{ikr}}{r}. \tag{3.16}$$

Afterward, finding the $\mathbf{E}$ field is straightforward by using Eq. 2.16. If there is a lens below the surface (as shown in Fig. 3.2), the radiation pattern $p(\Omega)$ on the BFP image surface can be calculated by writing Eq. 2.24 in the form of [53]

$$\langle S\rangle = \frac{1}{2}\sqrt{\frac{\epsilon_0\epsilon_m}{\mu\mu_m}}\mathbf{E}\cdot\mathbf{E}^*\mathbf{n}_{\mathbf{r}}, \tag{3.17}$$

where

$$p(\Omega)\mathrm{d}\Omega = r^2\langle S\rangle \cdot \mathbf{n_r}, \tag{3.18}$$

and using the fact that in the far-field the magnetic field is transverse to the electric field. Writing ($\overset{\leftrightarrow}{\mathbf{G}}_{\mathrm{tr}}$) in spherical coordinate, Θ and Φ show the direction of dipole moment in spherical coordinates, and θ and ϕ are the emission angles. The index m determines the material in the lower half-space. It is important to note $f/r = \sin\theta$ with f indicating the focal length of the BFP lens. Therefore, the intensity pattern on the BFP surface illustrates the molecule's orientation and the corresponding emission direction for a high NA objective.

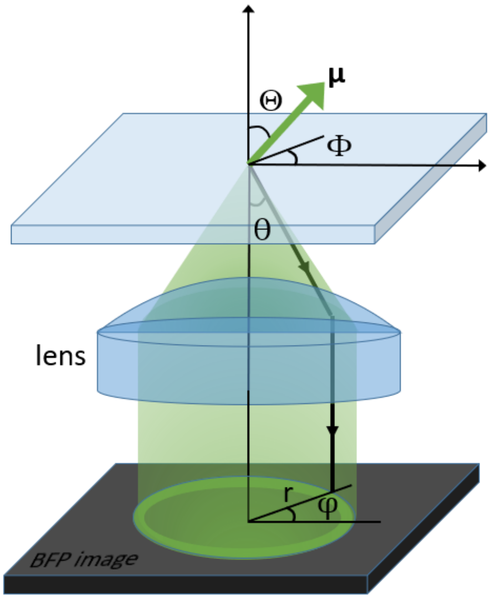

Figure 3.2: ***Coordinate system used for calculation of BFP.*** *The green arrow is a dipole with dipole moment* $\boldsymbol{\mu}$*. A lens with focal length* f *is used to provide the BFP image.*

In the experiment, the light of randomly oriented molecules on a substrate is mainly emitted with an angle above the critical angle (supercritical angle) between the two media [54]. Therefore, by measuring the BFP image of an ensemble of molecules one can calibrate the emission angle. The BFP image in this case is a ring, and its radius is proportional to the emission angle (see Fig. 3.2). This radius is directly related to the number of pixels of the camera. Thereby, one can plot the intensity of emission versus the emission angle θ based on the intensity at each pixel. This method has been applied in Sec. 4.2 to calculate the directionality of a fluorescence bead.

3.1.5 The Yagi–Uda antenna

To understand this work the fundamental knowledge of ”optical Yagi–Uda antenna” is required. The Yagi–Uda antenna is an array made of several dipole antenna elements with specific distances to form a directional emission pattern [55]. It consists of three main elements: active dipole (feed), reflector, and director. Due to their simple structure and design, Yagi–Uda antennas are commonly used for transmitting and receiving radio frequencies (RF) in various applications such as TV antennas and radar systems.

The far-field Poynting vector $\mathbf{S}(\mathbf{r})$ of an array of induced dipoles $\boldsymbol{\mu}_i$ can be calculated using free-space Green's function (Eq. 2.18) [27]. The $\boldsymbol{\mu}_i$ is proportional to the dipole polarizabilities α_i and the dipole locations $\mathbf{d}_i$. Therefore, for a fixed wavelength the radiation pattern can be tuned by these two parameters. Moreover, the impedance of the antenna Z is related to the length of the feed element l and consequently to the radiation pattern.

One of the main differences between a Yagi–Uda antenna in RF and visible (VIS) range is the effective wavelength of incident radiation λ_{eff} because the resonant wavelength of a nanoparticle is determined not only by its length but also by its shape and composition [56]. This difference directly influences the design of the antenna. As shown in Fig. 3.3, in the RF Yagi–Uda antenna, the distance between the feed and the reflector is $\lambda/4$ and the feed-director distance is λ/π [56]. However, in optical frequencies, because of the significant effect of the penetration of radiation into metals, the effective wavelength is [21]:

$$\lambda_{\text{eff}} = L_1 + L_2 \left(\frac{\lambda}{\lambda_p} \right), \tag{3.19}$$

where L_1 and L_2 are geometric constants and λ_p is the plasma wavelength, which is equal to:

$$\lambda_p = 2\pi \sqrt{\frac{\epsilon_0 m}{N q^2}}. \tag{3.20}$$

Here, m is the mass of the electron, N is the number of electrons per unit volume, and q is the charge of an electron. The λ_{eff} is related to the localized surface plasmon resonance, which is explained by the polarizability (α) of the nanoantenna. For a five-element optical Yagi–Uda antenna, similar to Fig. 3.3, the distance between the dipole (feed) and reflector or director is between $0.2\lambda/n$ and $0.3\lambda/n$ [57], where n is the refractive index of the medium.

The directional emission of the Yagi–Uda antenna results from the constructive and destructive interference of the radiated electromagnetic waves from the indi-

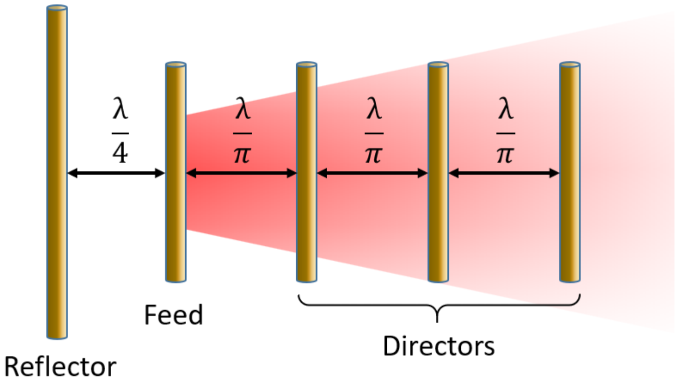

Figure 3.3: ***Typical geometry of a Yagi–Uda antenna*** *The distance between each element at RF waves is illustrated. In the VIS range, the distances are shorter.*

vidual dipole elements that make up the antenna. As the waves from each dipole combine, they create a radiation pattern that is strongest in one direction and weaker in others, resulting in the antenna's directional characteristics. This will be explained in subsection 3.2.2 for the planar Yagi–Uda antenna.

3.2 Optical planar antennas

While conventional optical Yagi–Uda antennas can direct electromagnetic waves at a small angle, their nanoscale size makes it difficult to control their characteristics. On the other hand, the planar antenna configurations are engineered to enhance the collection efficiency by modification of the radiation pattern. This type of antenna normally contains a stack of dielectric and/or metal layers with defined distances in order to achieve high collection efficiencies up to unity [58]. Since the layers have infinite sizes in lateral directions and can stack on top of each other, the fabrication of such an antenna is much simpler than the small nanostructured antennas.

This structure appears to share similarities with an optical cavity, however, its resonance length falls short of the minimum requirement of half the wavelength (i.e., $\lambda/2$) needed to produce a strong cavity effect. Moreover, the planar Yagi–Uda antenna has a broad-band resonance, and consequently, it is not sensitive to the position of the dipole inside the active medium (medium, which contains the dipole). They also have a small impact on spontaneous emission (the effect on the decay rate is small) and the characteristic of the emitter is conserved in such a system.

One way to determine the radiation pattern is to calculate the field $\mathbf{E}$ using the Green function $\overleftrightarrow{\mathbf{G}}(\mathbf{r}-\mathbf{r_0})$. Since we only consider the emission out of the antenna the field is only related to transmission Green function [33]

$$\mathbf{E} = \omega^2 \mu_0 \mu \overset{\leftrightarrow}{\mathbf{G}}_{\mathrm{tr}}(\mathbf{r} - \mathbf{r_0})\boldsymbol{\mu}. \tag{3.21}$$

Equation 3.16 is applicable for the calculation of the radiation pattern at far-field ($r \gg \lambda$) and one can use the transmitted far-field Green's function $\overset{\leftrightarrow}{\mathbf{G}}_{\mathrm{tr}\infty}(\mathbf{r} - \mathbf{r_0})$. Here, $\mathbf{r_0}$ is the position of the dipole.

First, we consider the general case when a randomly oriented dipole is embedded in a stratified structure. This means on both sides of the emitter, there are two series of layers numbered from $1, 2, \ldots, i, \ldots, M$ above and $-1, -2, \ldots, -i, \ldots, N$ below the dipole as shown in Fig. 3.4. The dipole is at z_0, and it has an angle α with the optical axis z. The refractive index and thickness of each medium are determined by n_i and d_i, respectively, and the active medium has a subscript m, i.e., n_m and d_m.

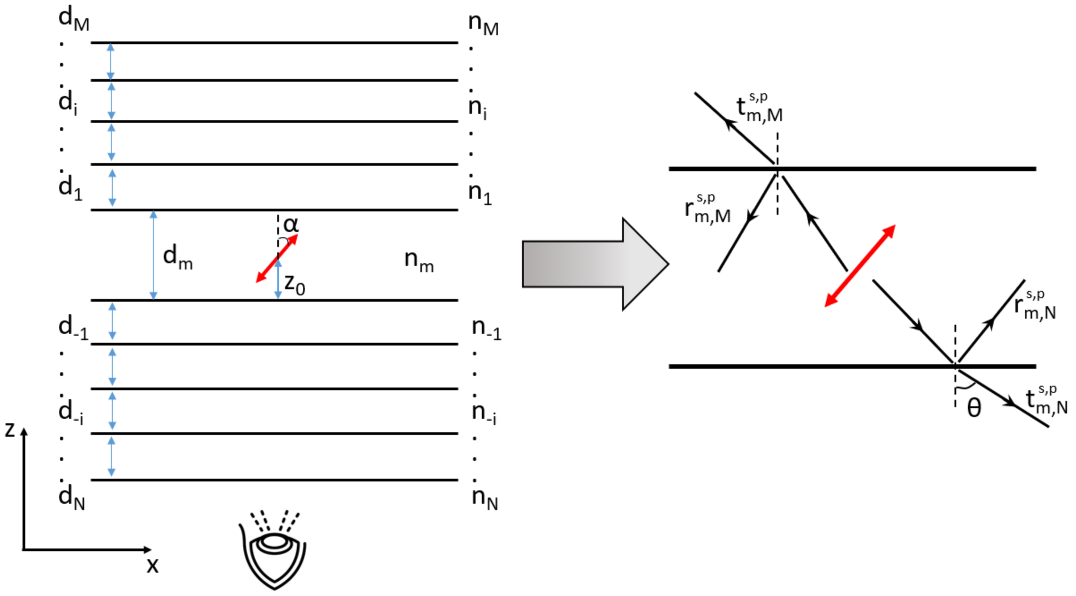

Figure 3.4: ***A randomly oriented dipole sandwiched between*** $N + M$ ***layers.*** *The* $n_{(-)i}$ *and* $d_{(-)i}$ *are the refractive index and the thickness of each layer, respectively where i represents the i-th layer. The transmission t and reflection r coefficients of dipole emission are shown in the right side scheme. Here,* z_0 *is the distance from the dipole to the substrate and the eye symbol shows the detection side.*

The aim is to find the r and t coefficients in the last layer N and replace them into $\overset{\leftrightarrow}{\mathbf{G}}_{\mathrm{tr}\infty}(\mathbf{r} - \mathbf{r_0})$ in order to derive the Green function. For simplicity the dipole field is described by its s- and p-polarized plane and evanescent waves. The $\mathbf{k}$ at each layer is a complex wave vector, the real part describes the direction of the phase velocity, and the imaginary part the absorption of wave propagation in that direction. The amplitude of $\mathbf{k}$ in z direction for each layer is equal to:

$$k_{z,i} = \sqrt{k_i^2 - k_{x,i}^2 - k_{y,i}^2}, \tag{3.22}$$

where $\sqrt{k_{x,i}^2 + k_{y,i}^2}$ can be written as transverse wave number $k_\parallel$. When k_i is real and larger than $k_\parallel$, we have a plane wave that is propagating at an angle θ, with

$$k_\parallel = k_i \sin\theta, \tag{3.23}$$

where θ is the angle of emission in medium N and as a result:

$$k_{z,i} = \sqrt{k_i^2 - k_i^2 \sin^2\theta}, \tag{3.24}$$

If $k_\parallel > k_i$ then we have an evanescent field in the last medium and therefore the far-field would be zero. With these parameters, one can calculate the Fresnel coefficients for each layer i incident on adjacent layer $i \pm 1$ [59]:

$$r^p_{i,i\pm1} = \left[\frac{k_{z,i}}{n_i^2} - \frac{k_{z,i\pm1}}{n_{i\pm1}^2}\right] \Bigg/ \left[\frac{k_{z,i}}{n_i^2} + \frac{k_{z,i\pm1}}{n_{i\pm1}^2}\right], \tag{3.25}$$

$$r^s_{i,i\pm1} = \frac{k_{z,i} - k_{z,i\pm1}}{k_{z,i} + k_{z,i\pm1}}, \tag{3.26}$$

$$t^p_{i,i\pm1} = 2k_{z,i} \Bigg/ \left[\frac{k_{z,i}}{n_i^2} + \frac{k_{z,i\pm1}}{n_{i\pm1}^2}\right], \tag{3.27}$$

$$t^s_{i,i\pm1} = 1 + r^s_{i,i\pm1}. \tag{3.28}$$

Consequently, the normalized angular distribution of the radiated power P (normalized to the emitted power of a dipole in an infinite medium with refractive index n_m) transmitted into region N at an angle θ in the far-field is given by [60]:

$$P(\theta) = \frac{n_N^2 k_0^2 cos(\theta) U}{\pi}, \tag{3.29}$$

where U is the normalized transmitted power density, which describes the modified wave amplitude due to Fresnel's coefficients. U depends on the orientation of the dipole, and is related to the vertical (V) and horizontal (H) power density according to:

$$U = U_V \cos^2 \alpha + U_H \sin^2 \alpha, \tag{3.30}$$

where

$$U_V = \frac{3\sqrt{n_m} k_{\parallel}^2 |1 + a_z^p|^2 |t_{m,N}^p|^2 \mathrm{Re}[\frac{k_{z,N}}{\sqrt{n_N}}] e^{-2\mathrm{Im}[k_{z,m}]z_0}}{8k_m^3 |k_{z,m}^2| |1 - a^p|^2}, \tag{3.31}$$

$$\begin{aligned} U_H = & \frac{3\sqrt{n_m} |1 - a_z^p|^2 |t_{m,N}^p|^2 \mathrm{Re}[\frac{k_{z,N}}{\sqrt{n_N}}] e^{-2\mathrm{Im}[k_{z,m}]z_0}}{16k_m^3 |1 - a^p|^2} \\ & + \frac{3|1 - a_z^s|^2 |t_{m,N}^s|^2 \mathrm{Re}[\frac{k_{z,N}}{\sqrt{n_N}}] e^{-2\mathrm{Im}[k_{z,m}]z_0}}{16|k_{z,m}^2| |1 - a^s|^2}. \end{aligned} \tag{3.32}$$

Here, $a_z^{s,p}$ and $a^{s,p}$ are the expressions for multiple reflections in the emitter layer:

$$a_z^{s,p} = r_{m,M}^{s,p} e^{2ik_{z,m}(d_m - z_0)}, \tag{3.33}$$

$$a^{s,p} = r_{m,M}^{s,p} r_{m,N}^{s,p} e^{2ik_{z,m}d_m}. \tag{3.34}$$

In this theory, the absorption of the active medium is not taken into account. These equations have been used for the simulations in the next subsection and Sec. 4.2.

3.2.1 Dielectric and metallo-dielectric planar antenna

A famous example of a molecule sandwiched between two dielectric layers is when a solution containing the fluorescent molecules is dropped on a glass coverslip and detected with a microscope. The refractive index of the solution and the glass coverslip is n_m and n_N, respectively. To prevent the solution from drying and improve the signal, another coverslip with a lower refractive index (n_M) can be placed on the solution as shown in Fig. 3.5(a). This structure provides a dielectric planar antenna.

It is shown that most of the emission is directed into the high-index medium with the emission angle close to the critical angle [54]. Therefore, in a dielectric antenna, it is essential that $n_m < n_N$. By choosing a proper ratio between n_m and n_N one can beam the light toward the detectors. Moreover, it is also possible to reduce the angle of emission by adding layers with a higher refractive index below the high-index medium. However, this may increase the loss due to the reflection at interfaces and scattering in the medium.

Another method for beaming the emitted light is to change the distance between two dielectric materials. In Fig. 3.5, we simulate the radiation pattern of such an antenna for different distances between two glasses with $n_N = 1.51$ and $n_M = 1.45$.

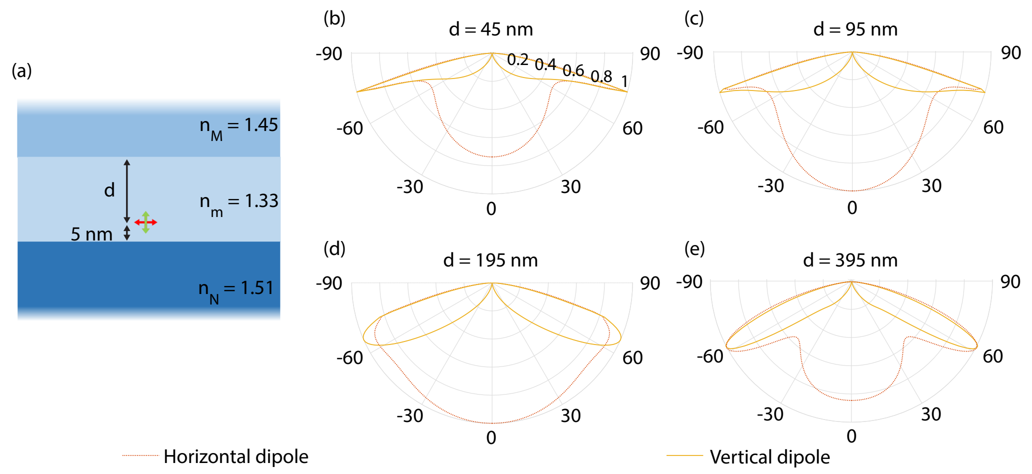

d	45 nm	95 nm	195 nm	395 nm
P^H_{rad}	0.64	0.65	0.70	0.73
P^H_{tot}	1.07	1.07	1.08	1.07
P^H_{rad} / P^H_{tot}	0.59	0.60	0.65	0.68

d	45 nm	95 nm	195 nm	395 nm
P^V_{rad}	0.98	0.89	0.90	1.00
P^V_{tot}	1.51	1.40	1.34	1.34
P^V_{rad} / P^V_{tot}	0.64	0.63	0.67	0.74

Figure 3.5: ***Light intensity and radiation pattern of a dipole emitter in a dielectric planar antenna.*** *(a) Simulation layout of a dipole emits at 680 nm in the dielectric antenna configuration. (b-d) The radiation pattern of horizontal (dashed red) and vertical (solid green) dipole at different d distances. The tables indicate the radiated power* P_{rad} *and total power* P_{tot} *of the horizontal (H) and vertical (V) dipoles in the antenna for different antenna gaps.*

The active medium is water with $n_m = 1.33$. In the experiment, one can change the gap between glasses using a piezo controller or $\mathrm{SiO_2}$ beads with different sizes.

The radiation pattern of a horizontal or vertical dipole is represented in Fig. 3.5(b-d) with red dashed and green solid lines, respectively. The vertical dipole emits at a high angle for all distances (d), whereas the emission angle of the horizontal dipole can vary depending on the distance between the dipole and the top layer. The tables in Fig. 3.5 represent the radiated power P_{rad} and total power P_{tot} of the horizontal (H) and vertical (V) dipoles in the antenna for different distance d. Dividing the P_{rad} by P_{tot} determines the antenna efficiency at each distance. Although the antenna efficiency may not change significantly for different distances or polarizations, the radiation pattern will be visibly altered. Therefore, any modifications to the antenna will affect its radiation pattern and potentially impact its overall performance. For example, the antenna efficiency of the horizontal dipole is around 60% in all distances, but the radiation pattern at $d = 95$ nm is more centralized.

By placing a metal layer (a reflector) on top of the planar antenna structure, the upward emitted light is not only reflected but also causes the radiation pattern to contract to a smaller angle on the detection side (downward). This occurs as a result of constructive interaction between the emission of the dipole and the emission of its image along the optical axis direction. As the emission angle increases, destructive interaction occurs (see Fig. 3.6). We calculate the dipole's radiation pattern at the same condition as for the dielectric antenna (Fig. 3.5) except the fact that the top glass layer is replaced with a semi-infinite gold mirror with the complex refractive index of $\mathrm{n}_{\mathrm{Au}} = 0.306 + 4.020i$ [61].

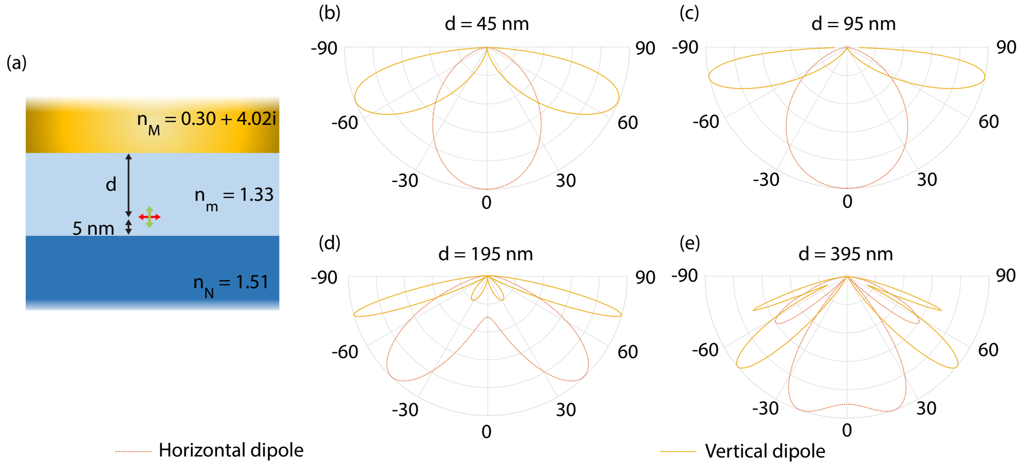

d	45 nm	95 nm	195 nm	395 nm
P^H_{rad}	0.70	1.20	1.20	1.15
P^H_{tot}	0.85	1.25	1.24	1.18
P^H_{rad} / P^H_{tot}	0.82	0.96	0.97	0.97

d	45 nm	95 nm	195 nm	395 nm
P^V_{rad}	1.27	1.14	0.84	1.19
P^V_{tot}	4.34	2.37	1.19	1.36
P^V_{rad} / P^V_{tot}	0.29	0.48	0.71	0.87

Figure 3.6: ***Light intensity and radiation pattern of a dipole emitter in a metallo-dielectric planar antenna.*** *(a) Simulation layout of a dipole emitting at 680 nm in the dielectric antenna configuration. (b-d) The radiation pattern of a horizontal (dashed red) and a vertical (solid green) dipole at different d distances. However, the directionality is higher for such an antenna, it is more sensitive to the distances between layers as compared to the dielectric antenna.*

For the metallo-dielectric antenna, the distance is more sensitive than the dielectric antenna, which is notable for radiation pattern changes in Fig. 3.6 (b-d). The experimental results and the corresponding theoretical calculations of the emission of a CdSe/CdS quantum dot in a metallo-dielectric antenna are presented in Fig. 3.7.

3.2.2 Planar Yagi–Uda antenna

Adding two layers of metal to a planar antenna, such that the dipole is sandwiched between the metal layers, creates a structure similar to a Yagi–Uda antenna. In this

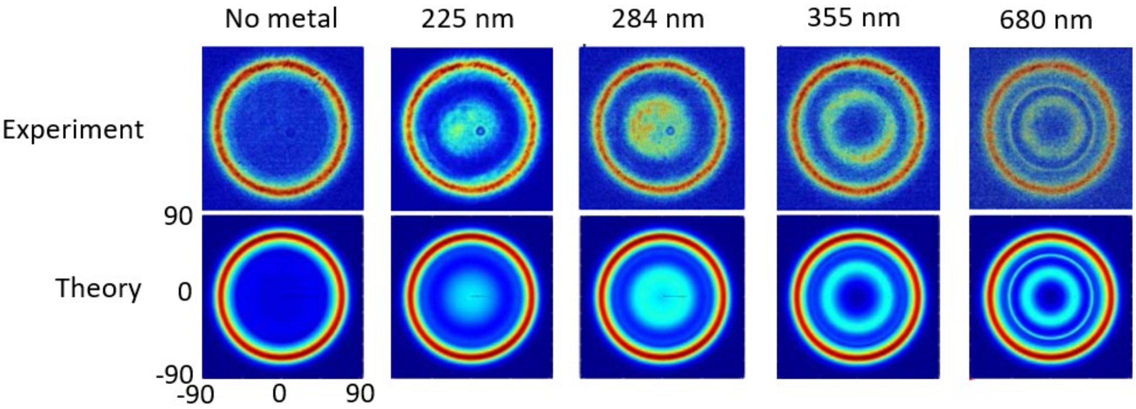

Figure 3.7: ***Theoretical and measured back focal plane images of the fluorescence of a single quantum dot in the metallo-dielectric antenna.*** *Left image is without the metallic mirror and the others are in the presence of the mirror at distances of d = 225, 284, 355, and 680 nm, respectively, from the top surface of the dielectric antenna. Adopted with permission from [58] © Optica Publishing Group*

case, one layer has a larger thickness to reflect the emission known as the reflector and the other one is a very thin layer (5-30 nm) known as the director. The director, depending on its thickness, is partially transparent and the emission will be detected from that side. Changing the thickness of the director can enhance the directionality but on the other hand, it will reduce the radiated power due to higher absorption and reflection of the metal.

Intuitively, in a Yagi–Uda antenna the image dipole is induced in the reflector by the source. When the dipole and its image radiate with an appropriate phase difference, which is controlled by the distance d_1 (see Fig. 3.8), they constructively interfere in the forward direction, resulting in a beaming effect. The excitation of the director element by the source can provide a dipole that radiates in phase with the source (depending on the distance d_2) and it provides even further enhancement in the directionality of the antenna.

The simulation and the experimental results of such an antenna based on Eq. 3.29 are presented in Ref. [22] for a fixed antenna and later in Sec. 4.2 for a scanning planar antenna. In Ref. [22], a molecule of dibenzoterrylene (DBT) embedded in anthracene (Ac) with spacer layers of hydrogen silsesquioxane (HSQ) and polyvinyl alcohol (PVA) sandwiched between two thin gold layers (Fig. 3.9(a)). This structure provides a planar Yagi–Uda antenna, that directs the emission (see BFP image in Fig. 3.9(b)). Here, the overall antenna thickness is kept constant ($d_1 + d_2 = 200$).

Fig. 3.9(c) determines the normalized collected power in the antenna, half antenna (without director), and on a glass coverslip in theory. Here, P_{hom} is the dipole power in a homogeneous environment. $P^{(\text{refl.+dir.})}_{\theta=24^\circ}$ and $P^{(\text{refl.+dir.})}_{\theta=90^\circ}$ are the normalized

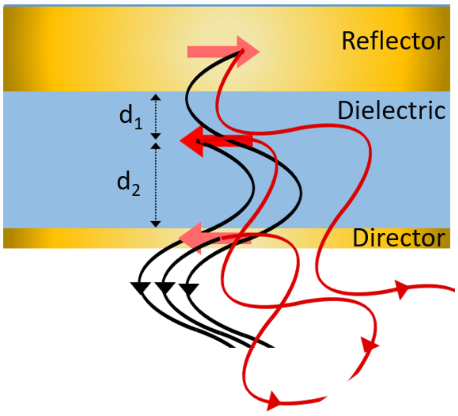

Figure 3.8: ***Principle of the planar Yagi–Uda antenna.*** *A horizontal dipole is sandwiched between two layers of metal. The emission of the dipole and its images in the reflector and director interfere constructively (black lines) in the forward direction and enhance the fluorescence signal. The emission in other directions faces a phase difference causing destructive interference (red lines).*

collected power up to 24° and maximum collection (90°), respectively. The graph also shows the normalized total power emitted in the antenna structure ($P_{\mathrm{tot}}^{(\mathrm{refl.+dir.})}$), which corresponds to the Purcell factor. In such an antenna, the modification of decay rates can be greater than in metallo-dielectric planar antennas, which enhance the fluorescence signal at the antenna resonance. This enhancement is presented by comparison of maximum collected power without ($P_{\theta=90^\circ}^{(\mathrm{refl.})}$) and with ($P_{\theta=90^\circ}^{(\mathrm{refl.+dir.})}$) the director layer. $P_{\theta=90^\circ}^{(\mathrm{glass})}$ is the maximum collected power when the dipole is located on a glass coverslip without any extra layer. The results present the advantage of a planar antenna for detecting a single emitter.

Although the simple geometry and directional outcoupling of a planar Yagi–Uda antenna make it promising for light emission applications, the existence of surface plasmon polaritons (SPPs) at the interface between the metal films and the dielectric layers, especially for high refractive index dielectrics, appears as a restriction on the outcoupling efficiency. This phenomenon has been studied for silicon-vacancy in diamond (Si-V) in [62].

A practical solution to suppress the SPP and enhance the outcoupling efficiency in such an antenna is adding intermediate dielectric layers with a lower refractive index between the active medium and the metal films. Figure 3.10 presents two planar antenna configurations for detecting a horizontal dipole in a diamond. In Fig. 3.10(a), the Metal films (silver) are in contact with the active medium (diamond), and in Fig. 3.10(b), two intermediate glass layers have a refractive index lower than that of the diamond at each side of the active medium. The antenna designs are evaluated by calculating P_{tot} and P_{rad}, both in terms of power densities

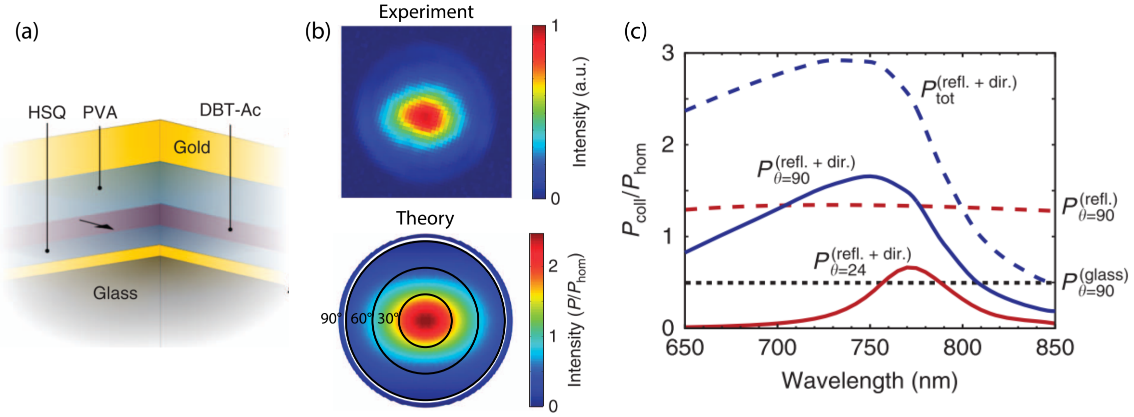

Figure 3.9: ***Detection of a DBT molecule in a planar antenna structure.*** *(a) Layout of the sample containing a DBT-Ac film inside the planar optical antenna. (b) Theoretical and measured BFP image of DBT. (c) Normalized collected power $P_{\text{coll}}/P_{\text{hom}}$ up to θ=24° (red solid curve) and θ=90° (blue solid curve) as a function of wavelength for d_1 = 130 nm. $P_{\text{coll}}/P_{\text{hom}}$ up to θ=90° is also shown for a Hertzian dipole in glass (black dotted curve) or 130 nm from a gold reflector (red dashed curve). dir., director; refl., reflector. Adopted with permission from [22] © Light: Science & Applications.*

as a function of the in-plane wavevector (k_{p}). The antenna efficiency η is equal to $P_{\text{rad}}/P_{\text{tot}}$. In Fig. 3.10(c), the power density per unit ($\mathrm{d}k_{\text{p}}^2$) associates with P_{tot} for both structures as a function of the normalized in-plane wavevector k_{p}/k_0 is presented. Here, k_0 is the wavevector corresponding to $\lambda = 738$ nm in the collection medium.

In such an antenna, power radiated in the collection medium peaked at small in-plane wavevectors for $k_{\text{p}} < k_0$. The SPP mode bound to the director in the collection medium peaked near k_0 for $k_{\text{p}} > k_0$. Two nearly degenerate SPP modes bound to the director in the active medium and to the reflector peaked between $3k_0$ and $3.5k_0$, for $k_{\text{p}} > 2.4k_0$, where 2.4 is the refractive index of a diamond. Figure 3.10(c) determines the suppression of the SPP director peak in the antenna configuration with intermediate layers.

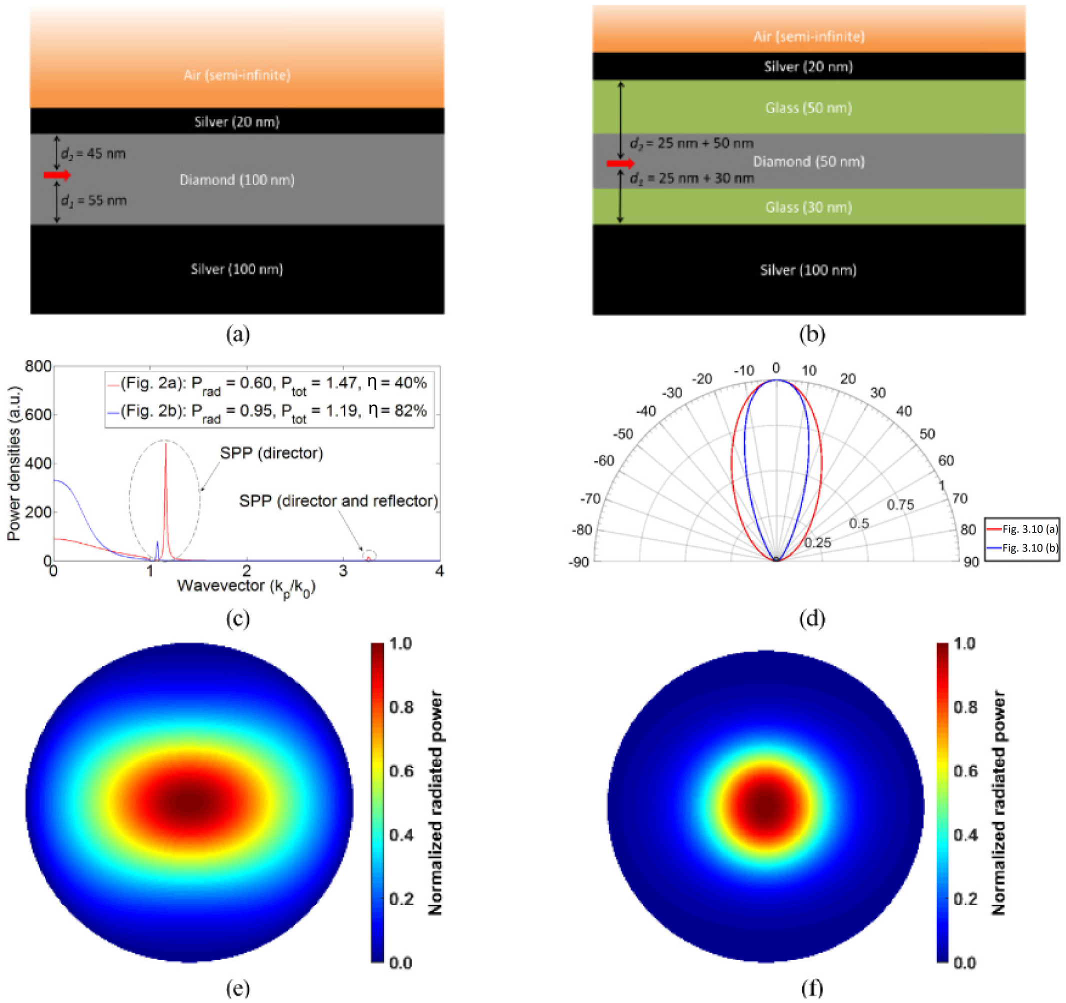

Figure 3.10: ***Improving outcoupling efficiency and directionality.*** *Planar Yagi–Uda antenna structure (a) without and (b) with intermediate glass layers. (c) Power density for* P_{tot} *as a function of the in-plane wavevector* k_{p} *and (d) Normalized radiation pattern integrated over the azimuthal angle for each configuration. The peaks in (c) correspond to the excitation of SPPs. (e) and (f) Normalized radiation patterns for the configurations depicted in (a) and (b). Adopted with permission from [62] © Optica Publishing Group.*

Chapter 4

Detection of fluorescent molecules in a scanning planar Yagi–Uda antenna

By scanning the distance between the director and reflector of a planar Yagi–Uda antenna in a controlled manner, one unravels the optical properties of the antenna in determining the fluorescence signal. This allows us to understand the functionality of such a system better. In this chapter, the experimental setup and the fabrication of the planar Yagi–Uda antenna is explained. Afterward, we investigate the excitation enhancement, decay rate, and radiation pattern of a scanning planar Yagi–Uda antenna. The results indicate that the antenna not only improves the directionality of fluorescent light but also increases the emission rate of fluorophores. To emphasize the advantage of directed emission, the collection efficiency of nanoscale sources with low-NA optics in the planar antenna is considered. Such an antenna can operate in any transparent solid, liquid, or gaseous environment, which makes it a good candidate for optical biosensing applications. Here, we also look into the collection enhancement and the limitation of our planar antenna for detecting dye-labeled DNA molecules in a buffer.

4.1 Microscope head design

A key factor for a scanning planar Yagi–Uda antenna setup is the distance between the reflector and the director, which is normally a few hundred nanometers. However, controlling such a distance is technically a challenge. Here, a home-built setup, which can hold the reflector (or the director) and move it in a controlled manner, is introduced. Since this part is attached to the top part of an inverted microscope (Zeiss Axio Observer 3), we call it the ”microscope head” in the rest of the text.

The microscope head consists of two main parts: a fiber (wire) positioner and a tilted microscope (Fig. 4.1(a)). The positioner is a combination of the xyz stage (Newport M-461-XYZ-M), tip-tilt stage (Newport M-561-TILT), and a fiber holder (Newport 466A-750), which can control the position and the angle of a bare fiber or a thin gold wire (80-250 μm). Moreover, the z-axis of the positioner is connected to a piezo fine adjustment stage (Newport NPM140SG) and controlled by a piezo stack amplifier (Newport NPC120SG). This allows us to program the fiber's (wire's) movement, which is required for measuring the distances between the reflector and the director. (Fig. 4.1(b))

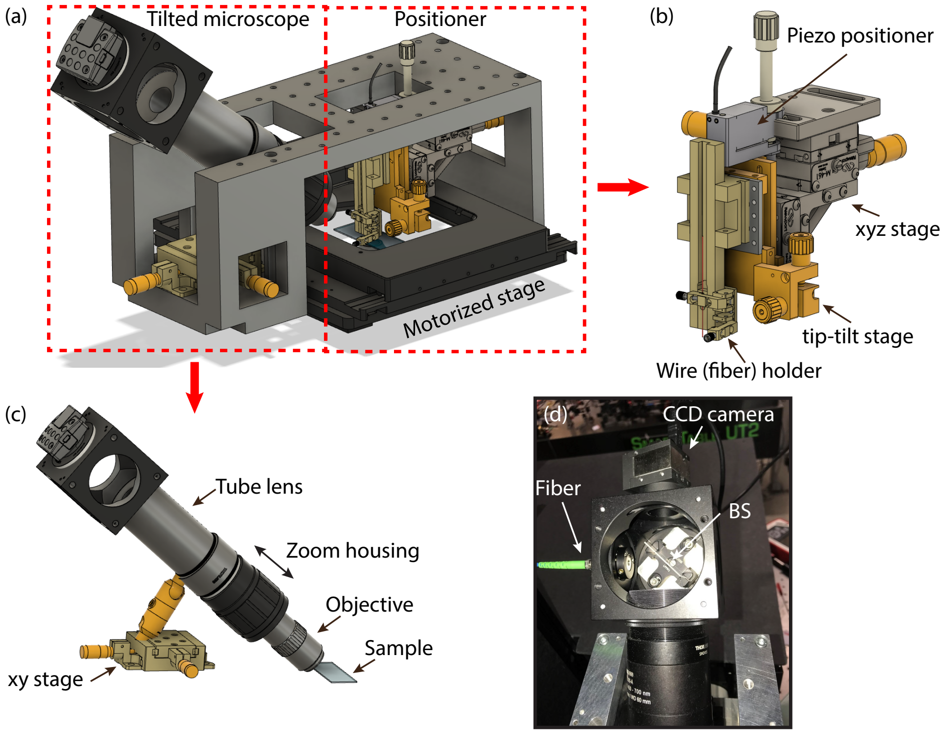

Figure 4.1: ***Scheme of microscope head.*** *(a) The tilted microscope images the location of a fiber (wire) with 10X magnification, and the positioner controls the position of the fiber with the nanometer resolution. (b) The positioner is a manual 5-axis stage in which the z-axis is controlled by an extra piezo stack. A fiber holder can hold any bare fiber or wire with a diameter in the range of 80-250 μm. (c) The tilted microscope monitors the fiber (wire) position in order to avoid the fiber-sample collision. Different parts of this microscope are mentioned in the figure. (d) Image of the cube box in the tilted microscope. The polarization-maintaining fiber and the beamsplitter are marked in the image.*

The other part of the microscope head is a tilted microscope, which contains an objective (Mitutoyo 10X Plan Apo Infinity Corrected Long WD), a zoom housing for focusing (Thorlabs Non-Rotating Zoom Housing SM2NR1), a tube lens (Thorlabs TTL100-A), a connection cage cube (Thorlabs LC6W - 60 mm), and a CCD camera (Thorlabs DCC1240C). To be able to change the tilting angle of the microscope, a flex lock optical post (Newport 9940-M) connected the microscope tube to a xy manual stage (Newport M460-A XY) as shown in Fig. 4.1(c). By inserting a 30:70 (R:T) beam splitter (BS) into the connection cage cube on top of the tilted microscope and attaching a polarization maintaining single mode fiber (Thorlabs: P3-630PM-FC-2) to the side of the cube (Fig. 4.1(d)), the tilted microscope is able not only to monitor the fiber-sample distance but also excite the sample. To facilitate detection, the refracted light emanating from the sample and the fiber tip is collected by the tilted objective and subsequently detected by the CCD camera. This occurs after the light has passed through the BS. On the other hand, the light outcoupled and collimated with a fiber lens collimator impinges the BS, which reflects 30% of the light towards the tilted objective. This angled excitation, along with the inverted microscope, provides a dark field microscope system. It can also be used to excite a sample via surface plasmon excitation (see Sec. 6.1). Figure 4.2 shows the side view of the inverted microscope and the microscope head. The excitation laser is coupled to the rear port of the microscope and reflected toward the objective via a dichroic mirror (Semrock FF660-Di02-25x36). This setup combines confocal microscopy, fluorescence lifetime microscopy, dark-field microscopy, epifluorescence microscopy, and scanning planar antenna. The other part of the optical setup is explained in Sec. 4.2

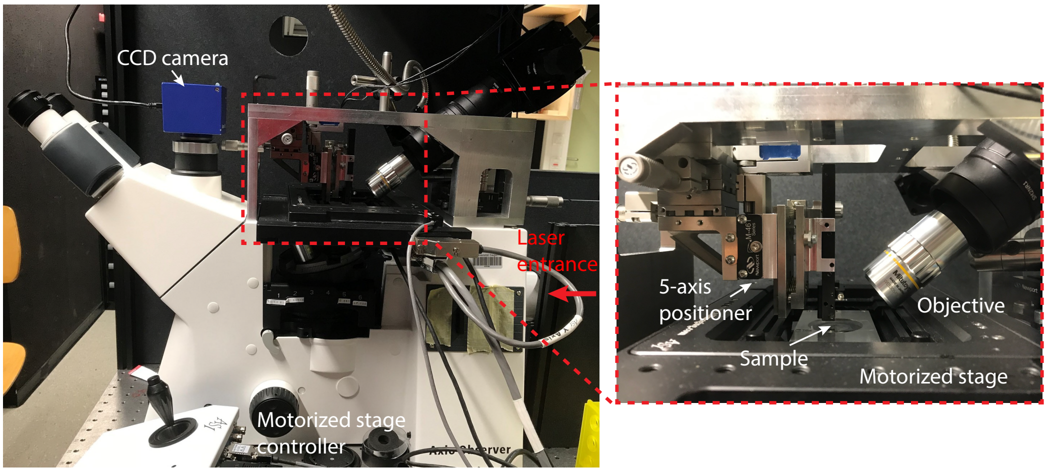

Figure 4.2: ***Image of Axio Observer microscope and the microscope head.*** *The 5-axis fiber positioner and tilted microscope are attached to an aluminum holder and connected to the microscope. The laser is coupled into the microscope from the rear port and reflected toward the sample by a dichroic mirror. A motorized stage can control the position of the sample. A ZEISS CCD camera is connected to the trinocular of microscope to monitor the position of a fiber. Inset, a zoom in the central part of the microscope head, where the sample is located.*

4.2 Article I: Scanning planar Yagi–Uda antenna for fluorescence detection

Bibliographic Information

N. Soltani, E. Rabbany Esfahany, S. I Druzhinin, G. Schulte, J. Müller, F. Sledz, A. M. Flatae, B. Butz, H. Schönherr, N. Markešević, and M. Agio, "Scanning planar Yagi–Uda antenna for fluorescence detection," Opt. Soc. Am. B 38, 2528–2535 (2021).

Author's contribution

The author contributed to sample preparation, experiment and data analysis, drafting of the manuscript, and revisions.

Copyright Notice

Abstract

An effective approach to improve the detection efficiency of nanoscale light sources relies on a planar antenna configuration, which beams the emitted light into a narrow cone. Planar antennas operate like optical Yagi–Uda antennas, where reflector and director elements are made of metal films. Here we introduce and investigate, both theoretically and experimentally, a scanning implementation of a planar antenna. Using a small ensemble of molecules contained in fluorescent nanobeads placed in the antenna, we independently address the intensity, the radiation pattern, and the decay rate as a function of the distance between a flat-tip scanning gold wire (reflector) and a thin gold film coated on a glass coverslip (director). The scanning planar antenna changes the radiation pattern of a single fluorescent bead, and it beams light into a narrow cone down to angles of 45° (full width at half maximum). Moreover, the collected signal compared to the case of a glass coverslip is larger than a factor of 3, which is mainly due to the excitation enhancement. These results offer a better understanding of the modification of light-matter interaction by planar antennas, and they hold promise for applications such as sensing, imaging, and diagnostics.

Introduction

Despite advances in the fields of optics and nano-optics, the detection of fluorescent molecules remains a big challenge. In general, low excitation cross-sections at room temperature, low quantum yields of molecules, and their dipolar emission patterns are only some of the problems that we have to face to detect low fluorescence signals. To overcome these issues, a lot of different techniques have been developed over the years, ranging from simple ones such as the use of high numerical aperture (NA) mirrors and objectives [63, 64] to the complicated fabrication techniques for creating nanostructures that can change the optical properties of the emitters and facilitate their detection, such as optical microcavities [65, 66], photonic nanowires [67, 68] and nano-antennas [69, 70]. For example, in the vicinity of plasmonic nanoparticles illuminated by laser light, the excitation intensity can increase by orders of magnitude [71, 72]. In addition, plasmonic particles spectrally matched with fluorescent molecules can also increase the emission rate as well as the quantum efficiency, making them significantly brighter [73–76]. It is also well known that some of these structures operate like antennas to change the radiation pattern of emitters and make them radiate into smaller angles [77–80]. For example, a single quantum dot coupled to a Yagi–Uda nano-antenna shows strongly polarized and highly directional luminescence [81]. However, the production of these nano-objects demands complicated fabrication techniques and precise positioning of the emitters in the antenna's hotspot.

Recently, a high collection efficiency of up to 99% from a single molecule has been demonstrated with dielectric [82] and metallo-dielectric [58] planar antennas. Since a planar antenna has a broadband resonance, the position of the emitter is not crucial, and the fabrication of planar structures is relatively simple and straightforward. However, these antennas direct the radiation towards the microscope objective at wide angles, which requires a high-NA objective for efficient collection.

A planar Yagi–Uda antenna, which consists of two thin metallic films, a reflector, and a director, not only beams the radiation pattern into smaller angles but also enhances the emission rate of a molecule [22]. In this system, the distance from the emitter to the reflector is not a sensitive parameter, and it can vary between $\lambda/6n$ to $\lambda/4n$ where n is the refractive index of the medium between them. This type of antenna can also enhance the collection efficiency for light sources embedded in high-refracting index materials [23, 62].

So far, planar Yagi–Uda antennas have been designed to operate in a fixed configuration, and the emitters are embedded in a solid matrix. However, tunable microcavities or antennas allow more operational freedom, and they can change the optical properties of emitters in a controlled manner [58, 83–86], hence offering additional possibilities and paving the way towards potential applications. In this work, we introduce and investigate a scanning implementation of a planar Yagi–Uda antenna, which could even be exploited for fiber collection [87]. Our main goal is to examine how the antenna operates as a function of the reflector-director distance and tune, for instance, the collection efficiency, the quantum yield, and the radiation pattern of a nanoscale light source. This approach can be applied to different kinds of nanoscale light sources, such as molecules, quantum dots, and fluorescence beads, and it can be operated in different environments, such as in water or at cryogenic temperatures. Therefore, it represents a novel platform for enhanced spectroscopy and sensing.

Layout of the problem and simulation results

Although previous works simulate the radiation pattern and the maximum collection efficiency for the optimal distance between the emitter and the antenna elements [22, 62], we extend this approach and simulate the parameters for continuous reflector-director distances even larger than $2\,\lambda$ (up to 1.5 μm). Moreover, in a realistic simulation of fluorescence detection, one should also consider the excitation enhancement and the emission quantum efficiency of the molecule (η_0). Therefore, we examine the collection efficiency of a dipole in a scanning planar antenna excited by a plane monochromatic electromagnetic wave.

We take into consideration only horizontal projections of the dipole moments of emitters since the vertical ones are strongly coupled to the surface plasmon polariton modes of the metal films, and they do not contribute to the emission in the far field [22]. Thus, for emitters with random orientation, the coupling efficiency would scale by a factor of 2/3 [87]. In our calculations, the gold layer, which represents the director, is 10 nm thick, and the reflector is a gold mirror movable along the z-axis. As already demonstrated, the optimal distance between the dipole and the director should be approximately between $\lambda/6n$ and $\lambda/4n$ [22]. For this reason, we need a spacer to provide such a distance in a realistic simulation. The ideal spacer should be optically transparent, and the emitters should not be quenched in its vicinity [88]. Therefore, the dipole is located 20 nm above a 75 nm thick SiO_2 layer used to separate the dipole from the director (Fig. 4.3(a)). This distance is chosen to mimic the 20 nm radius of fluorescent beads on the SiO_2 layer, which we model as a single dipole. The parameters are calculated in the range of distances from 45 nm to 1500 nm between a semi-infinite gold mirror (reflector) and the SiO_2 layer. To simulate the realistic structure, we also consider that the director layer is on the top of a 2 nm titanium (Ti) film, which is supported by a semi-infinite borosilicate glass (Fig. 4.3(a)).

We calculate the normalized total decay rate $\Gamma_{\text{tot}}/\Gamma_0$ and the normalized radiative decay rate to the far field $\Gamma_{\text{rad}}/\Gamma_0$ by respectively considering the power dissipated and radiated by a Hertzian dipole emitting at 680 nm in the antenna configuration with respect to free space [19,89]. Here, Γ_0 represents the radiative decay rate of the dipole in a vacuum. Hence, $\Gamma_{\text{tot}}/\Gamma_0$ corresponds to the Purcell factor for an emitter with an intrinsic quantum yield $\eta_0 = 1$, and it reaches a value of about 2.8 at the first maximum (Fig. 4.3(b)). Normalization with respect to a dipole near a glass coverslip would reduce the Purcell factor by a factor of about 1.25 (average refractive index between SiO_2 and air) since the radiative decay rate change is correlated with the refractive index. We also consider the dipole excitation at a wavelength of 636 nm, which for simplicity, is assumed to be a plane wave. To estimate the enhancement of the excitation rate, we calculate the electric-field intensity $|E|^2$ at the dipole position. The plane-wave reflectivity R is also calculated to relate the excitation enhancement with this measurable quantity. We numerically solve the electromagnetic problem (computation of $|E|^2$ and R) using FDTD Solutions (Lumerical) [90] and semi-analytically (computation of the decay rates and of the radiation patterns) [59].

Figure 4.3(b) plots $|E|^2$ (dashed blue curve), normalized to its maximum value, and R (dotted blue curve), normalized to the incident power, as a function of the air gap in the planar antenna. Since we use a plane wave, both quantities oscillate with a periodicity of $\lambda/2$, where $\lambda = 636$ nm, and with a constant maximum height,

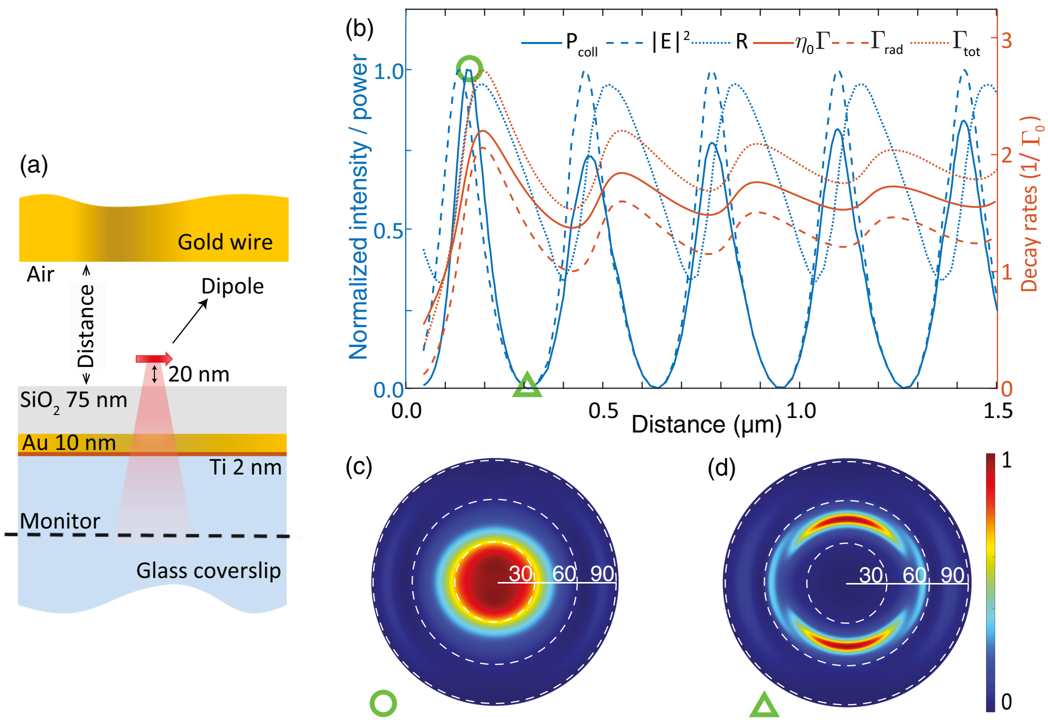

Figure 4.3: ***Hertzian dipole in a scanning planar antenna.*** *(a) Simulation layout of a dipole excited with a 636 nm monocromatic light and its emission is 680 nm in the antenna configuration. The glass coverslip and the gold wire (reflector) are semi-infinite. The values of the fixed parameters are given in the figure. The distance between the* SiO_2 *layer and the gold reflector (air gap) varies from 45 nm to 1500 nm. The reflectivity* R *and the excitation intensity* $|E|^2$ *are recorded with a frequency-domain monitor. (b) Plane-wave intensity at the dipole position,* $|E|^2$*, reflectance* R*, and collection efficiency* P_{coll} *plotted as a function of the air gap. Modification of the decay rate* Γ *(assuming a quantum yield of 0.7) as well as* Γ_{tot} *and* Γ_{rad} *also plotted as a function of the air gap. The far-field radiation patterns, corresponding to the maximum and minimum of* P_{coll}*, are highlighted with a circle and a triangle, and they are represented in (c) and (d), respectively. The FWHM of the intensity profile in (c) is 45°.*

like in a Fabry-Perot etalon. Notice that the maxima and minima of $|E|^2$ and R do not coincide, because the planar antenna is a kind of asymmetric cavity, and $|E|^2$ is calculated at the fixed dipole position, which is not at the maximum of the cavity modes.

Since we consider a detection with a high-NA objective, the collected power P_{coll} can be assumed proportional to the product of $|E|^2$ with Γ_{rad}, as we will demonstrate later, and to be nearly independent of the radiation pattern. In Fig. 4.3(b), P_{coll} (solid blue curve) is plotted for different values of the air gap between the reflector and the SiO_2 layer. P_{coll} oscillates with $|E|^2$ and Γ_{rad} and therefore, its behavior is determined by both excitation and radiation enhancement and by the radiation pattern.

When R has a minimum, P_{coll} is not maximal. It is also remarkable to note that even when $|E|^2$ is maximal, P_{coll} is not maximal for the first peak. This indicates the different contributions of $|E|^2$ and Γ_{rad} to the emission. Nonetheless, when the distance increases Γ_{rad} has a smaller contribution and P_{coll} oscillates with $|E|^2$.

To understand the role of the decay rates, Fig. 4.3(b) plots Γ_{rad} (dashed orange curve), Γ_{tot} (dotted orange curve) and the inverse excited-state lifetime Γ (solid orange curve), calculated by $(1-\eta_0)\Gamma_0/\eta_0 + \Gamma_{\text{tot}}$ for an intrinsic quantum yield $\eta_0 = 0.7$ [91], which is close to that of our fluorescent beads in the experiment.

Since the beads have an intrinsic quantum yield of 0.7, the modification of the excited state decay rate is given by $\eta_0\Gamma/\Gamma_0$. This value oscillates around 2 as shown in Fig. 4.3(b) because the normalization is with respect to a dipole in free space.

Because part of the emitted light is absorbed by the metallic elements of the antenna, it is relevant to pay attention to the antenna efficiency $\eta_{\text{a}} = \Gamma_{\text{rad}}/\Gamma_{\text{tot}}$, which represents the fraction of photons reaching the far field. This efficiency is about 0.6, and it is almost independent of the distance between the reflector and the director (not shown). Moreover, Γ_{rad} is the quantity that contributes to P_{coll} as we show here. In fact, below saturation, the fluorescence signal S is proportional to the product of intensity, quantum yield, and decay rate, i.e., $S = |E|^2\eta\Gamma$, where $\eta = \eta_0/[(1-\eta_0)\Gamma_0/\Gamma_{\text{rad}} + \eta_0/\eta_{\text{a}}]$ and Γ_0 is the radiative decay rate without the antenna. Since $\Gamma = (1-\eta_0)\Gamma_0/\eta_0 + \Gamma_{\text{tot}}$, it is easy to show that $S = |E|^2\Gamma_{\text{rad}}$. Now, considering the fact that the high-NA objective does not significantly modify the collection efficiency, we can assume $P_{\text{coll}} \simeq S$.

The far-field emission patterns of the dipole in the first local maximum and minimum of P_{coll} are shown in Fig. 4.3(c) and (d), respectively. In Fig. 4.3(c), the radiated intensity is peaked at the center and its full width at half maximum (FWHM) is 45°. On the other hand, in Fig. 4.3(d), the radiated intensity at small angles drops almost to zero.

Experimental methods

Antenna fabrication and setup configuration

To verify our theoretical predictions, we design a planar antenna according to the parameters used for the calculations in the previous section. For light sources, we choose bright fluorescent beads with a 40 nm diameter (ThermoFisher, 0.04 μm, dark red fluorescent 660/680), highly concentrated fluorescent molecules embedded in polystyrene (approximately 350 molecules), which are less prone to bleaching. Since our goal is to address individual beads, we dilute them in pure water (MilliQ 18.2 MΩ·cm resistivity) and subsequently spin-cast them on a substrate in order to obtain spatially separated beads (at least few μm mutual distance).

A planar antenna consists of two main parts, a director and a reflector. To produce the director, a glass coverslip (GCS) (PLANO, L42342 Stärke #1) is firstly coated with 2 nm titanium (Ti) [92], which played a role of an adhesion layer between the GCS and 10 nm gold film [93] (director). Furthermore, we evaporated a 75 nm SiO_2 layer as a spacer on top of Au film (similar to the structure presented in Fig. 4.3(a)). All the material deposition processes were performed by e-beam evaporation (Edwards E306A) with an evaporation rate of 0.1 nm/s. As shown in Fig. 4.4(a), 10 nm gold layer on Ti does not form uniform film but ultra-thin islands. In these kinds of structures, polarized light can excite localized surface plasmons [94].

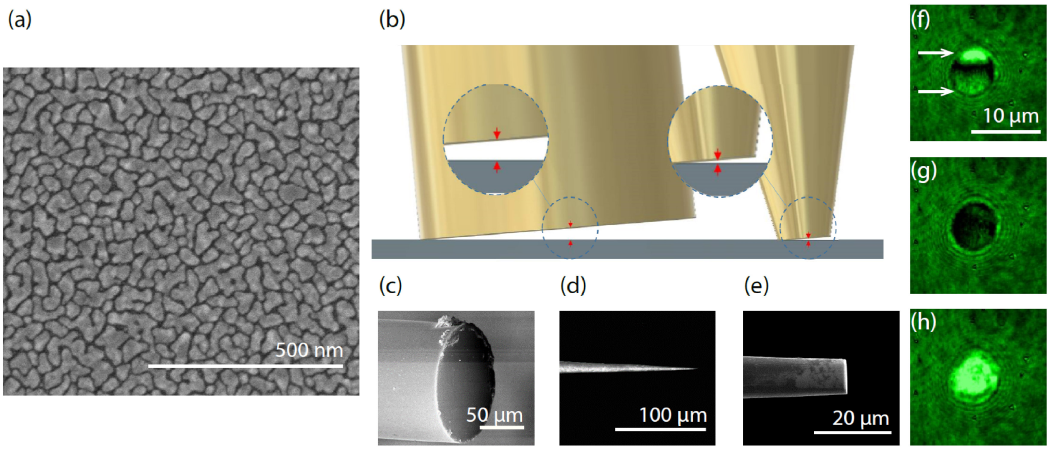

Figure 4.4: ***Fabrication of gold director and wire reflector****. (a) Scanning electron microscopy (SEM) image of a 10 nm gold layer on a glass coverslip. Instead of flat films, ultrathin islands are formed. The surface roughness of the film (director) is 10.2 nm peak to peak, which is measured by an atomic force microscope (data not shown). (b) Schematic representation of a tilted reflector before and after the thinning process. The distance from the substrate to the center of the wire varies significantly depending on the wire's diameter. The insets are magnified images of the central part, the gold wire tip, and the substrate underneath. SEM image of a gold wire (c) before and (d) after electrochemical etching. (e) SEM image of the wire tip after FIB cutting. (f) The interference pattern is formed by a tilted wire and the gold director. Since only two maxima are visible (white arrows), the estimated angle between the wire and the substrate is around 2.6°. In (g) and (h), this angle is close to zero, and thus these images represent consecutive dark and bright fringes due to 316 nm wire displacement.*

The numerical calculations indicate that the air gap between the SiO_2 layer and the gold mirror should be 160 nm to receive the maximal directional emission from a Hertzian dipole (Fig. 4.3(b)). However, we note that a small tilt angle between the reflector and substrate (Fig. 4.4(b)) can make the center gap larger than the optimal distance. One way to mitigate this issue is to reduce the diameter of the gold mirror, e.g., by etching the tip of the wire. From a simple geometrical consideration, we can easily demonstrate that even for 3° tilt angle between the wire and the substrate, the distance between the center of the reflector and the substrate is 183 nm for a 7 μm wire and 5.23 μm for a 200 μm wire diameter.

In order to obtain gold tips with a 5-10 μm diameter, we follow the procedure of Ref. [95]. Namely, we first vertically submerge a 200 μm thick gold wire (Fig. 4.4(c)) up to 1 cm into an electrolyte solution (37 % hydrochloric acid (HCl)). By applying a 3-Volt potential difference between the anode, the gold wire, and a platinum cathode, the gold wire is etched down to a cone-shaped micro-tip (Fig. 4.4(d)). Several parameters, such as the time of applying the voltage, the length of the wire inside the HCl, and the HCl concentration, play a role in the fine etching procedure. However, since we only need a sharp tip with a radius of a few micrometers, these parameters are not crucial. After the etching process in order to obtain a flat mirror, the tip of the wire is subsequently cut by Focused Ion Beam (FIB) milling (FEI Helios Nanolab 600) as shown in Fig. 4.4(e). The face diameter of the tip is determined by the position of the FIB cut. To achieve a flat tip and to avoid edge rounding at the tail of the ion beam, FIB milling is performed at 30 kV and with the smallest aperture possible while maintaining reasonable cutting times. Depending on the diameter of the wire tip, the used apertures typically result in a beam current of 0.92 nA to 2.8 nA. As FIB milling is well-suited for high-resolution electron microscopy sample preparation, the local roughness of the tip is expected to be within a few nm.

The contact point and the tilt angle can be measured by monitoring interference fringes as shown in Fig. 4.4(f)-(h). For a 7-μm gold tip and 636 nm coherent light, the minimal angle to obtain only two bright fringes is 2.6° (Fig. 4.4(f)). In the experiment, this angle can be adjusted by a manual tilting stage (Newport M-561-TILT) below this value to overcome the central gap distance (Fig. 4.4(g),(h)).

Optical setup

The optical setup is based on an epi-fluorescence inverted microscope (Supplementary Information Fig. 4.7). A pulsed laser with a wavelength of 636 nm and a repetition rate of 40 MHz (Picoquant, LDH-P-C-640B) is coupled to a commercial inverted microscope (Zeiss, Axio Observer 3) and the laser light is focused with an oil objective (Zeiss, Plan-Apochromat 63x/1.4) onto the sample. A motorized stage (ASI, PZ-2000FT) controls the position of the glass substrate with the spin-casted beads in the xyz directions in order to address a single bead. The reflector is aligned above the focal point of the objective with a home-built module on the top part of the microscope. A piezo controller (Newport, NPM140SG) moves the wire in the z-

direction in order to set the distance between the reflector and the bead positioned in the focal spot of the laser. The piezo-controller movement is monitored by a closed-loop piezo stack amplifier (Newport NPC120SG).

The fluorescence signal from a single bead is collected by the microscope objective and simultaneously sent to the CMOS camera (Andor, Zyla 4.2 Plus) and the single-photon avalanche photodiode (SPAD) (Excelitas, SPCM-AQRH-TR), with a 95:5 Transmittance: Reflectance ratio defined by a beam splitter (BS). A Time-Correlated Single-Photon Counting (TCSPC) device (PicoQuant, Pico Harp 300) measures the photon count rate. The time resolution in this experiment is less than 250 ps, which is the time resolution of SPADs. The radiation pattern is obtained by Back-Focal Plane (BFP) imaging with the CMOS camera.

The setup contains also a laser clean-up filter (CF 637/7) with a central wavelength of 637 nm and 7 nm bandwidth, a flippable wide-field lens (WFL) used for monitoring the beads in the alignment process, a dichroic mirror (DM) with a 650-nm cut-off wavelength, a long-pass (LP) and a band-pass (BP) filter (LP 650, BP 680/42, with a central wavelength of 680 nm and 42 nm bandwidth), whose position can change based on the experiment (Fig. 4.7(b)). Flip mirrors (FM1 and FM2) can send the light to the CMOS camera, the spectrometer (Ocean Optics QE pro), or to another single-photon avalanche photodiode (SPAD1). A back-focal plane lens (BFL) is used to image the radiation pattern. The inset of Fig. 4.7(a) sketches the 3D model of gold wire in the antenna configuration. The distance of the wire from the glass coverslip is monitored by a tilted objective mounted on the home-built stage such that the wire tip is clearly visible while approaching the substrate surface. For precise alignment, the tilting of the reflector is observed by the laser interference pattern also collects by the microscope objective and corrects by a manual tilt stage as described in Fig. 4.4(f-h). Moreover, the contact point between the reflector and the substrate is determined by interference fringes. Namely, once the wire and the substrate are in contact, a further attempt to approach does not result in any visible interference pattern change. We take this position as a starting point for the wire retraction.

The experiment is performed at room temperature and the vibration of the antenna system is estimated by interference patterns to around 40 nm. Therefore, in all steps, we measure the position several times and average the result. This further helps us to decrease the vertical position error to ±5 nm at each step.

Experimental results and discussion

Here, we investigate the emission pattern, the excited-state decay rate Γ, and the collected power P_{coll} for a single bead in the planar antenna configuration, as a function of the distance between the SiO_2 layer and the reflector (air gap), as shown in Fig. 4.5. The reflector position is adjusted using the piezo controller in a stepwise fashion (10 nm step size), from the contact point with the SiO_2 in 150 steps (Fig 4.5(a)). At each step, the position of the wire and the measured quantities are recorded. The vertical dashed line in Fig. 4.5(b) indicates the contact point.

In our experiment, the excitation power at the back entrance of the microscope is 3.5 μW. Since the 10 nm thick gold director has only 30% transmittance, the power passing through the director is around 1 μW. However, this is sufficient to detect the fluorescent beads and align them in the focus point of the objective using the xyz stage.

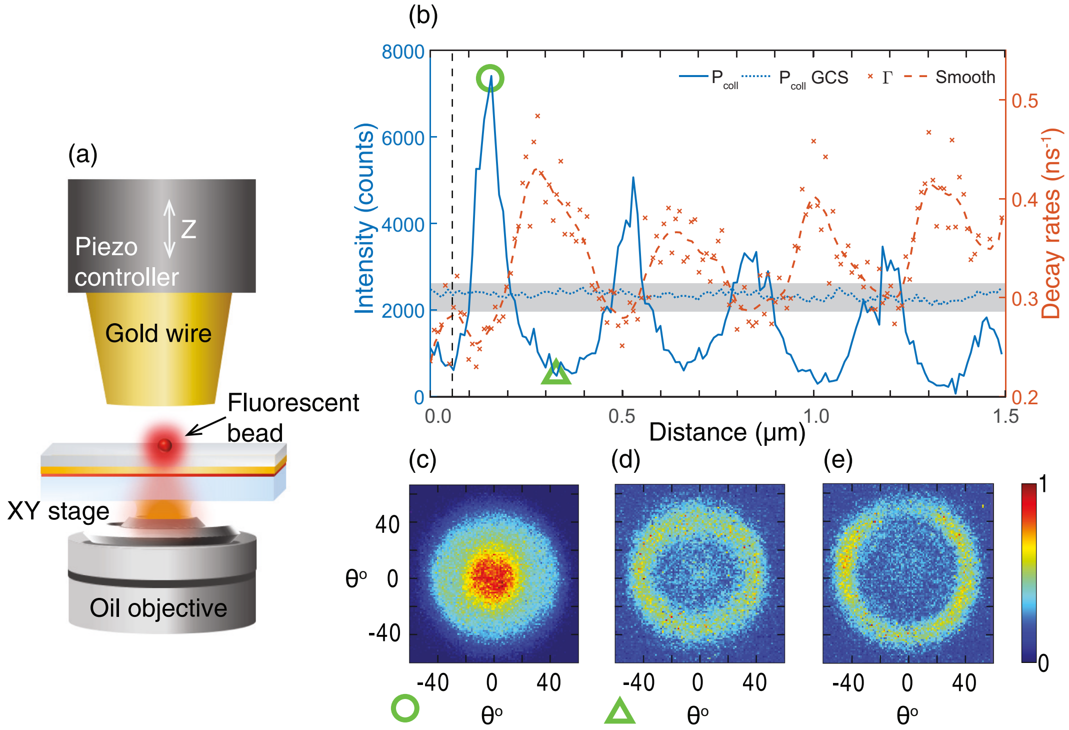

Figure 4.5: ***A fluorescent bead in the scanning antenna configuration****. (a) Schematic representation of the home-built scanning planar antenna setup. The reflector and the sample can move by a piezo controller (along Z-axis) and motorized stage (in XYZ), respectively. (b) Collected fluorescence intensity (counts) and decay rates ns^{-1} measured as a function of the distance between the reflector and the SiO_2 layer. The background intensity is subtracted. The vertical black dashed line indicates the position, where the reflector and the SiO_2 are in contact. The collection intensity of a bead on the glass coverslip (P_{coll} GCS) is shown with the blue dotted line and the range of this intensity for different beads is shown by the gray shaded area. (c,d) The radiation pattern for two selected positions is marked by a circle and a triangle. (e) The radiation pattern of a bead when the reflector is far away. Each BFP image is normalized to its maximum values.*

To determine fluorescence lifetimes at each step of the reflector position, we construct fluorescence lifetime decay histograms based on the start-stop events of the TCSPC. Using the deconvolution method, we are able to separate fluorescence from the background and reach the single exponential fluorescence decay rate (Γ) (see Supplementary Information for details). The integration of the fluorescence decay histogram determines the collected power (P_{coll}) as a function of the distance between the reflector and the SiO_2 spacer. (Supplementary Information Fig. 4.8). The variation of P_{coll} and Γ at different reflector positions are plotted in Fig. 4.5(b) with the blue line and orange crosses, respectively.

The decay rate Γ in the scanning Yagi–Uda antenna exhibits a periodic behavior with values between 0.48 and 0.27 ns^{-1}, i.e. lifetime τ is between 2.08 and 3.70 ns, and it has a phase shift with respect to P_{coll} (Fig. 4.5(b)). This is due to the fact that the decay rate increases at the cavity resonance for the emission wavelength ($\lambda \simeq 680$ nm), while the detected intensity follows the laser wavelength (excitation enhancement at $\lambda = 636$ nm) and the emission wavelength (enhancement of the radiative decay rate). The fluctuation of the decay rate, especially at low P_{coll} is mainly due to the low intensity of the fluorescence decay from a single bead as well as the lower background caused by the ultrathin gold islands (director). Although this background is deconvolved from the fluorescence signal of the bead, the signal-to-noise ratio still remains very low at the low emission intensities (Fig. 4.8).

A smoothed Γ (orange dashed curve in Fig. 4.5(b)) is obtained by averaging the decay rate at each point with its six neighbors. Moreover, by calculating the ratio between the first maximum and minimum of the smooth curve (1.6) and comparing it to Γ in Fig. 4.3(b), one can estimate the quantum efficiency of the beads, which is around $\eta_0 = 0.7$ [91,96]. The modification of the excited-state lifetime due to the Purcell factor of about 2, is in good agreement with the simulation results presented in Fig. 4.3.

The beads exhibit an emission spectrum peaked at 680 nm with a collection bandwidth of 38 nm. Although in theory (Fig. 4.3) the emitter has a fixed position (20 nm above the SiO_2) and single emission wavelength (680 nm), the agreement between theory and experiment is due to the fact that the antenna has a bandwidth of about 80 nm [22] both in terms of the spectrum and the position, and that P_{coll} is mainly modulated by the excitation rate, which for both theory and experiment corresponds to the same wavelength (636 nm).

The excited-state decay rate of the bead is about 0.29 ± 0.05 ns^{-1} on the glass coverslip (not shown). The collection intensity of a single bead on the glass coverslip (without any additional layer) is shown by the blue dotted line in Fig 4.5(b) for reference. Although the bleaching of the fluorescent molecules inside the bead can potentially reduce its emission, this effect is neglected in our experiments owing to the long bleaching time of the beads (blue dotted line in Fig. 4.5(b)).

The main reason for the reduced P_{coll} in the antenna configuration (Fig. 4.5(b)) must be attributed to the smaller excitation intensity due to the standing wave pattern formed by the laser. One should take into account that the antenna acts also as a cavity and gives rise to the intensity enhancement (blue dashed line in Fig. 4.3(b)).

Furthermore, at larger distances, the cavity resonance has a dominant effect and the signal exhibited a series of maxima and minima that follow the excitation wavelength. Since fluorescent beads contain a different number of fluorescent molecules, the emitted power of the individual beads is not the same. It is therefore difficult to compare the antenna configuration with the glass coverslip in a quantitative manner. However, a comparison of the P_{coll} in the antenna with P_{coll} for several beads on the glass coverslip, shown by a gray shaded area (Fig. 4.5(b)), demonstrates that overall the antenna enhances the fluorescence signal by more than a factor of 3. The dotted curve represents one measurement of P_{coll} of a bead on the glass coverslip.

The maximum of P_{coll} is at 0.17 μm distance and the back-focal plane (BFP) image at this position (Fig. 4.5(c)) indicates a highly directional emission. The FWHM of the emission pattern at the first maximum of P_{coll} shrinks to roughly 45°. Moreover, the emission pattern at the first minimum of P_{coll} is a ring with 70° angle (Fig. 4.5(d)), which is also in good agreement with the simulation results shown in Fig. 4.3(c,d). Since the NA of the objective is high, we can compare the measured intensity with the calculated P_{coll} shown in Fig. 4.3(b). The radiation pattern of the bead when the reflector is far away is shown in Fig. 4.5(e) and the results are consistent with earlier studies [97–99].

Inspired by the planar metallo-dielectric antennas [58, 100] we design a semi-antenna, which is a simplified version of the planar Yagi–Uda antenna (without SiO_2, gold director and Ti layers). In Supplementary Information (Fig. 4.10) we provide the radiation pattern for the single bead influenced by this antenna configuration. Comparing the radiation patterns for the planar Yagi–Uda antenna presented above (Fig. 4.5(c)) with the semi-antenna, we clearly demonstrate that even a 10 nm thick gold layer (director), with all its imperfections, can dramatically change the radiation pattern (see for comparison Fig. 4.10(c,d) and Fig. 4.5(c,d)).

To determine the relationship between R and P_{coll}, the collected light is split into two channels. We slightly modify the previous setup and, instead of a CMOS camera, we employ SPAD1 for photon detection (Supplementary Information Fig. 4.7(b)). In this case, 95% of the light is passing through a long-pass and a band-pass filter and it is detected by the SPAD1. Conversely, after being attenuated only by a neutral density (ND) filter (OD=2), the other 5% of light (laser reflection) is detected by a second SPAD (SPAD2).

Figure 4.6 plots the intensity detected by SPAD1 and SPAD2 as a function of the distance between the director and the SiO_2 layer. We note that the intensity

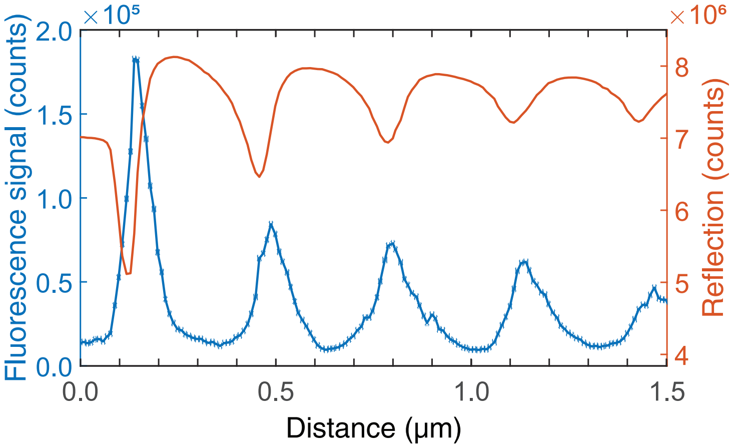

Figure 4.6: ***Fluorescence signal and laser reflection in the planar antenna configuration.*** *The fluorescence signal consisting of the bead and the director emission (blue curve) as well as the reflected laser power (orange curve) are shown as a function of the distance between the reflector and SiO_2 layer (air gap). The reflection is associated with the excitation rate, which modulates the fluorescence signal.*

from the beads is much higher than P_{coll} in Fig. 4.5(b) because in the previous configuration, only 5% of the light is collected by SPAD2, but in this configuration, 95% is detected by SPAD1.

In Fig. 4.6, the intensity (blue curve) is the convolution of the fluorescence of the bead (P_{coll}) and the background emission from gold islands. This will cause a slight shift (roughly 40 nm) in the position of the maxima of P_{coll} and increase the distance between the fluorescence and reflection peaks as compared to theory (Fig. 4.3). Since the decay histogram is not recorded in this experiment, it is not possible to deconvolve the director auto-fluorescence from the signal of the bead, as performed for Fig. 4.5(b).

The spacing between two minima of the laser reflection (orange curve) is roughly 330 nm, which should correspond to the cavity resonance at the excitation wavelength. This is slightly larger than $\lambda/2$, for $\lambda = 636$ nm. The 10 nm difference can be related to the piezo calibration and the system vibrations. The oscillation of the reflected signal gradually decreases with the air gap. This phenomenon can be simply explained by the fact that, while the laser light remains focused on the bead, the reflector is not able to refocus the incident light back into the laser mode. In our theoretical considerations, the amplitude of the reflection (R) is constant, since the excitation is a plane wave (Fig. 4.3(b)).

The distance between the first two peaks in P_{coll} (blue curve in Fig. 4.6) is different from the next ones. This is probably due to the near-field of the emission at $\lambda = 680$ nm, in combination with the intensity enhancement. Moreover, since the antenna effect has a higher impact at sub-wavelength distances ($\lambda/6n$ to $\lambda/4n$), the first maximum in P_{coll} is 2.4 times larger than the second one. On the other hand, the first minimum in R is 1.8 times deeper than the second one. By dividing these numbers we get 1.33, which is equal to the first and second peak difference of P_{coll} in theory (Fig. 4.3(b)).

As the distance increases, P_{coll} roughly follows $1 - R$, as expected from the predominant contribution of the intensity enhancement. However, in agreement with the simulation results (Fig. 4.3(b)), the maxima of P_{coll} are slightly ahead of the minima of R, because they are related to $|E|^2$.

Conclusions

We have proposed and investigated, theoretically and experimentally, a scanning planar Yagi–Uda antenna to understand better its influence on the optical properties of nanoscale light sources. Simulations and measurements of the excitation enhancement, the beaming effect, and the Purcell enhancement give us insight into the working mechanism of the planar Yagi–Uda antenna and help us optimize fluorescence collection efficiencies over a large parameter range. These physical quantities are addressed by scanning the distance between the antenna elements, the reflector, and the director. Moreover, the experimental findings are consistent and in good agreement with the semi-analytical model. The results demonstrate that at around 160 nm antenna air gap the Purcell factor is small but not negligible (around two at the first maximum), and the FWHM of the main radiation lobe at this position is 45°. Altogether, the fluorescence signal is three-fold higher than on a regular glass coverslip. A comparable improvement can also be found for larger distances.

Compared to other scanning cavity approaches [84,101,102], our method is broadband and less sensitive to the fine position control of the emitters concerning the antenna elements. Therefore, it is particularly advantageous for detecting fluorescence at ambient temperatures, where the signal is spectrally broad and it allows standard immobilization techniques of the emitters, such as spin-casting or chemical functionalization of the substrate surface. We already envision that we can easily extend this technique to detect emitters in a liquid environment.

Since planar antennas strongly influence the emission directionality, our findings suggest that this approach can be further extended to low-NA optics, particularly to low-NA objectives with long working distances. Avoiding expensive and sometimes impractical high-NA objectives would facilitate the experiments and extend the range of possible applications. Eventually, the tip of an optical fiber coated with a thin gold film (director) could completely replace the objective, and as such optical fibers would be employed both for the excitation of the emitters and fluorescence collection [87]. Hence, a scanning planar Yagi–Uda antenna holds promise for a variety of applications in fluorescence-based biosensors [103], single-photon sources [104], enhanced spectroscopy [105] and scanning microscopy [106].

Supplementary information for: scanning planar Yagi–Uda antenna for fluorescence detection

Setup configuration

The experimental setup and components are explained in the manuscript.

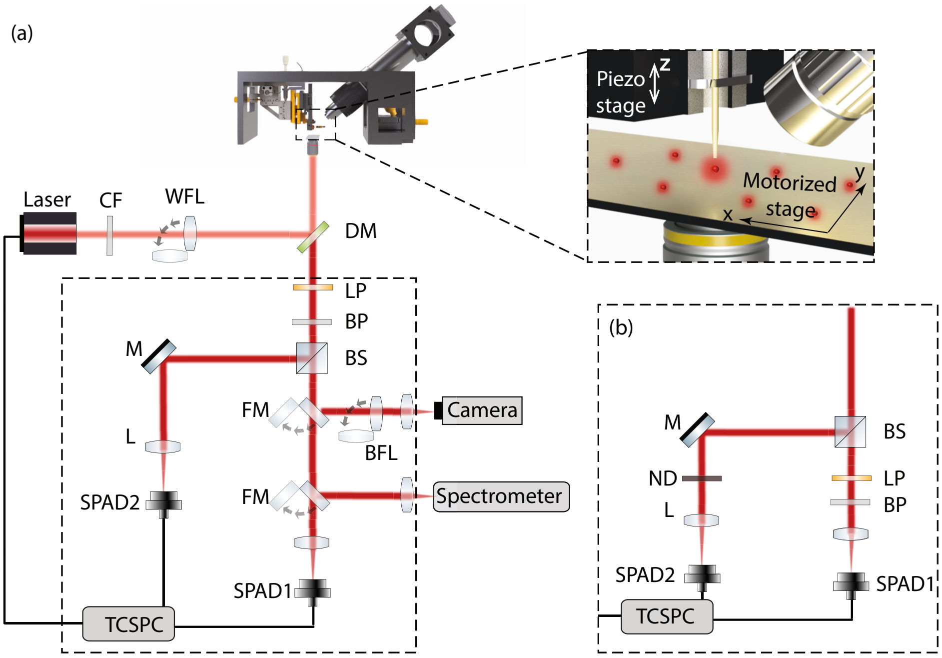

*Figure 4.7: **Scheme of the optical setup**. (a) A module complements an inverted epi-fluorescence microscope (Zeiss Axio Observer 3) for the gold wire (see the main text for a description of the setup). The inset sketches the positioning of the gold wire on top of the sample. The tilted objective monitors the distance between the wire and the substrate but also enables precise positioning of the gold wire directly above the focus. Abbreviations: CF (clean-up filter), WFL (wide-field lens), DM (dichroic mirror), LP (long-pass filter), BP (band-pass filter), BS (beam splitter), M (mirror), L (lens), FM (flip mirror), SPAD (single-photon avalanche detector), TCSPC (time-correlated Single Photon Counter), BFL (back focal plane lens) (b) Simultaneous measurement of the laser reflectance and of the fluorescence signal is performed by SPAD2 and SPAD1, respectively by placing the LP and BP after BS and removing all flip mirrors.*

Decay rates and deconvolution of the collected signal

As discussed in the manuscript, evaporated gold films (director) are not flat and ultrathin islands are formed (see Fig. 4.4(a)). Therefore, all the photons collected by the objective and detected by the detector (SPAD2) consist of two subgroups: bead fluorescence (P_{coll}) and emission from the gold director (P_{dir}). Since we are interested in bead fluorescence, the director's background is deconvolved from the fluorescence signal using the following procedure.

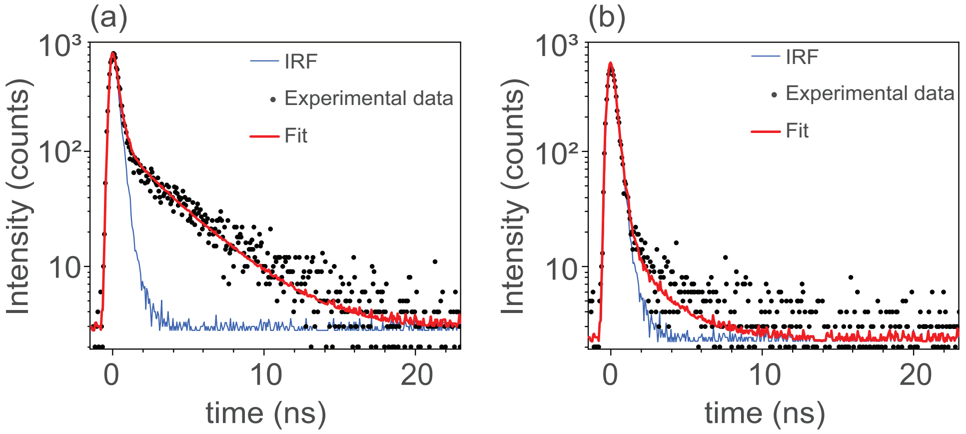

Figure 4.8: ***Experimental fluorescence decay of a bead in planar antenna configuration****. (a) Fluorescence decay at the first maximum of the fluorescence intensity. SiO_2-reflector distance d = 169 nm, decay rate Γ = 0.29 ns^{-1}, fluorescence intensity $P_{\text{coll}} = a/\Gamma$ = 6005 counts and director background intensity $P_{\text{dir}} = s\int_{-\infty}^{\infty} p(t)\,\text{d}t = 7514$ counts. (b) Fluorescence decay at the first minimum of the fluorescence intensity. $d = 329$ nm, Γ = 0.40 ns^{-1}, P_{coll} = 481 counts, P_{dir} = 6192 counts. The blue dots represent the experimental data, the orange curve shows the lifetime fit, and the black curve illustrates the instrument response function (IRF).*

The director background (P_{dir}) dominates the fluorescence signal below 2 ns, and the bead emission (P_{coll}) is visible above that value, making a reliable estimation of the decay rate Γ feasible. The response function $y_i = a\int_{-\infty}^{t_i} p(t-x)\exp(-\Gamma x)\,\text{d}x + sp_i + b$ is calculated as a sum of three elements: a convolution of the instrument response function p measured as the emission at the glass/gold interface and an exponential decay term, with its amplitude a, the reflected excitation p_i, with its amplitude s, and the remaining background b. The parameters [107, 108] for the fluorescence decay of the bead are obtained by employing a nonlinear least-squares method, with the sum of the squares of the weighted residuals $S = \sum_i w_i(y_i - y_i^e)^2$ as the target function. In the expression for S, w_i is the weighting factor, and the index i counts the experimental points for each response function, usually around 400, and the superscript "e" indicates that the quantity is an experimental value. For the fluorescence decay, the factor $w = y^{-1}$.

The histogram of photon arrival times (detected by SPAD2) is plotted at each measuring step. Figure 4.8(a,b) represent this decay histogram of a bead in planar antenna configuration when the SiO_2 surface-reflector distance is 169 nm and 329 nm, respectively.

Figure 4.9 shows the director background (P_{dir}), fluorescence signal (P_{coll}) and

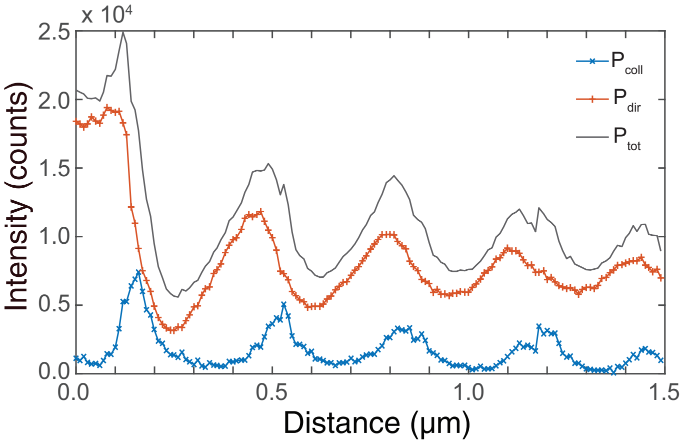

Figure 4.9: ***The director background and the bead fluorescence signal in planar antenna.*** *The total collected signal (P_{det}) is deconvolved into P_{dir} and P_{coll} using the deconvolution method for the decay histogram at each point. P_{dir} has a phase shift with respect to P_{coll} owing to different cavity and antenna resonance. This shift appears smaller for larger distances.*

the total detected photons by SPAD2, (P_{det}) which is the combination of P_{dir} and P_{coll}. Figure 4.9 clearly determines the influence of the surface plasmon emission on P_{det}. The latter is maximized in the cavity resonance. Since the resonance of the antenna and the cavity are not at the same reflector-director distance, there is an offset in peak positions of P_{dir} and P_{coll} for the first few peaks. When the wire is further retracted, the antenna effect becomes weaker, and the cavity effect is dominant.

This background can be largely avoided by improving the quality of the director, namely by evaporation of gold onto a heated substrate or post-evaporation annealing [109], which is beyond the scope of this study.

Collection efficiency with a reflector (semi-antenna)

Inspired by previous works [58,100] we investigate the emission pattern, the excited-state decay rates Γ, and the collected power P_{coll} for a single bead on a glass coverslip as a function of the distance between the bead and the reflector, i.e. gold wire (see Fig. 4.10). The scheme of such a system (semi-antenna) is presented in Fig. 4.10(a). In this configuration, the excitation power is 1 μW and the gold director (more precisely, titanium, gold, and SiO_2 layers) is not present. The low background signal eliminates the need for the BP filter, therefore we collect the entire broadband fluorescence signal. As a result, the collected intensity is higher, when compared to the same measurement with the BP filter in the antenna configuration (Roughly 2 fold higher). We repeat the same measurements as in the case of the planar antenna described in the manuscript and present our findings as a function of the air gap size between the reflector and the glass coverslip surface.

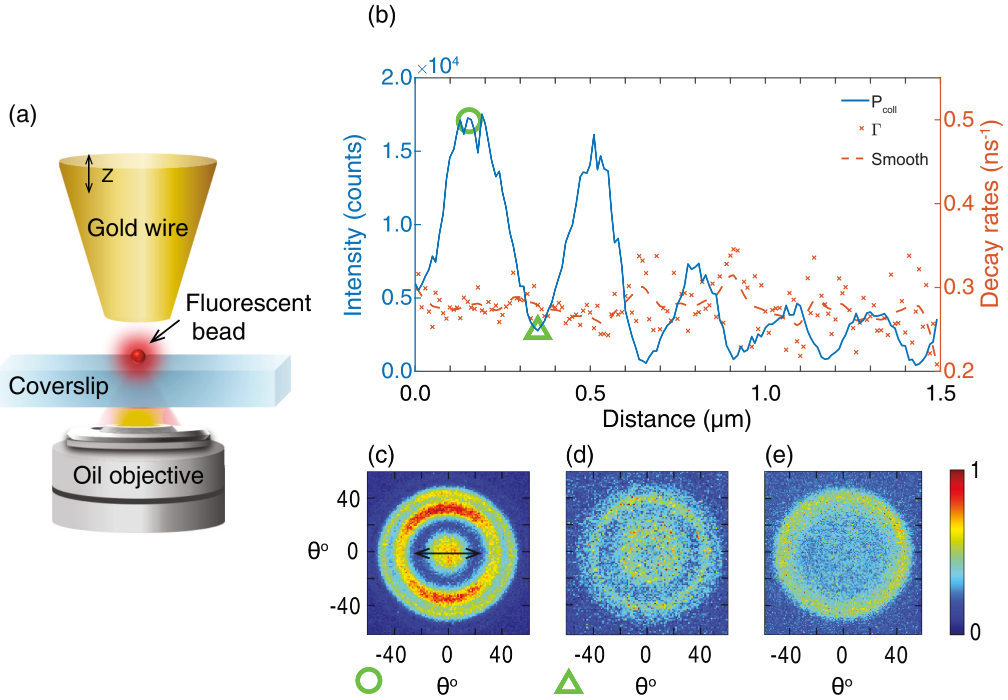

Figure 4.10: ***A movable reflector on top of a fluorescent bead on a glass coverslip****. (a) Scheme of the experimental setup. (b) Collection intensity (counts) and decay rate (ns^{-1}) are measured as a function of the distance between the reflector and the glass coverslip. The smooth line is obtained by averaging the decay rate at each step with its neighbors. (c-d) The radiation pattern for two selected positions is marked by a circle and a triangle in (a). (e) The radiation pattern of a bead on a glass coverslip without the reflector.*

In Fig. 4.10(b) blue curve (P_{coll}) shows that the number of emitted photons is maximal at a distance of 160 nm between the gold wire and the glass coverslip. The corresponding back focal plane (BFP) image of this position is shown in Fig. 4.10(c). The BFP imaging reveals the laser polarization, and it is shown by a black arrow. In this configuration, P_{coll} has its first minimum at a distance of 350 nm (Fig. 4.10(b)). Since P_{coll} is very low, it is difficult to compare these two radiation patterns in Fig. 4.10(c,d). The main reason for the reduced power at the minimum must be attributed to the smaller excitation intensity due to the standing wave pattern formed by the laser when it is reflected by the gold wire. The radiation pattern of a bead on CGS is presented in Fig. 4.10(e), which is consistent with the previous investigation [110].

As expected, the gold wire has a minor effect on the decay rate of the molecules [96]. This is illustrated in Fig. 4.10(b), when the decay rate (orange dots) has a minor change, while the wire is retracted. Moreover, Fig. 4.10(b) determines that at the low-intensity signal in the minima and at larger distances the decay rate changes in a random manner. The reason is that the low count rates give poor statistics of the photon time arrivals, therefore the fitting of the histograms gives scattered values. To guide the eye, the smooth curve is obtained by averaging the decay rate at each point with its 6 neighbors.

Directionality of planar antenna at larger distances

The emission directionality can improve even for larger reflector-director distances. In Fig. 4.11, we present the radiation patterns of the detected light (P_{det}) at the higher order maxima. However, for the third and fourth maxima (triangle and square), the background intensity has a dominant role in the BFP imaging (a factor of 2 higher than fluorescence signal) (see Fig. 4.9). Therefore, it is difficult to identify the directionality of the fluorescence signal. We repeat this experiment for an ensemble of beads in the diffraction-limited spot, which causes a higher signal-to-noise ratio and achieves the same directionality for maxima at larger distances. This property might enable the antenna to detect larger molecules or structures ($>$ 160 nm) with reasonable collection efficiency even with low-NA objectives.

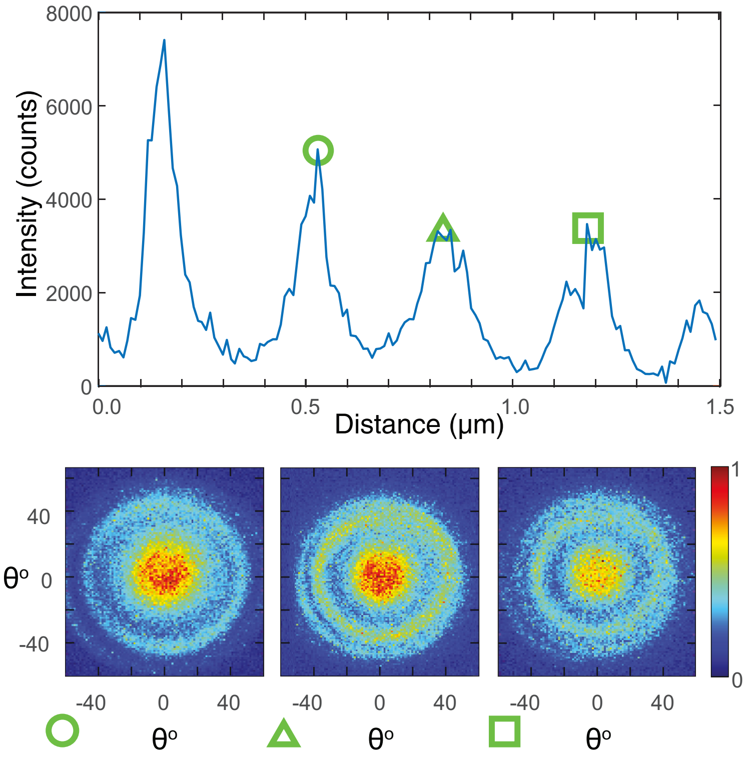

Figure 4.11: ***Radiation pattern at the higher order maxima.*** *(a) Fluorescence signal as a function of* SiO_2*-gold wire distance (air gap). (b-d) Radiation pattern at selected positions with maximal intensities (see symbols).*

4.3 Fluorescence detection using low NA objectives

Although the changes in radiation pattern do not contribute to the signal enhancement when we utilize high-NA objectives (Sec. 4.2), it becomes an important factor once we are using low-NA objectives. Figure 4.12 represents the numerical calculation of collected fluorescence signal (P_{fluo}) for different collection angles, which corresponds to NA, in the planar antenna, and on a coverslip. In this Figure, the dashed lines and the solid lines illustrate the P_{fluo} on the coverslip and in the antenna, respectively. The results determine that the fluorescence collection of a single emitter in the antenna is 2.8 times higher as compared to the emitter on the coverslip while the collection angle is 67 degrees (NA $\approx$ 0.92 for air objective). However, the ratio between maximum coupling in the antenna and coverslip for 36 degrees (NA $\approx$ 0.6) is around 10. This enhancement is only related to the emission pattern and Purcell factor in the antenna while the excitation enhancement is not considered. Similarly, the ratio for 0.5 and 0.35 NA are 11.6 and 21.2, respectively.

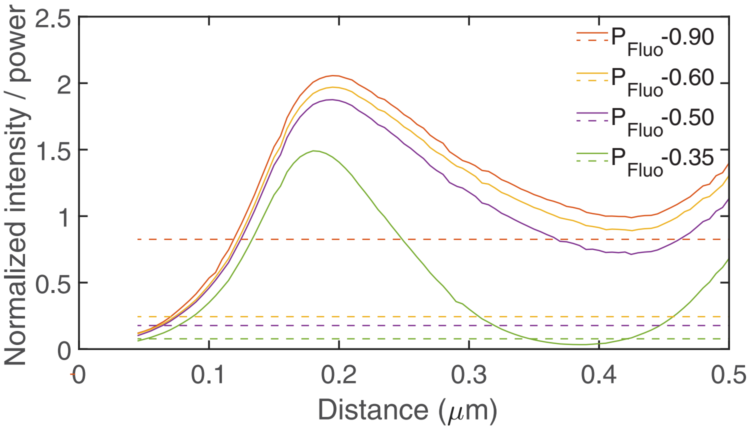

Figure 4.12: ***Collection efficiency with different NA****. The collection efficiency of a single emitter is considered as a function of the distance between the reflector and* SiO_2 *spacer for different objective NA. The Solid line and the dashed line represent the objective collection efficiency in the antenna and on a coverslip, respectively. Since the coverslip does not have a reflector, the efficiency is not changing via distance and each dashed line has a constant value.*

To demonstrate the beaming effect in the antenna setup we experimentally measure the P_{fluo} of a 40 nm fluorescence bead in the antenna and on a coverslip with a NA = 0.6 (Zeiss LD C Epiplan-Apochromat 50x/0.6 DIC M27) and NA = 0.4 (Zeiss EC Epiplan 20x/0.4) air objectives. To neutralize the variation of the fluorescence signal of each bead, we repeat the measurement 7 times with different beads and average the results in the end. Since the collected signal is a combination of fluorescent from the bead and the background (e.g. background of the gold surface), we should subtract the background from the collected signal. The method is explained in detail in Sec. 4.4. This means that having a high background can affect the result. The ratio between the fluorescence power of the spin-casted beads in the antenna and on the coverslip is nearly 7.2 for NA=0.6. This is due to the ring shape emission of a single bead on the coverslip with nearly 85° angle while the maximum collection angle for 0.6 NA objective is 72°. On the other hand, in the antenna due to the high directionality of emission (40-45°), most of the light is collected with the 0.6 NA objective.

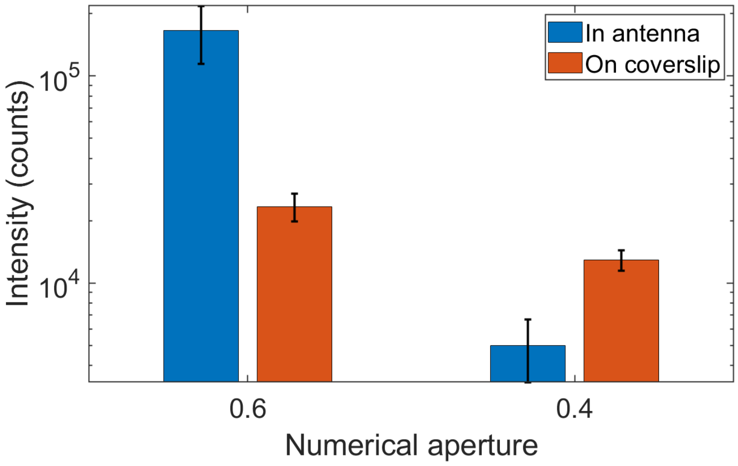

Figure 4.13: ***Collection efficiency with different collection angle angle.***

Furthermore, we measure the P_{fluo} with 20x and 0.4 objective. However, due to the larger focal volume ($\sim$90 μm^3) of such an objective, a larger area of the sample is excited and as a result, the background is higher. This cause a weak signal after the background subtraction in the antenna (see Fig. 4.13).

Although it seems the radiation pattern changes do not contribute to the signal increase when we utilize high-NA objectives, it becomes an important factor once we start using low-NA objectives. This can be interpreted from the signal enhancement of a 40 nm fluorescence bead with a 1.4 NA oil objective and 0.6 NA air objective in the antenna as compared to a bead on a coverslip. The signal enhancements are 3 and 7.2 for oil and air objectives, respectively. This difference clearly presents the advantage of the beaming effect in the antenna system.

4.4 Article II: Biosensing with a scanning planar Yagi–Uda antenna

Bibliographic Information

N. Soltani, E. Rabbany Esfahany, S. I Druzhinin, G. Schulte, J. Müller, B. Butz, H. Schönherr, M. Agio, and N. Markešević, ”Biosensing with a scanning planar Yagi–Uda antenna,” Biomed. Opt. Exp. 13, 539-548 (2022).

Author’s contribution

The author contributed to sample preparation, experiment and data analysis, drafting of the manuscript, and revisions.

Copyright Notice

Abstract

We investigate a model bioassay in a liquid environment using a z-scanning planar Yagi–Uda antenna, focusing on the fluorescence collection enhancement of ATTO-647N dye conjugated to DNA (deoxyribonucleic acid) molecules. The antenna changes the excitation and decay rates and, more importantly, the emission pattern of ATTO-647N, resulting in a narrow emission angle (41°) and improved collection efficiency. We efficiently detect immobilized fluorescently-labeled DNA molecules, originating from solutions with DNA concentrations down to 1 nM. In practice, this corresponds to an ensemble of fewer than 10 ATTO-647N labeled DNA molecules in the focal area. Even though we use only one type of biomolecule and one immobilization technique to establish the procedure, our method is versatile and applicable to any immobilized, dye-labeled biomolecule in a transparent solid, air, or liquid environment.

Introduction

The detection of biomolecules at low concentrations [111, 112] is crucial for the early-stage diagnostics of diseases. However, their interrogation is a real challenge since they are small and typically mixed with other types of molecules. They are detectable upon interaction with light or via other schemes; thus, various labeling and label-free techniques have been developed over the years [113–116].

To enhance the collection efficiency and improve the signal-to-noise ratio (SNR), different phenomena and techniques such as surface plasmon resonance [117], localized surface plasmon resonance [118,119], surface-enhanced Raman spectroscopy [120, 121], optofluidic Fabry-Pérot cavities [122], nanogap antennas [74, 123], and zero-mode waveguides [124] have been employed.

In some cases, it is essential to label the biomolecule with fluorescence dyes. However, these suffer from blinking and photobleaching [125]. Moreover, they emit light-like dipolar sources. This further means that a significant fraction of the emitted photons cannot be efficiently collected by optical elements. A practical approach to overcome this issue relies on optical antennas that can change the radiation pattern, enhance the excitation efficiency and the fluorescence quantum yield to improve the emission signal [21, 77, 80, 81].

Most optical antennas demand precise positioning of the emitters and complicated fabrication and experimental procedures to observe a significant change in the radiation pattern. A planar optical Yagi–Uda antenna, which enhances the collection efficiency by beaming the fluorescent light into a narrow cone, has been recently proposed [22]. This system is easy to fabricate, and it does not suffer from a demanding positioning with nanometer-scale precision. Namely, it is only essential to immobilize emitters on a transparent substrate supported by a thin metal layer; otherwise, the translation in the (xy) plane does not play a crucial role. We further extended this idea to a z-scanning planar Yagi–Uda antenna, where we can control the vertical distance between the antenna elements to examine the optical properties of fluorescent beads [126].

In this work, we apply the scanning antenna approach for biosensing to detect short double-stranded DNA (dsDNA) molecules in a liquid, immobilized on a transparent surface. Although dsDNA molecules are not fluorescent, one of the strands in the pair features a single dye molecule, ATTO-647N (ATTO-TEC GmbH), which enables its detection. ATTO-647N is chosen because it is rather photo-stable and possesses a high fluorescence quantum yield. Despite the fact that we utilize ATTO-647N labeled dsDNA molecules as a toy model, we argue that this approach is general and that it can be applied to specific fluorescence-based bioassays.

Materials and Methods

DNA strands and hybridization

Short dsDNA molecules are created in a hybridization process of the sequences purchased from Integrated DNA Technologies (DNA1: 5'-/5Biosg/ GCA CGA AAC CTG GAC ATG GGA ACA ATA -3' and DNA2: 5'-/5ATTO647NN/TAT TGT TCC CAT CTG GTC CAG GTT TCG TGC -3'). The sequences are modified and adjusted from Ref. [127]. In this process, 1 μL of 100 μM of DNA1 and 1 μL of 100 μM of DNA2 are mixed with 7 μL of pure water (MilliQ H_2O 18.2 MΩcm) and 1 μL of 1 mM NaCl in a micro-tube and left in a hot water bath (95 °C) to cool overnight. The described procedure ensures that the dsDNA constructs feature a single ATTO-647N fluorophore on one end and a biotin molecule on another.

Flow channels

A glass coverslip (PLANO, L42342 #1) is first rinsed with pure water and isopropanol and subsequently dried with compressed air. After the rinsing and drying steps, 15 minutes of UV-ozone cleaning (Bioforce UV/Ozone ProCleaner Plus) increase the hydrophilic character of the glass surface and promotes the attachment of proteins. A flow channel is eventually created on the glass coverslip, by placing two stripes of parafilm at a distance of approximately 5 mm and by gluing them to the surface by heating the glass coverslip on a hot plate above 60 °C. The flow channel prevents the solution to spread over the sample, and it provides a controllable

ATTO-647N labeled dsDNA immobilization process, which will be explained in the next step.

dsDNA attachment to the surface

The attachment of the ATTO-647N labeled dsDNA molecules in the flow channel consists of several steps [128, 129], which we follow in the sample preparation process. Biotinylated bovine serum albumin (BSA) and neutravidin are purchased from Sigma-Aldrich (cat. no A-8549) and Thermo Scientific (31000), respectively, and dissolved in water to the concentration of 1 mg/mL, each. After pipetting 40 μL of BSA solution into the flow channel and the incubation time of 10 minutes, the surplus of material is washed by 400 μL (4 × 100 μL) of T50 (10 mM Tris and 50 mM NaCl). In the following steps, we add the same volumes of neutravidin and superblock (Thermo Scientific 37515), one after the other, with the same incubation time and washing procedures in between. The superblock prevents any non-specific binding.

Finally, 40 μL of a solution of ATTO-647N labeled dsDNA in T50 is added and left to incubate for 30 minutes leaving ample time for the attachment. The washing step at this point is particularly important to remove all free-floating fluorescent molecules, which could cause an unwanted background signal during the optical measurements. We prepare several different samples with different concentrations of ATTO-647N labeled dsDNA in T50 ranging from 10 nM down to 10 pM.

Fabrication of a planar Yagi–Uda antenna

A planar Yagi–Uda antenna consists of two main parts, a reflector, and a director [22]. We purchase glass substrates coated with 2 nm titanium and 10 nm gold (Platypustech, AU.0100.CSS Square Coverslips). The titanium layer is an adhesion layer, while the gold film plays the role of a director. The auto-fluorescence of the gold film increases the background signal in the optical measurements (see Fig. 4.18) but it does not prevent an efficient detection of ATTO-647N.

The fluorescent molecules should be positioned at a distance in the range between $\lambda/6n$ and $\lambda/4n$ from the antenna elements in order to have the maximum beaming effect. Here, n represents the refractive index of the medium and λ is the emission wavelength in free space [22]. Therefore, an E-beam evaporation of a 75 nm thick SiO_2 layer over the gold film turns out as the most convenient method to form a transparent spacer, which in addition does not induce quenching.

The coverslip coated with 10 nm gold and 75 nm SiO_2 layers will be called the director substrate in the rest of the text. The standard procedure of the dsDNA attachment described for glass coverslips works well also for SiO_2 and in this case, the flow channel is formed on the director substrate, following the procedure described earlier (director flow channel).

The reflector is created starting from a 250 μm diameter gold wire (chemPUR, NO:009164), which is electrochemically etched (37% HCl) and then milled by Focused Ion Beam (FEI Helios Nanolab 600). This is the way to manufacture a flat mirror (10 μm diameter), which plays the role of a reflector.

The antenna elements are adjusted to be parallel to each other and the distance between the reflector and the substrate director can be varied by a piezo stage (Newport, NPM140SG). To fix the tilt angle and find a contact point, we observe the interference pattern caused by the phase shift between the reflected light from the director and the reflector using a CMOS camera (ZEISS AxioCam ERc 5s Rev.2) [126,130].

Optical setup and measurements

We detect ATTO-647N labeled dsDNA molecules with an epifluorescence microscope (Zeiss, Axio Observer 3) equipped with an oil-immersion objective (Zeiss, Plan-Apochromat 63x/1.4). To verify the success of the immobilization process, we use a wide-field imaging technique by adding a lens (WFL) before the objective into the excitation path. For the excitation, we utilize a pulsed diode laser at the wavelength of 636 nm (Picoquant, LDH-P-C-640B) with a repetition rate of 40 MHz. The collected light from the sample is sent through a set of filters; a long-pass (LP) (cutoff at 650 nm) and a band-pass (BP) (660-700 nm) filter to remove the reflected laser light and reduce the background.

A homemade module holding the gold wire is mounted on top of the microscope, which enables precise control over the distance between the reflector and the director using a piezo stage, as mentioned earlier. The center of the reflector is positioned directly above the focal spot of the laser, and it can move step-wise in the z direction. A motorized stage (ASI, PZ-2000FT) controls the position of the director substrate (with ATTO-647N labeled dsDNA molecules immobilized on the surface) in the xy directions.

At each piezo step, the emitted light is collected by the same objective and sent further either to single-photon avalanche diodes (SPADs) (Excelitas, SPCM-AQRH-TR) or to a CMOS camera (Andor, Zyla 4.2 Plus), depending on the type of experiment. For lifetime and intensity measurements, we direct light toward the SPADs, which are connected to a Time-Correlated Single-Photon Counting (TC-SPC) device (PicoQuant, Pico Harp 300). To determine the radiation pattern of the molecules, light is sent to the CMOS camera with the back focal lens in front of it. It is also possible to replace the CMOS camera with a spectrometer (OceanOptics

QE Pro) in order to check the emission spectrum of the molecule or the fluorescence background.

Results

After the immobilization of ATTO-647N labeled dsDNA molecules on the glass coverslip flow channel, we use wide-field imaging to estimate the distribution and the number of attached molecules (Figure 4.14(a)-(f)). The attachment process is random, therefore we can clearly observe the regions with different densities of emitters. This becomes prominent once the DNA concentration in the incubated solution drops below 1 nM. The set of measurements is performed to understand the relation between the concentration of ATTO-647N labeled dsDNA molecules in solution and the number of molecules that are eventually attached to the substrate. To determine the fluorescence background, we functionalize a glass surface with BSA, neutravidin, and superblock, with washing steps in between, as described before, and perform wide-field imaging (Fig. 4.14(f)). It is clear that the functionalization of the glass surface does not significantly contribute to the background signal.

The distribution of ATTO-647N labeled dsDNA molecules on coverslips and on a thin layer of SiO_2 is the same. Therefore, we expect to obtain the same molecular distribution on the director substrate as in the case of a glass coverslip flow channel. Figure 4.14(g) shows the scheme of a director flow channel and Fig. 4.14(h)-(i) represents the wide field image of samples prepared with DNA concentrations of 10 nM and 1 nM in water on the director flow channel. As shown in Fig. 4.14(j), the background of the gold substrate is high and 70% of the excitation light is reflected by the 10 nm gold layer. Therefore, it is difficult to observe the molecular distribution for samples prepared with DNA concentrations in water below 1 nM.

The collected fluorescence power (P_{fluo}) of an emitter in the planar antenna configuration is influenced by the fluorescence radiation pattern, the excitation power (P_{exc}), and the excited-state decay rate (Γ) [126]. Here, we simply probe these parameters for ATTO-647N in T50 by changing the reflector-director substrate distance. Since the back focal plane (BFP) imaging and decay rate measurements benefit from a higher number of detected photons, we choose samples prepared with DNA solutions at a concentration of 10 nM in water.

In Fig. 4.15(a) a scheme of the BFP imaging experimental setup is presented. The reflector is retracted step-wise from the relative zero position in the z-direction. Since ATTO-647N dye is prone to bleaching (see Fig. 4.19 of the Supplementary Material), our approach is to decrease the measurement time as much as possible. This can be done either by step-size increasing or by decreasing the photon collection times. However, to construct BFP images using a CMOS camera, we cannot further

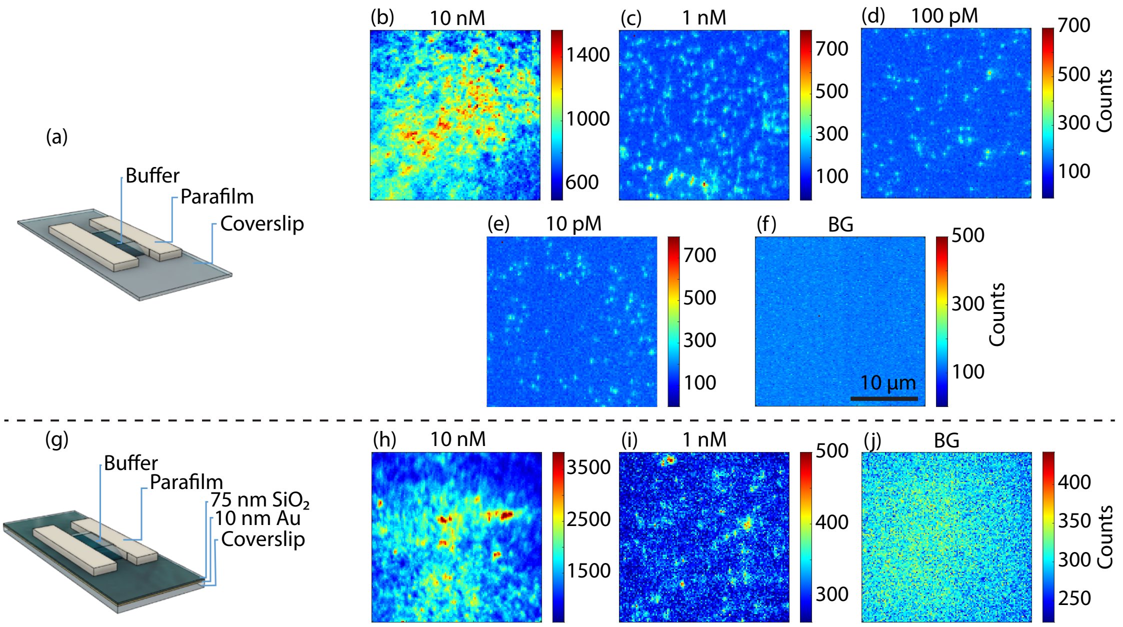

Figure 4.14: ***Wide-field image of immobilized ATTO-647N labeled dsDNA.*** *(a) Scheme of a glass coverslip flow channel. The channel is created between parafilm stripes to ease the washing process. (b-e) Data for samples prepared with different concentrations of ATTO-647N labeled dsDNA molecules (from 10 nM to 10 pM) in water on a glass coverslip flow channel. (f) Wide field image of T50, BSA, neutravidin, and superblock (background) as a reference. The excitation power before the entrance of the microscope for (b-f) is 250 μW. (g) Scheme of a flow channel on the director substrate (director flow channel). (h-i) Wide-field images of samples prepared with buffers at a DNA concentration of 10 nM and 1 nM on the director substrate. For samples prepared with concentrations below 1 nM, the molecules are hardly distinguishable from the background (not shown). (j) Background fluorescence image of the director substrate as a reference (before immobilization of ATTO-647N labeled dsDNA molecules). The excitation power before the entrance of the microscope for (h-j) is 827 μW. In all images the excitation wavelength is 636 nm and the integration time of the CMOS camera is 1 s. The scale bar for all figures is given in (f). The dark counts of the camera are around 100 and they are not subtracted.*

decrease the acquisition time. Thus, a 20 nm step size with an integration time of 2.2 s for each step seems like an appropriate solution.

The collected light from the sample is sent through the filter set and detected by the CMOS camera or the SPAD. The radiation pattern of the emitters is recorded by the CMOS camera. On the other hand, using TCSPC we construct a decay histogram. The integration of this histogram determines the total emitted power (P_{tot}), which comprises the fluorescence signal of the ATTO-647N dyes (P_{fluo}) and the background (P_{bg}). By deconvolving the decay histogram, using the instrument response function (IRF), one can plot the P_{fluo} and Γ as a function of the distance between the director substrate and the reflector, as shown in Fig. 4.15(b). In this experiment, the P_{bg} is much smaller than P_{fluo}, which gives us an SNR of 8.5 in the

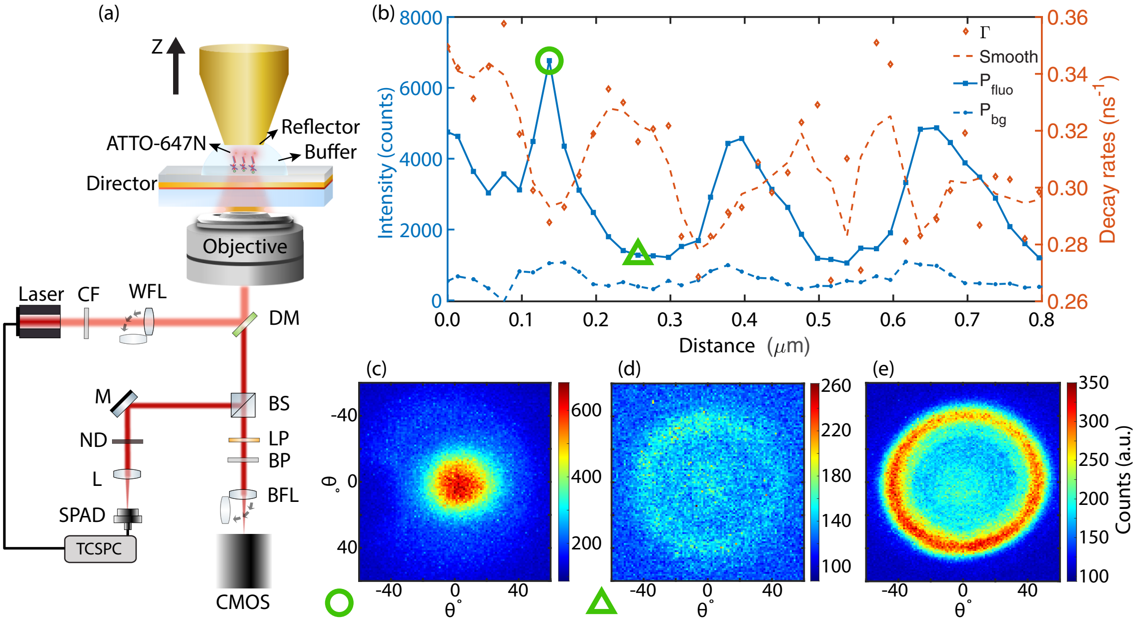

Figure 4.15: ***ATTO-647N labeled dsDNA in the scanning planar antenna with liquid medium.*** *(a) Schematic diagram of the scanning Yagi–Uda antenna configuration and the optical setup. The medium between the reflector and the director substrate is the T50 buffer. The sample was prepared from a solution of dsDNA molecules at a concentration of 10 nM in water. 95% of P_{tot} is detected by the CMOS camera and 5% is recorded by the SPAD. CF is a clean-up filter, M is a mirror, L is a lens and WFL is a wide-field lens. (b) P_{fluo}, P_{bg} (counts), and the decay rate (ns^{-1}) as a function of the distance between the reflector and director substrate. The red dashed line is obtained by averaging three neighboring values of the decay rate. (c-d) The radiation pattern for two selected positions is marked by a circle and a triangle in (b). (e) BFP image of ATTO-647N labeled dsDNA molecules immobilized in the coverslip flow channel.*

maximum of P_{fluo}. The peak-to-peak distance of P_{fluo} is 259 nm and it corresponds to $\lambda/2n$, where n is the refractive index of T50 (close to water) and λ is the emission wavelength of ATTO-647N (~680 nm).

Although P_{fluo} is not a smooth curve in Fig. 4.15(b), it is easy to observe that the intensity oscillates with the reflector-director substrate distance, as shown in Ref. [126], where the decay rate of fluorescence beads changes periodically in a scanning Yagi–Uda antenna. Here, however, the decay rate is not periodic after the first intensity peak, most likely due to scanning with larger steps and data points fitting (see Fig. S3 in the Supplementary Material).

Additionally, in Fig. 4.15(c)-(d), we represent the BFP image of the emitted light at different selected distances marked by a circle and a triangle in Fig. 4.15(b). Figure 4.15(e) shows instead the emission pattern of ATTO-647N labeled dsDNA molecules on a glass coverslip (without a director nor reflector), which can be considered as the reference radiation pattern. Comparing Fig. 4.15(c) with Fig. 4.15(e), we notice that the radiation pattern changes from a ring shape to a ”Gaussian-like” shape, with a full-width at half maximum (FWHM) of 41° at the emission maximum. This beaming effect can have advantages in biosensing because it can improve the collection efficiency and it allows us to reduce the numerical aperture of the optics (objective or fiber) without losing the signal.

Figure 4.15 shows the fluorescence signal, the beaming effect, and the modification of the decay rate for ATTO-647N dyes attached to dsDNA molecules, immobilized in the antenna at a concentration of 10 nM in water, with the space between reflector and director substrate filled with T50. For samples prepared to start from lower DNA concentrations in water, the number of molecules in the focal area is small. Thus the bleaching time of ATTO 647N plays an important role in longer measurements, and the bleaching of one ATTO-647N dye significantly changes the signal in a step-wise manner (see Fig. 4.19(b)-(d) of the Supplementary Material).

For this reason, we modify the setup and manage to decrease the experiment time by a factor of 4. Moreover, to mitigate the bleaching process, our samples are excited using 2 μW laser power. The total fluorescence power P_{tot} is detected with SPAD1 and the laser reflection from the antenna P_{refl}, attenuated by a neutral density (ND) filter (OD=2), is recorded by SPAD2; a 95:5 beamsplitter is used to split the collected light into these two channels (Fig. 4.16(a)). Thus, we are able to determine the relationship between P_{refl} and the P_{tot} in order to compare the excitation power in different experiments.

Figure 4.16(b)-(c) plots P_{tot} and P_{refl} as a function of the distance between the reflector and director substrate. Since P_{tot} consists of P_{fluo} and P_{bg}, to subtract P_{bg}, we measure the sample in the scanning antenna configuration before (Fig. 4.16(b)) and after (Fig. 4.16(c)) the immobilization of ATTO-647N labeled dsDNA from buffered solution at a concentration of 1 nM.

In Fig. 4.16(b)-(c) the grey area shows the region, where the reflector and director substrate are in contact. The vertical dashed line goes through the maximum of the curve representing P_{tot} (blue curve) and the corresponding point of P_{refl} (red curve) determining the reflection value at a given distance.

In both Fig. 4.16(b) and Fig. 4.16(c) the oscillation amplitude of P_{refl} gradually decreases with the distance between the reflector and director substrate. This phenomenon can be explained by the fact that, while the laser light remains focused on the director, the reflector is not able to refocus the incident laser light. P_{refl} exhibits the resonance of a cavity mode, and the distance between two consecutive dips is $\lambda/2n$. Based on this relation and the fact that we can precisely control this distance using a piezo stage, it is possible to determine the refractive index n of the embedding medium. Here, n is 1.31, which is close to the refractive index of water ($n_{water} = 1.33$), as expected.

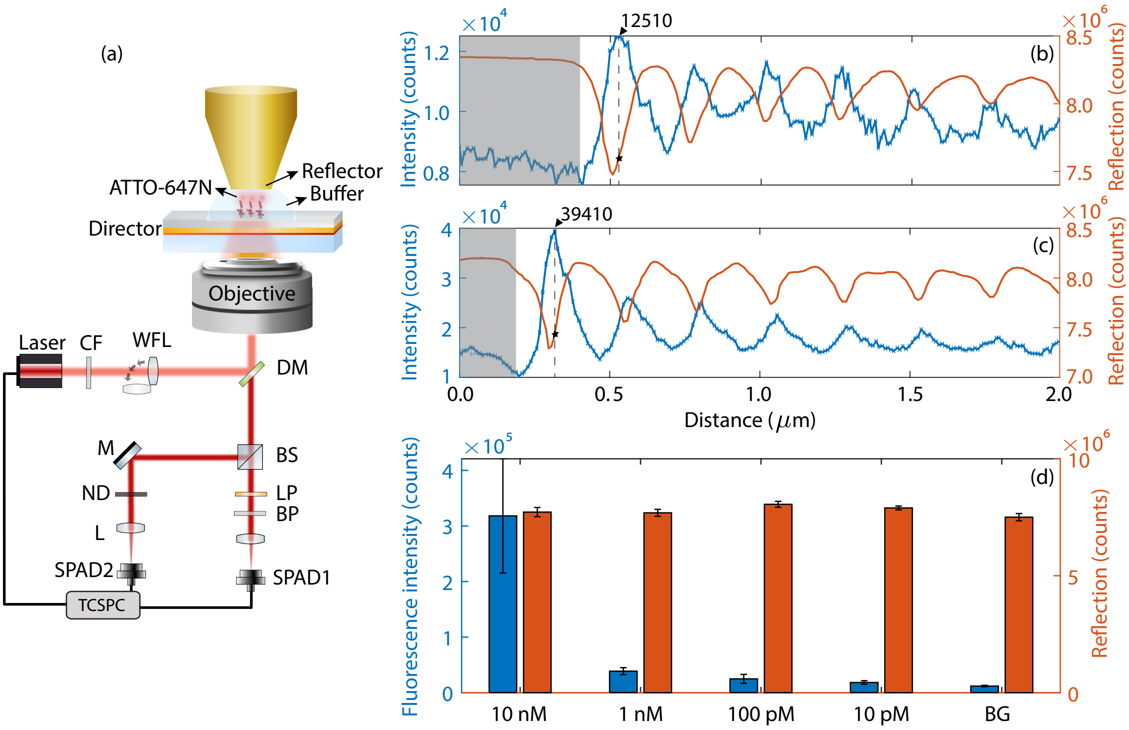

Figure 4.16: ***Fluorescence intensity of ATTO-647N labeled dsDNA molecules immobilized in the planar antenna.*** *(a) Scheme of the experiment. SPAD1 (SPAD2) detects P_{tot} (P_{refl}). (b,c) P_{tot} (blue curve) and P_{refl} (red curve) as a function of the distance between reflector and director substrate (b) without ATTO-647N labeled dsDNA molecules and (c) with ATTO-647N labeled dsDNA molecules at a concentration of 1 nM. The maximum of P_{tot} in (b) is assumed as our background (BG). The grey region is the estimated area, in which the reflector and director substrate are in contact. This experiment takes around 55 s, (d) the Average value of the maximum of P_{tot} and the corresponding P_{refl} for samples with different DNA concentrations. Each sample is measured with 2 μW excitation power.*

Moreover, since the antenna has a higher impact at sub-wavelength distances ($\lambda/6n$ to $\lambda/4n$), the first maximum of P_{tot} is 2.1 times higher than the second one (see Fig. 4.16(c)). On the other hand, the first reflection minimum is 1.5 times deeper than the second one.

We repeat this experiment for different spots of each sample prepared with buffers of various ATTO-647N labeled dsDNA concentrations (1 nM, 100 pM, 10 pM) and for the sample without such labeled dsDNA molecules. Figure 4.16(d) represents the averaged maximum of P_{tot} (blue bins) for samples with different molecule concentrations and the corresponding average of P_{refl} (red bins) at the position, where P_{tot} is maximal (see the cross-section of the black dashed line and red curve in Fig. 4.16(b)-(c)).

In the samples where the initial concentration of ATTO-647N labeled dsDNA molecules is very low (100 pM and 10 pM), the molecules attached to the surface are spatially well separated, and the distance between them can be several micrometers in some cases. Therefore, if we choose measurement points randomly, most of the time, we would collect only a background signal. To avoid this, at low concentrations we first try to find bright spots (fluorescent emitters) using wide-field imaging, and only then do we position the bright spots onto the focal point of the excitation beam. The downside of this approach is that most likely, we select points with several emitters in the diffraction-limited spots since they are more visible in wide-field imaging.

Therefore, we can associate the detected signal to a concentration with certainty, by our apparatus and sensing approach (i.e., by randomly choosing spots), only for samples prepared from solutions with a concentration of at least 1 nM, which corresponds to few (below 10) molecules in the detection spot. To better quantify the fluorescence signal, we would need to measure the mean concentration of molecules, for example, by knowing the illuminated area and the photon counts of a single molecule.

Figure 4.17(a) shows the same quantities of Fig. 4.16(d) for samples prepared with the coverslip flow channel. The significantly higher reflection signal in the antenna (Fig. 4.16(d)) compared to the coverslip is due to the high reflectivity ($\approx$ 70%) of the director. By subtracting the background from the fluorescence signal for each concentration in Fig. 4.16(d) and Fig. 4.17(a), one can calculate the fluorescence signal of the ATTO-647N dyes (P_{fluo}). In figure 4.17(b), P_{fluo} in the coverslip flow channel is compared with P_{fluo} in the antenna configuration for different ATTO-647N labeled dsDNA concentrations excited at 2 μW. We repeat the same experiment for the laser excitation power of 6.6 μW and the results are similar as in the case of 2 μW (not shown).

Figure 4.17(b) determines that for samples prepared with higher DNA concentrations (10 nM and 1 nM) in the antenna, the signal improves by a factor of 2, which is consistent with our previous work [126]. Here, such signal enhancement is caused mainly due to the modulation of the excitation rate. The beaming effect provides a minor change in the signal due to collection with a high NA objective. If the NA becomes smaller, the beaming effect plays a significant role as the collection efficiency remains nearly the same for molecules in the planar antenna, whereas it drastically reduces for molecules on the coverslip. This increases further the antenna signal enhancement. On the other hand, since the results for samples prepared with DNA concentrations below 1 nM are obtained by pre-selection of the measurement points, it is difficult to compare them with the corresponding reference samples. To overcome this issue, a solution would be to perform a raster scan on the surface to increase the probability of excitation/detection of the fluorescent molecules.

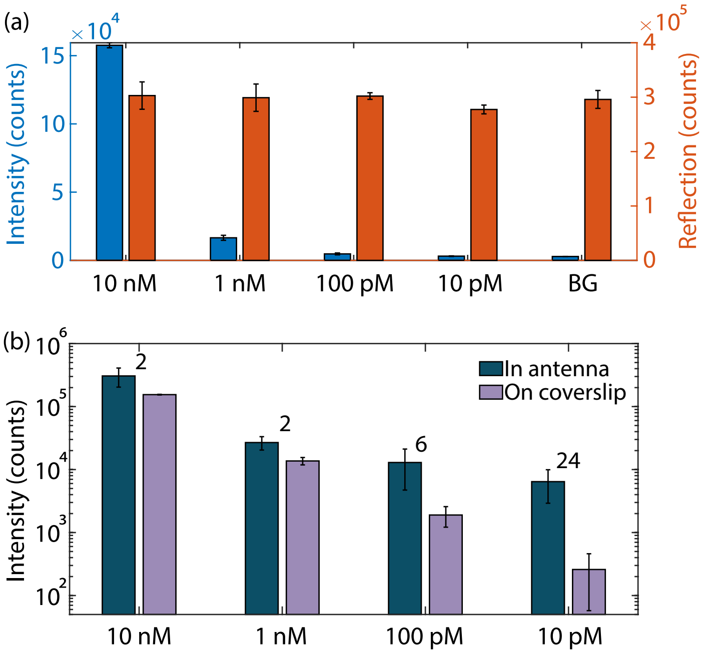

Figure 4.17: ***Fluorescence of ATTO-647N labeled dsDNA molecules in the antenna and on the coverslip.*** *(a) Average value of the maximum of P_{tot} and the corresponding P_{refl} for samples with different DNA concentrations on a glass coverslip. Each sample is measured with 2 μW excitation power. (b) The average background-corrected fluorescence signal of samples with different DNA concentrations on a coverslip and in the antenna. The numbers above each bin represent the signal enhancement ratio.*

Conclusion

In this work, we show that the fluorescence signal, the radiation pattern, and the decay rate of ATTO-647N dyes labeling dsDNA molecules immobilized in the antenna can be controlled by changing the distance between the reflector and the director. Specifically, the radiation pattern changes from a doughnut shape to a Gaussian-like profile (FWHM of 41°), and the fluorescence signal can be enhanced. This demonstrates the possibility of using low-NA optics since by reducing the numerical aperture, the collected fluorescence is not decreased. Therefore, this approach does not demand the use of microscopes [131] and it is also suitable for fiber-based detection [87, 132].

These findings motivate us to use this approach for biosensing in, e.g., in-vitro diagnostics. We show that ATTO-647N labeled dsDNA molecules in the antenna have at least a two-fold signal enhancement as compared to on a glass coverslip for the same analyte concentration in the buffer. Although one can detect single molecules with a planar antenna [22], our biosensor configuration is suitable for samples prepared from solutions with analyte concentrations down to 1 nM, which corresponds to few (below 10) molecules in the focal spot. For samples obtained from lower concentrations, one should use for instance, raster scanning techniques in a small region (roughly 10 μm × 10 μm) of the sample in order to obtain a signal proportional to the target molecule concentration. Finally, we argue that this technique can work for any fluorescence-based immobilized bioassay that fits the space between the reflector and director while keeping the distance constraints.

Supplementary information for: Biosensing with a scanning planar Yagi–Udaantenna

Fluorescence background of the gold director

Figure 4.18(a) shows the surface roughness of a 10 nm gold film (Platypustech, AU.0100.CSS Square Coverslips) captured by an environmental scanning electron microscope (ESEM). The emission intensity and the spectra of the light collected from the gold-coated glass coverslip as a function of laser power is presented in Fig. 4.18(b) and (c), respectively. The gold film auto-fluorescence originates from an electronic interband transition between the $s-p$ conduction band and the d bands [133]. In thin films, the surface roughness can cause additional resonances due to localized surface plasmon modes [94]. In our experiments, the gold director generates around 2-3 times higher background auto-fluorescence than the signal detected from the glass coverslip.

Bleaching time of ATTO-647N in T50 buffer

ATTO-647N (ATTO-TEC GmbH) dyes are subject to bleaching and, for a large ensemble of emitters, the intensity curve decays exponentially as presented in Fig. 4.19(a) (52 s for an ensemble of emitters). However, the number of molecules in the focal area is small for samples with lower concentrations. In this case, bleaching and blinking of individual molecules significantly change the fluorescence signal and play an essential role in single-molecule detection. The results are shown for ATTO-647N labeled dsDNA molecules immobilized on coverslip [128, 129] flow channels from buffered solutions with concentrations of 1 nM, 100 pM, and 10 pM in Fig. 4.19(b)-(d), respectively. We use 2 μW laser power in this set of measurements, except for samples prepared at a concentration of 100 pM (Fig. 4.19(c)), in which the excitation power is 6.6 μW. In this way, we demonstrate that the emitters do not bleach immediately, even at higher excitation powers.

In Fig. 4.19(b)-(d), the emission intensity changes in a step-wise manner as molecules blink and bleach randomly. The step sizes and the initial intensity can be used to estimate the number of molecules in the focal spot. Therefore, we conclude that at low concentrations, the bright spots typically contain less than ten emitters. Likewise, we expect a similar behavior for ATTO-647N labeled dsDNA molecules immobilized on the gold director in the antenna configuration.

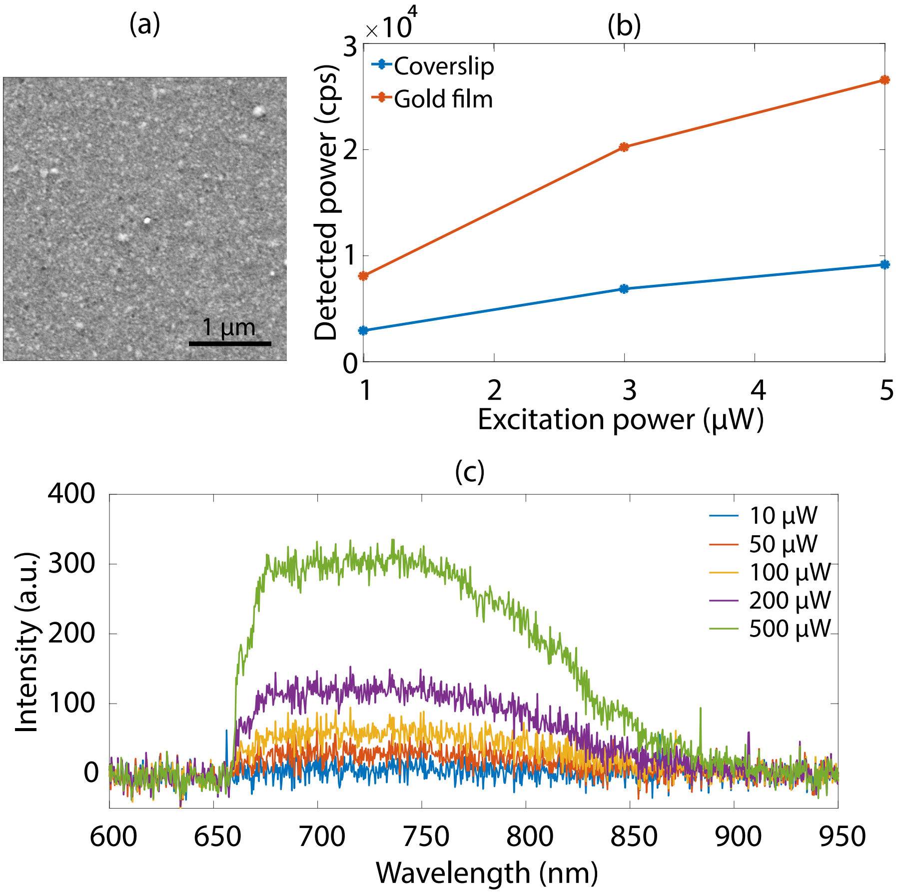

Figure 4.18: ***Characterization of the gold director.*** *(a) Environmental scanning electron microscope (ESEM) image of a 10 nm gold film (director) formed on a glass coverslip. (b) Detected power by a single-photon avalanche detector (SPAD) for low excitation powers (range used in the experiments). (c) Fluorescence spectrum of the gold director as a function of the excitation power using a long-pass filter (cutoff at 650 nm).*

Signal deconvolution and decay rates fitting

As an example, the fluorescence decay of ATTO-647N molecules at the first maximum and minimum fluorescence intensity in Fig. 4.15(b) of the manuscript (circle and triangle positions) are shown in Fig. 4.20. The deconvolution process and fitting method are explained in the supporting information of Ref. [126]. At the circle position (Fig. 4.20(a)), due to higher signal counts, the decay fitting exhibits a lower error as compared to the triangle position (Fig. 4.20(b)).

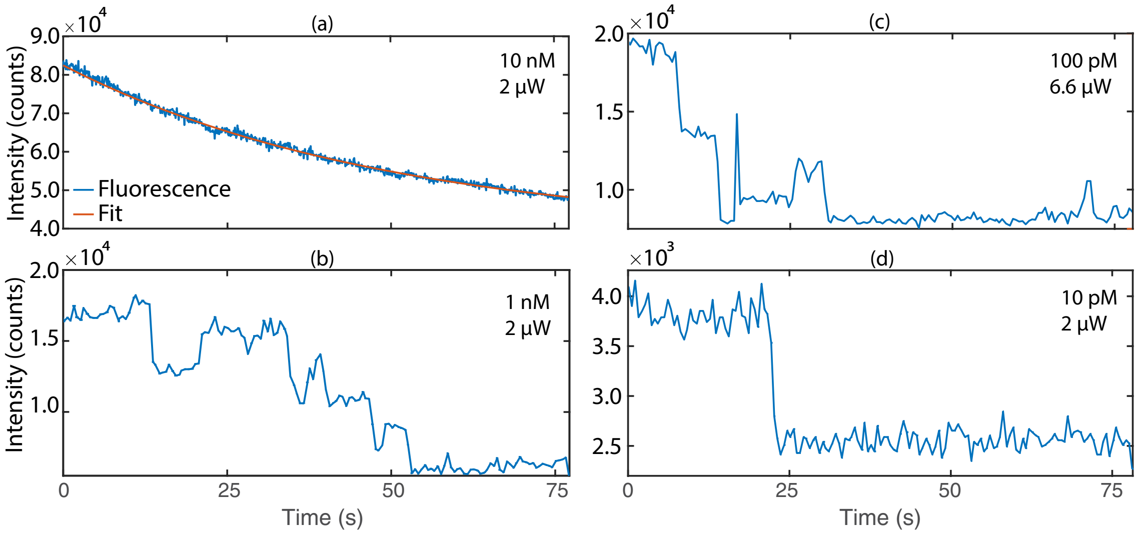

Figure 4.19: ***ATTO-647N bleaching and blinking in T50 buffer.*** *(a) Bleaching of ATTO-647N labeled dsDNA immobilized on a coverslip from a 10 nM solution. The experimental data fitted with a first-order exponential function (red curve) to find the bleaching time, which is approximately 52 s. (b-d) Step-wise bleaching and blinking of ATTO-647N labeled dsDNA from buffers with different concentrations immobilized on a coverslip: (b) 1 nM and 2 μW excitation power, (c) 100 pM and 6.6 μW excitation power, and (d) 10 pM and 2 μW excitation power.*

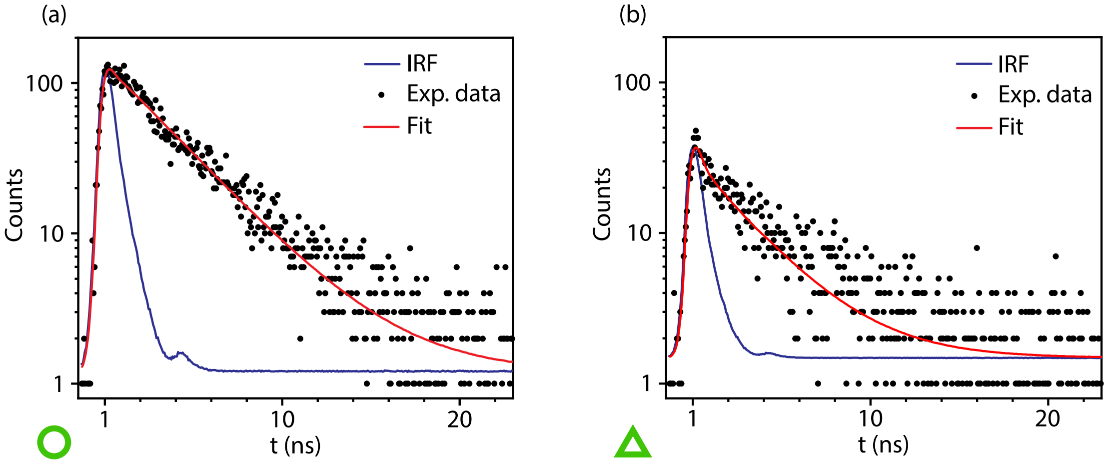

Figure 4.20: ***Fluorescence decay of ATTO-647N labeled dsDNA molecules in the planar antenna.*** *(a) Fluorescence decay at the first maximum of the fluorescence intensity shown in Fig. 4.15(b) (circle). SiO$_2$-reflector distance 137 nm, decay rate $\Gamma = 0.29$ ns^{-1}, fluorescence intensity P_{fluo} = 6767 counts and background intensity (scattering of excitation light) P_{bg} = 1050 counts. (b) Decay at the first minimum of the fluorescence intensity is shown in Fig. 4.15(b) (triangle). SiO$_2$-reflector distance 256 nm, decay rate $\Gamma = 0.32$ ns^{-1}, fluorescence intensity P_{fluo} = 1277 counts and background intensity P_{bg} = 394 counts.*

Chapter 5

Fiber-based planar Yagi–Uda antenna

The collection of fluorescence or scattered light from a nanoscale source using optical fiber is a desirable method due to the flexibility and efficient light transfer capabilities of fibers. However, this collection process can suffer from inefficiencies caused by factors such as the small size of the fiber core, low numerical aperture (NA) of the fibers, and challenges associated with alignment.

In this chapter, we investigate the coupling efficiency of light with different sources into an optical fiber. For this reason, first, we calculate the coupling efficiency of a plane field focused on a fiber with an ideal lens. Afterward, we show the diffraction of the focused Gaussian beam by an ideal lens considering an arbitrary lens filling factor. In addition, we investigate the coupling efficiency of the emission from a single molecule, treated as an arbitrarily emitted source, into a fiber using the planar Yagi–Uda configuration. Our findings demonstrate that the emitted or scattered light can be effectively coupled into the optical fiber without the need for optical lenses, thanks to the beaming effect provided by the planar antenna. We also provide guidelines for the fabrication of optical fibers that exhibit a large collection efficiency in the planar antenna configuration by changing optical fiber parameters, such as the refractive indices of core and cladding. Ultimately, we focus on the experimental challenges of using an optical fiber and etching technique to provide a small fiber tip.

5.1 Efficient light coupling to a fiber

The efficient coupling of light into an optical fiber depends on several physical and technical parameters. In theory, the coupling of light into an optical fiber can be classified based on the characteristics of the fiber and the wavelength of the light into two categories. First, coupling into multimode fibers, where one can use the ray optics to calculate the coupling, and second, coupling into single-mode fibers, in which one must consider the problem of mode matching of the incident light and the mode of the fiber. The latter cannot be solved by ray optics and should be calculated using the concepts of Gaussian beam optics.

To couple a collimated light beam into a multimode fiber, the light should focus into a spot that is smaller than the core diameter of the fiber using a collimator, and the angle from the collimator to the fiber (θ_f) should be smaller than the acceptance angle of the fiber, which is equal to $\arcsin(NA/n)$. However, any collimated light has a divergence (θ_i), which also has to be considered in the coupling. As it is shown in Fig. 5.1 the diameter of the focal spot is equal to $y_f = 2\,\theta_i \cdot f$, where f is the focal length of the lens. Moreover, the angle θ_f is equal to $\theta_f = y_i/2\,f$, where y_i is the beam waist.

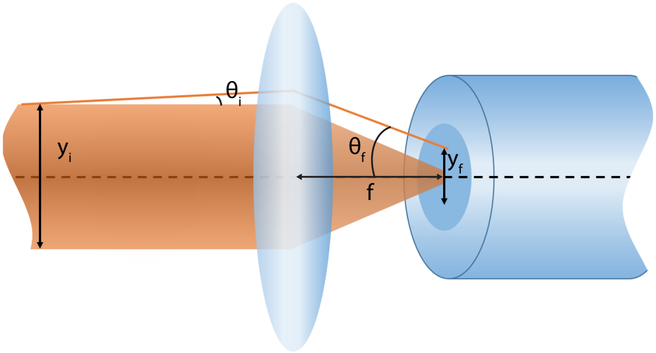

Figure 5.1: ***Diagram of a collimated light couple into an optical fiber.*** *The collimated light has a beam waist of y_i and divergence of θ_i angle. The light is focused on the core of a fiber and has a focal diameter of y_f.*

This is a fundamental limitation on the size of the focused spot in this application with an aberration-free lens. The only way to provide the spot size smaller is to use a lens of shorter focal length or expand the beam. In addition, diffraction may limit the spot to an even larger size, but since normally the core of multimode fibers is large (as compared to the range of working wavelength), we are ignoring wave optics and only considering ray optics.

On the other hand, in single-mode fibers, we can estimate the coupling intensity to a fiber only by integration of the field at the focus over the fundamental mode of the fiber known as overlap integral. Therefore, we investigate the electric field at the focus of a Gaussian beam and the fundamental mode of an optical fiber in the next subsections.

In addition to theoretical limitations, fiber coupling in the experiment faces some technical challenges. The difficulty of alignment due to the mechanical degree of freedom and the small size of the core, the stability of optomechanical components, and the aberration of lenses are a few examples of difficulties, which is not included in the theory.

5.1.1 Focusing of electromagnetic field

Understanding coupling efficiency into fiber requires a theoretical understanding of strongly focused light by an anti-reflected aplanatic lens. Here, we assume that the incident field ($\boldsymbol{E}_{\mathrm{inc}}$) has a planar phase front and is entirely polarized along the x-axis:

$$\boldsymbol{E}_{\mathrm{inc}} = E_{\mathrm{inc}}\, \boldsymbol{n}_{\mathrm{x}}, \tag{5.1}$$

where, E_{inc} is the field amplitude. The optical ray, which intersects on a sphere of radius f converges to the focus of the lens and provides an angle θ with the optical axis as shown in Fig. 5.2. The total refracted electric field (far-field) is equal to [33]:

$$\boldsymbol{E}_{\infty}(\theta,\phi) = E_{\mathrm{inc}}(\theta,\phi)\frac{1}{2}\begin{bmatrix}(1+\cos\theta)-(1-\cos\theta)\cos 2\phi\\ -(1-\cos\theta)\sin 2\phi\\ -2\cos\phi\sin\theta\end{bmatrix}\sqrt{\frac{n_1}{n_2}}. \tag{5.2}$$

By knowing the amplitude profile of the incident beam (E_{inc}), the far-field will be determined. If the incident beam has a Gaussian profile, depending on the mode number E_{inc} can take different values [33]. In this chapter, we only focus on the lowest Hermite-Gaussian mode, which is the fundamental Gaussian beam and is equal to Eq. 5.3 in the spherical coordinate of (f,θ,ϕ).

$$E_{\mathrm{inc}} = E_0 \mathrm{e}^{-f^2\sin^2\theta/\omega^2} \tag{5.3}$$

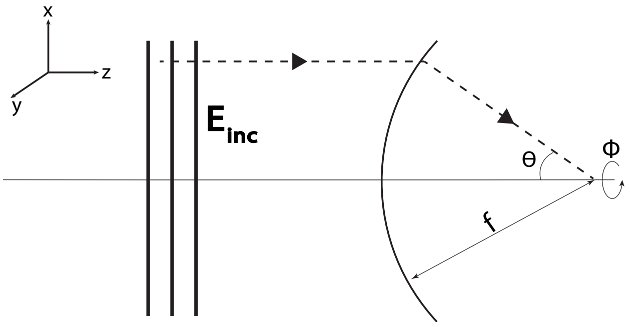

Figure 5.2: ***Geometrical representation of the aplanatic system.*** *The refraction of light rays at an aplanatic lens is determined by a spherical surface with radius f.*

Since the aperture radius of our lens is equal to $f\sin\theta_m$, we define the filing factor f_0 as:

$$f_0 = \frac{\omega_0}{f \sin\theta_m}, \tag{5.4}$$

where θ_m is the maximum angle of convergence. By substitution of the filling factor in the exponential term of the Gaussian equation, we derive:

$$f_\omega(\theta) = \mathrm{e}^{-\frac{1}{f_0^2}\frac{\sin^2\theta}{\sin^2\theta_m}}, \tag{5.5}$$

which is known as the apodization function and it can be viewed as a pupil filter. In this section, for simplicity, we only consider the case that the incident beam overfilled the back-aperture of the focusing lens ($f_0 \to \infty$). This limits the apodization function to one, which represents the plane wave ($E_{inc} = E_0$).

Now, we can compute the field $\boldsymbol{E}$ near the focus. For this we substitute Eq. 5.2 into the angular spectrum representation of the focal field, which is in cylindrical coordinates:

$$\boldsymbol{E}(\rho,\varphi,z) = \frac{ikf\mathrm{e}^{-ikf}}{2\pi}\int_0^{\theta_m}\int_0^{2\pi} \boldsymbol{E_\infty}(\theta,\phi)\,\mathrm{e}^{ikz\cos\theta}\,\mathrm{e}^{ik\rho\sin\theta\cos(\phi-\varphi)}\sin\theta\,\mathrm{d}\phi\,\mathrm{d}\theta, \tag{5.6}$$

where ρ is the transverse size of the beam ($\rho = \sqrt{x^2+y^2}$) and φ representing the angle of the plane wave to the z axis, which $x = \rho\cos\varphi$ and $y = \rho\sin\varphi$. The result of this integral leads to:

$$\boldsymbol{E}(\rho,\varphi,z) = \frac{ikf}{2}\sqrt{\frac{n_1}{n_2}}E_0\mathrm{e}^{-ikf}\begin{bmatrix} I_{00} + I_{02}\cos 2\varphi \\ I_{02}\sin 2\varphi \\ -2iI_{01}\cos\varphi \end{bmatrix}, \tag{5.7}$$

where I_{00}, I_{01}, I_{02} are defined as:

$$I_{00} = \int_0^{\theta_m} (\cos\theta)^{1/2}\ \sin\theta(1+\cos\theta)J_0(k\rho\sin\theta)\,\mathrm{e}^{ikz\cos\theta}\,\mathrm{d}\theta, \tag{5.8}$$

$$I_{01} = \int_0^{\theta_m} (\cos\theta)^{1/2}\ \sin^2\theta J_1(k\rho\sin\theta)\,\mathrm{e}^{ikz\cos\theta}\,\mathrm{d}\theta, \tag{5.9}$$

$$I_{02} = \int_0^{\theta_m} (\cos\theta)^{1/2}\ \sin\theta(1-\cos\theta)J_2(k\rho\sin\theta)\,\mathrm{e}^{ikz\cos\theta}\,\mathrm{d}\theta, \tag{5.10}$$

where J_n is the $\mathrm{n_{th}}$-order Bessel function.

Here, the focusing field is calculated for a Gaussian beam, which overfills the lens aperture (plane wave). However, in a realistic case, the collimated laser light has a small beam waist and covers mostly a small area of the lens aperture, which causes a broadening in the focal spot. This phenomenon is explained in detail in Sec. 5.2

5.1.2 Mode analysis of step-index optical fiber

In fiber coupling, if the angular condition for total internal reflection is satisfied, the light will be confined to the core since the core has a higher index of refraction than the cladding. The fiber geometry and composition determine the a discrete set of electromagnetic fields, or fiber modes, which can propagate in the fiber. To understand the number of modes in fiber, one can use a dimensionless parameter known as V-number, which is defined as:

$$V = \frac{2\pi}{\lambda} a \sqrt{n_{\text{core}}^2 - n_{\text{cladd}}^2}, \tag{5.11}$$

where λ is the vacuum wavelength, a is the radius of the fiber core, and n_{core} and n_{cladd} are the refractive indices of the core and cladding, respectively. For V values below ≈ 2.405, a fiber supports only one mode per polarization direction, which is known as single-mode fiber.

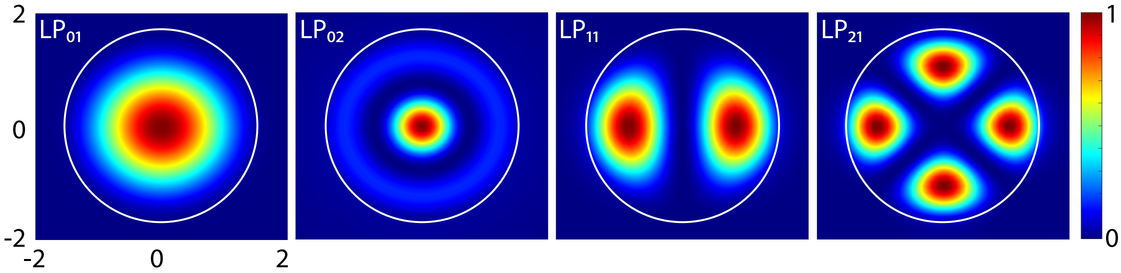

Figure 5.3: ***Linear polarized modes (LP$_{lm}$) in an optical fiber.*** *Fiber with $n_{\text{core}} = 1.4949$, $n_{\text{cladd}} = 1.4533$, $a_{\text{core}} =$ 1.6 μm, has only four modes (LP$_{01}$, LP$_{02}$, LP$_{11}$, and LP$_{21}$) at $\lambda_0 = 700$ nm. The white circle represents the core size.*

To calculate the linearly polarized (LP) mode of the fiber, we assume that the fiber has a cylindrical shape and its transverse refractive index profile is radially symmetric. Since the refractive index contrast of the core and the cladding for the conventional fibers is small, we also consider the weak guidance approximation in this calculation. Here, each of the components of the electric and magnetic fields obeys the Helmholtz equation. This equation in cylindrical coordinates is:

$$\frac{d^2u}{dr^2} + \frac{1}{r}\frac{du}{dr} + \left(n^2(r)k_0^2 - \beta^2 - \frac{l^2}{r^2}\right) u = 0, \tag{5.12}$$

where k_0 is the wavenumber and β is propagation constant. l is an integer number known as the azimuthal index and related to the periodic behavior of the guided mode in ϕ. Solving this equation results in a Bessel function ($J_l(x)$) and modified Bessel function ($K_l(x)$) for core and cladding, respectively [134]. For each azimuthal index l, the equation has multiple solutions yielding discrete propagation constants

β_{lm}, $m = 1, 2, \ldots$, which each solution representing a mode shown with LP_{lm}. By substituting electric and magnetic fields in Eq. 5.12 and applying the boundary conditions, one can derive the fields. Here, the intensity of each mode is proportional to $u_{lm} \cos^2 l\phi$. The modes of a fiber with $n_{\text{core}} = 1.4949$, $n_{\text{cladd}} = 1.4533$, $a_{\text{core}} = 1.6$ μm, for wavelength $\lambda_0 = 700$ nm is shown in Fig. 5.3. This fiber is a commercial fiber (Thorlabs UHNA 3) and it is presented as a reference fiber in Sec. 4.2

5.2 Article III: Focused Gaussian beam in the paraxial approximation

Bibliographic Information

A. Das, N. Soltani, M. Agio, "Focused Gaussian beam in the paraxial approximation," Optics Letters 45, 6752-6754 (2020).

Author's contribution

The author contributed to theory development and revisions.

Copyright Notice

Abstract

A focused Gaussian beam represents a case of high practical importance in many areas of optics and photonics. We derive analytical expressions for a focused Gaussian beam in the paraxial approximation, considering an arbitrary lens filling factor. We discuss the role of higher-order Bessel functions of the first kind in defining the electric field in the focal region.

Introduction

The focus of light is theoretically understood as a diffraction problem [135]. In the case of strong focusing, vectorial diffraction leads to diffraction integrals [136] or to a multipole expansion [137] for the representation of the field in the focal region. When the paraxial approximation is applicable, for example in the case of a thin lens, scalar diffraction theory leads to an analytical expression of the focused field. This is the case of the well-known Airy pattern in the Abbe theory of optical resolution.

The electric field profile in the focal region not only depends on the focusing system but also on the incident beam [138]. The case of a Gaussian beam focused by a lens or by a microscope objective is of high practical importance in optics and photonics and its solution based on vectorial diffraction theory or on the paraxial approximation is a textbook result [33, 135]. However, the paraxial approximation is often related to the special situation, in which the beam overfills the objective, such that the diffraction problem reduces to that of a plane wave.

Here, we analyze the general situation, in which the lens filling factor of a focused Gaussian beam, i.e. the ratio between the beam waist and the lens aperture, varies from underfilled to overfilled. Starting from vectorial diffraction theory, we derive analytical expressions in the paraxial approximation for the electric field profile in the focal region.

We show that the solution to the diffraction problem is a superposition of terms, which reduces to the well-known Airy function when the beam overfills the objective lens, i.e., the case of a focused plane wave. Our findings expand the theoretical treatment of focused Gaussian beams and they are relevant for a wide range of practical situations, such as free-space fiber coupling [139], microscopy [140] and laser-beam micro machining [141].

Theory

Our starting point is an x-polarized Gaussian beam profile for the electric field vector

$$\vec{E}_{\text{inc}} = \hat{x} E_0 \exp\big\{(-f^2 \sin\theta^2/w_0^2)\big\}, \tag{5.13}$$

where f is the focal length of an objective lens fulfilling the sine condition [136], w_0 is the beam waist and θ is the angle between the optical axis and a ray on the objective lens converging to the focal point. The x-component of the electric field in the focal plane, $E(\rho)$, where ρ is the distance from the optical axis, can be obtained from the Debye diffraction integrals [33]

$$\begin{gathered} E(\rho) = E_0 \int_0^{\theta_\mathrm{m}} e^{(-f^2 \sin\theta^2 / w_0^2)} \sqrt{\cos\theta} \times \\ \sin\theta (1+\cos\theta) J_0(k\rho \sin\theta) \mathrm{d}\theta, \end{gathered} \tag{5.14}$$

where θ_m is related to the numerical aperture (NA) of the objective lens through NA$= n\sin\theta_\mathrm{m}$. A sketch of the focusing problem is displayed in the inset of Fig. 5.4, where one can see that $f\sin\theta_\mathrm{m}$ defines the lens aperture. The refractive index n of the background medium is equal to 1 for simplicity.

In the paraxial approximation, the NA of the objective lens is assumed to be small, hence $\sin\theta \simeq \theta$ and $\cos\theta \simeq 1$. Nevertheless, this approximation can be used here even if the NA is not small, as long as the Gaussian beam underfills the objective lens. In other words, the apodization function $\exp\{(-f^2\sin\theta^2/w_0^2)\}$ vanishes, even before θ approaches θ_m, when $f\theta \gg w_0$ (underfilled objective). Hence, θ_m can also be understood as the smallest angle between the one determined by the NA and the one determined by the condition $\exp\{(-f^2\sin\theta^2/w_0^2)\} \ll 1$. We can therefore write

$$E(\rho) = 2E_0 \int_0^{\theta_\mathrm{m}} e^{(-f^2\theta^2/w_0^2)} \theta J_0(k\rho\theta) \mathrm{d}\theta. \tag{5.15}$$

We consider $x = k\rho\theta$ and take advantage of a property of the Bessel functions of the first kind [142], namely

$$\frac{\mathrm{d}}{\mathrm{d}x}\left[x^n J_n(x)\right] = x^n J_{n+1}(x). \tag{5.16}$$

By partial integration of the right-hand-side in Eq. (5.15) it can be shown that

$$\int e^{-\alpha x^2} x J_0(x) \mathrm{d}x = e^{-\alpha x^2} \sum_{n=1}^{\infty} (2\alpha)^{n-1} x^n J_n(x), \tag{5.17}$$

with $\alpha = f^2/(k\rho w_0)^2$. Using Eq. (5.17) into Eq. (5.15), we derive a general expression for the electric field in the focal plane

$$E(\rho) = 2E_0\theta_\mathrm{m}^2 e^{(-f^2\theta_\mathrm{m}^2/w_0^2)} \sum_{n=1}^{\infty} \left[\frac{2f^2\theta_\mathrm{m}^2}{w_0^2}\right]^{n-1} \frac{J_n(k\rho\theta_\mathrm{m})}{(k\rho\theta_\mathrm{m})^n}. \tag{5.18}$$

For $w_0 \gg f\theta_\mathrm{m}$, we obtain the usual expression of the electric field in the paraxial approximation

$$E(\rho) \simeq 2E_0\theta_{\mathrm{m}}^2 \frac{J_1(k\rho\theta_{\mathrm{m}})}{k\rho\theta_{\mathrm{m}}}. \tag{5.19}$$

On the other hand, for $f\theta_{\mathrm{m}} \geq w_0$, i.e., for an underfilled objective lens, the higher order terms in Eq. (5.18) must be taken into account.

To further investigate the role of the additional terms, we derive an asymptotic expression valid near the focal point, i.e., $k\rho\theta_{\mathrm{m}} \ll 1$, using the fact that $J_n(x)/x^n \simeq 1/(2^n n!)$ for x close to zero [142]. Although these terms have a rapidly decreasing contribution to the electric field amplitude, it should be considered that they are multiplied by $(f^2\theta_{\mathrm{m}}^2/w_0^2)^n$. The result is an electric field amplitude, which depends on the filling factor of the objective lens, i.e.,

$$\begin{aligned} E(\rho) &\simeq E_0 e^{(-f^2\theta_{\mathrm{m}}^2/w_0^2)} \sum_{n=1}^{\infty} \left(\frac{f^2}{w_0^2}\right)^{n-1} \frac{\theta_{\mathrm{m}}^{2n}}{n!}, & (5.20) \\ &= E_0 \frac{w_0^2}{f^2}\left[1 - \exp\left\{\left(-f^2\theta_{\mathrm{m}}^2/w_0^2\right)\right\}\right]. & (5.21) \end{aligned}$$

Underfilling the objective lens reduces the field amplitude in the focal spot by

$$\exp\left\{(-f^2\theta_{\mathrm{m}}/w_0^2)\right\}.$$

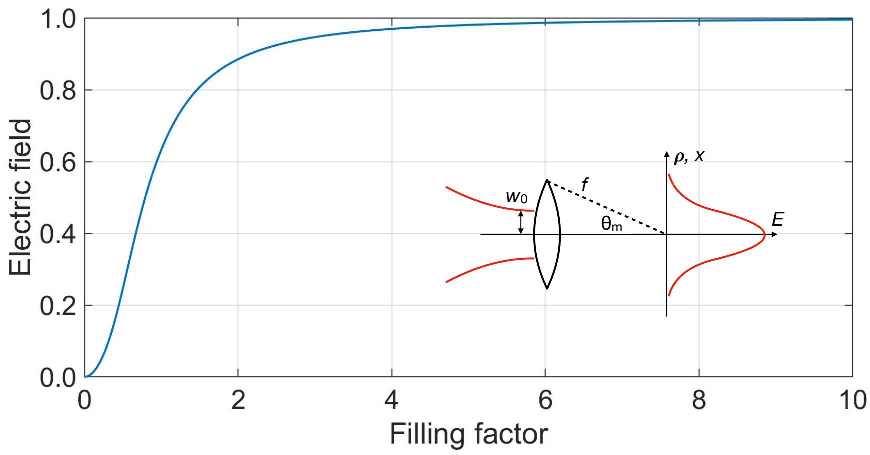

Figure 5.4: Normalised electric field amplitude in the focal spot, $E(0)/E_0\theta_{\mathrm{m}}^2$, as a function of the lens filling factor $w_0/f\theta_{\mathrm{m}}$. Inset: a sketch of a focused Gaussian beam with the relevant quantities: beam waist w_0, lens focal length f, lens angular aperture θ_{m}, electric field in the focal plane E, and transverse coordinates ρ, $x = \pm k\rho\theta_{\mathrm{m}}$.

We present our results in the most possible general form and discuss the main findings. For instance, they are fully independent of the particular choice of the NA, being the electric field expressed as a function of the filling parameter $w_0/f\theta_{\mathrm{m}}$.

By setting the focal length, the NA, or the beam waist, one can easily calculate the solution for the case of interest. Here, we consider the electric field amplitude in the focal spot, in the focal plane, and in the contributions of the higher-order terms.

In Fig. 5.4, we plot the field amplitude in the focal plot (see Eq. (5.21)) as a function of $w_0/f\theta_\mathrm{m}$. The case $w_0/f\theta_\mathrm{m} \to \infty$ represents an overfilled objective lens, whereas the case $w_0/f\theta_\mathrm{m} \to 0$ represents an underfilled objective lens.

We notice that the electric field amplitude increases with the filling parameter, and it saturates to its maximum value when the filling parameter is larger than about two. This gives an indication of an appropriate choice of the beam waist or the lens focal length for optimizing the focusing strength.

For instance, the practical situation of a commercial microscope objective with NA=0.3 and a working distance of 10 mm, corresponding to $f\theta_\mathrm{m} \simeq 3$ mm, and a laser beam with a waist of 1-2 mm would lead to a lens filling factor of the order of 0.3 - 0.6. Therefore, in the following, we want to investigate the field profile in the focal plane, especially when the filling parameter is less than one.

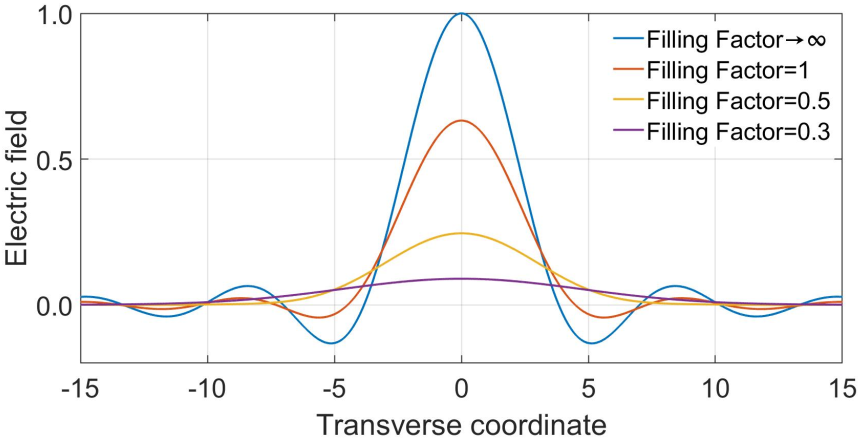

Figure 5.5: Normalised electric field amplitude in the focal plane, $E(x)/E_0\theta_\mathrm{m}^2$, where $x = \pm k\rho\theta_\mathrm{m}$ is the transverse coordinate, for filling factors $w_0/f\theta_\mathrm{m} = \infty$, 1, 0.5 and 0.3. The first case corresponds to the result of Eq. (5.19).

The field profile in the focal plane (see Eq. (5.18)) is investigated for different representative values of the lens filling factor, namely $w_0/f\theta_\mathrm{m} = 1$, 0.5, and 0.3. Figure 5.5 plots the result as a function of $x = \pm k\rho\theta_\mathrm{m}$, in which we used up to twenty terms in the sum of Eq. (5.18). The field profile of Eq. (5.19) (Airy pattern) is also shown for comparison.

For a filling parameter of the order of one, $w_0/f\theta_\mathrm{m} = 1$, the field profile resembles the typical diffraction pattern of a circular opening, which becomes the Airy pattern in the limiting case of $w_0/f\theta_\mathrm{m} \to \infty$, see Eq. (5.19). On the other hand, when the filling parameter decreases, the field profile acquires a smooth shape without oscillations. Moreover, its full width at half maximum (FWHM) increases because of less focusing strength by the lens. Notice also the variation of the field maximum, which rapidly decreases with the filling factor, in agreement with the results of Fig. 5.4. These findings are valid for any NA as long as the paraxial approximation holds. The evolution of the field profile to a smooth function is determined by the summation in Eq. (5.18).

Next, we discuss in more detail the contribution to the field amplitude for the various terms in Eq. (5.18), namely

$$E_n(x) = \left[\frac{2f^2\theta_{\mathrm{m}}^2}{w_0^2}\right]^{n-1} \frac{J_n(x)}{x^n}. \tag{5.22}$$

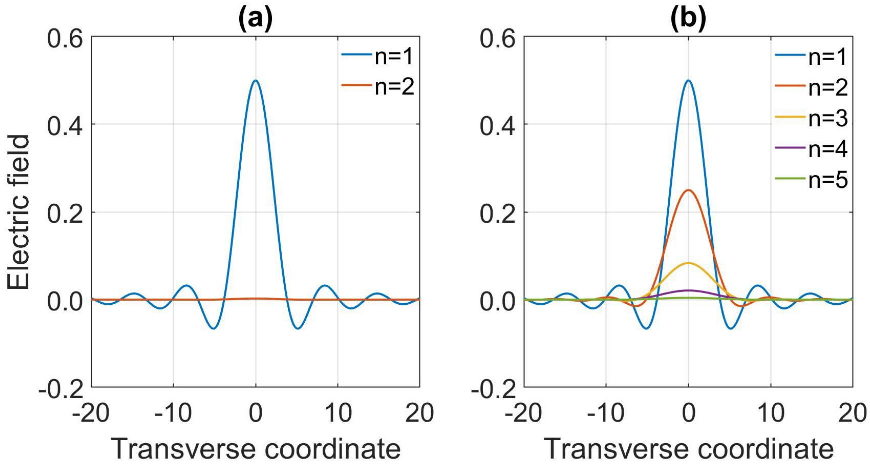

Figure 5.6: Normalised electric field amplitude in the focal plane, $E(x)/E_0\theta_{\mathrm{m}}^2$, where $x = \pm k\rho\theta_{\mathrm{m}}$ is the transverse coordinate, for filling factors $w_0/f\theta_{\mathrm{m}} = 10$ (a) and 1 (b). Each curve corresponds to a term in the summation of Eq. (5.18), see also Eq. (5.22).

Figures 5.6(a)-(b) respectively plot the individual terms in Eq. (5.18) as a function of $x = \pm k\rho\theta_{\mathrm{m}}$ for $w_0/f\theta_{\mathrm{m}} = 10$ and 1. For $w_0/f\theta_{\mathrm{m}} = 10$, only the very first term contributes to the electric field amplitude, which corresponds to the Airy pattern (see Fig. 5.6(a)). For $w_0/f\theta_{\mathrm{m}} = 1$, one can see in Fig. 5.6(b) that the first four terms contribute to the field profile. However, they still result in a diffraction pattern with positive and negative values of the electric-field amplitude, as shown in Fig. 5.5.

In order to better understand the evolution of these terms, Fig. 5.7 plots $E_n(x)$ (see Eq. (5.22)) for $x = 0$, which reads

$$E_n(0) = \left[\frac{f^2\theta_{\mathrm{m}}^2}{w_0^2}\right]^{n-1} \frac{1}{2n!}. \tag{5.23}$$

When $w_0/f\theta_{\mathrm{m}}$ gets smaller, one notices that the main term is not the first one anymore. The higher-order terms get larger and become the predominant contribution to the field profile. As a result, the field oscillations in the focal plane disappear, as shown in Fig. 5.5 for $w_0/f\theta_\mathrm{m} = 0.5$ and 0.3. Moreover, Fig. 5.7 indicates that the higher-order terms are maximal at a value n dependent on the filling parameter and that they eventually vanish for $n \to \infty$. Indeed, the summation in Eq. (5.18) is always convergent, as proven by Eq. (5.23).

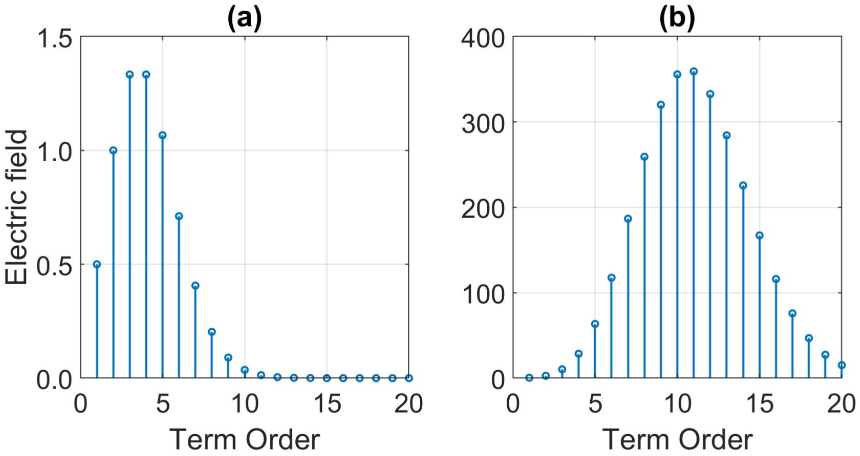

Figure 5.7: Electric-field terms in Eq. (5.23) as a function of n, for $w_0/f\theta_\mathrm{m}$ = 0.5 (a) and 0.3 (b).

Conclusions

In summary, we study the electric field profile of a focused Gaussian beam in the paraxial approximation in the general and practical important case, where the beam waist does not overfill the objective lens. We provide analytical expressions starting from vectorial diffraction theory, and by making use of the paraxial approximation, we show that the apodization function of the Gaussian beam produces a summation of terms containing Bessel functions of the first kind of increasing order, $J_n(x)$. When the beam overfills the objective lens, our expressions approach the well-known Airy pattern, which only contains the Bessel function of the first kind, $J_1(x)$. In all other cases, the higher-order terms must be taken into account. They are responsible for the suppression of the oscillatory behavior of the electric field profile in the focal plane, as expected from the zero-field amplitude of the incident beam at the edge of the objective lens. These findings contribute to a better understanding of focused Gaussian beams and provide a quantitative analytical tool to solve practical problems involving Gaussian beams in optics and photonics.

5.3 Article IV: Planar antenna designs for efficient coupling between a single emitter and an optical fiber

Bibliographic Information

N. Soltani, M. Agio, ”Planar antenna designs for efficient coupling between a single emitter and an optical fiber,” Optics Express 27, 30830-30841 (2019).

Author’s contribution

The author contributed to theory development, calculation, drafting of the manuscript, and revisions.

Copyright Notice

Abstract

Fluorescence detection is a well-established readout method for sensing, especially for in-vitro diagnostics (IVD). A practical way to guide the emitted signal to a detector is by means of an optical fiber. However, coupling fluorescence into a fiber is challenging and commonly lacks of single-molecule sensitivity. In this work, we investigate specific fiber geometries, materials, and coatings that, in combination with a planar Yagi–Uda antenna, allow to reach efficient excitation and collection. The simulation of a practical setting determines more than 70% coupling efficiency for a horizontally-oriented dipole, with respect to the planar antenna, emitting at 700 nm and embedded in polyvinyl alcohol (PVA). Moreover, the coupling efficiency would only scale by a factor of 2/3 for emitters with random orientation as a result of the antenna geometry. These findings are relevant for single-molecule detection with fiber optics and have implications for other applications involving the coupling of light with nano-scale sources and detectors. Scanning the surface of a sample with such fibers could also be advantageous for imaging techniques to provide low background noise and a high resolution.

Introduction

Optical waveguides can be used to transfer light much more efficiently than free space optics [143], thus representing a desirable practical method for nano-particle detection, fluorescent sensing, and single-photon sources [67, 144–147]. However, coupling the emitted light into a waveguide can be inefficient due to the dipolar radiation pattern of nano-scale sources, and for this reason, it is still a challenging research task [148–150].

One method that has been extensively explored is direct fiber coupling, where the dipole source is located in the vicinity of a single-mode fiber tip. Fiber-based micro-cavities [65], fibers with a nano-scale tapered tip [151], lensed fibers [152] and etched single mode fibers [153] are a few examples of this approach. On the other hand, multimode fibers, which have a larger core size ($\sim$50 μm), suffer from mode mismatch with the near field of the dipole.

Another method is embedding the molecules inside the waveguide [154, 155]. The coupling efficiency could reach up to 70% in a tapered fiber, but the approach requires immobilization of the molecules in the fiber, which is not always desirable. Moreover, researchers have investigated the evanescent coupling to a tapered fiber [156–159]. This method is particularly useful for single-molecule detection, but it is quite challenging from a practical point of view. The reported coupling efficiency for this technique varies from 10% to 80% in the simulations, depending on the fiber size and the material.

Recently, a planar antenna structure that beams the emission of single molecules has been proposed [22, 62]. This relies on the concept of an optical Yagi–Uda antenna [160], where the reflector and the director elements are thin metal films. Hence, the antenna strongly modifies the emission pattern leading to a half-width at half maximum of fewer than 20 degrees. This modification can be applied to the concept of fiber collection.

Here, we investigate the coupling of a dipolar emitter in a planar antenna with an optical fiber, which has a core radius larger than the source emission wavelength λ (hence excluding the case of nano-fibers [151]) and a facet coated with a thin gold layer, acting as director element. This configuration improves the overlap of the radiated field with the guided modes in the fiber. As a result, the coupling efficiency of the dipole into the fiber increases.

The proposed detection scheme is targeting, especially, bioassays based on surface chemistry, in which the vertical position of the molecule can be defined, for instance, as in surface-plasmon resonance biosensors [161].

Furthermore, we study the relationship between mode coupling efficiency and the numerical aperture (NA) of the fiber. The critical numerical aperture, for which the fiber has the maximum coupling efficiency, has been obtained. The coupling efficiency of a dipole embedded in different transparent materials has also been calculated. This is relevant for the efficient coupling of organic molecules in media such as water. Finally, the effect of tilting and displacement of the fiber in the setup is investigated.

Methodology and layout of the problem

In order to optimize the coupling efficiency of a dipole into a fiber, the geometry, material, and position of the fiber must be specified. This includes many variables such as core radius, refractive indices of core and cladding, the reflector-director distance, the active medium in which the dipole source is embedded, and so on. In this work, the effect of these variables for the optimization of the fiber coupling is studied using the finite-difference time-domain (FDTD) method [162]. The simulations have been performed with a commercial software package (FDTD Solutions, Lumerical Inc. [90]). To reduce the computation time and memory, we took advantage, whenever possible, of the symmetry of the layout. Symmetric boundary conditions are implemented by forcing the appropriate field components to zero. These boundaries can not be used for tilting and radial displacement of the dipole from the center.

We consider a gold substrate as the reflector, in which a dipole emitter is located at a distance d_1, creating an image dipole [163]. The distance between the dipole and fiber tip in the radiation direction is denoted as d_2, shown in Fig. 5.8. When two dipoles radiate with an appropriate phase delay, they can give rise to a beaming effect in a certain direction. This occurs when d_1 and d_2 fall within the range of $\lambda/(6n) < d_{1,2} < \lambda/(4n)$, where λ is the emission wavelength and n is the refractive index of the active medium [22, 62].

The radiated power (P_r) is calculated as the power passing through a frequency-domain field monitor across the fiber (see Fig. 5.8) at a distance 4λ in the radiation direction and it corresponds to the power out-coupled from the planar antenna [22].

The power transmitted into the mode m of the fiber is determined by the overlap integral (a_m) of the guided mode across the fiber.

$$a_m = 0.25 \left(\frac{\int d\vec{S} \cdot \vec{E}_{\text{in}} \times \vec{H}_m^*}{N_m} + \frac{\int d\vec{S} \cdot \vec{E}_m^* \times \vec{H}_{\text{in}}}{N_m^*} \right) , \tag{5.24}$$

where m is the number of the selected mode in the fiber, $\vec{E}_{\text{in}}$ and $\vec{H}_{\text{in}}$ are the radiated electric and magnetic fields, respectively. $\vec{E}_m$ and $\vec{H}_m$ are the modal fields of the fiber and N_m can be calculated from

$$N_m = 0.5 \int d\vec{S} \cdot \vec{E}_m \times \vec{H}_m^* , \tag{5.25}$$

where, $\text{Re}[N_m]$ is the power of the mode m in the fiber [143].

The dipole has a fixed amount of power in free space, known as the source power (P_s). The ratio of the total emitted power of the dipole inside the system (P_t) over the source power gives the Purcell factor (F):

$$F = \frac{P_t}{P_s} . \tag{5.26}$$

The fraction of power transmitted into the mode m of the fiber can be described by:

$$T_m = \frac{|a_m|^2 N_m}{P_t} . \tag{5.27}$$

This equation describes the coupling efficiency into the mode m with respect to the total emitted power [143], which we discuss in the following section together with the Purcell factor. We have compared our FDTD simulations against a few different case studies (see Ref. [65]), finding an excellent agreement.

One way to enhance the overlap integral is to change the fiber geometry and material. Further enhancements can be obtained by coating a thin gold layer on the tip of the fiber, also known as a director, which provides directional beaming.

In all simulations, the dipole source has a horizontal orientation with respect to the reflector in order to minimize the coupling of energy to surface plasmon-polariton (SPP) modes present in both the reflector and the director interfaces. The emission of vertically oriented dipoles is quenched by the antenna. Therefore, for the case of molecules with the tilted dipole moment, the detection efficiency would scale as $\sin^2\phi$, where ϕ is the angle between the dipole orientation and the antenna axis. For randomly-oriented molecules, the detection efficiency would thus be reduced by a factor of 2/3, which corresponds to the average value of $\sin^2\phi$ over the solid angle.

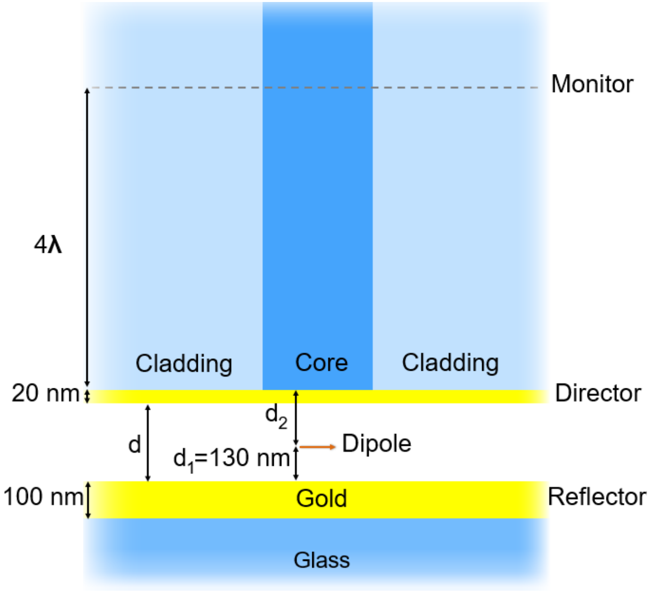

Figure 5.8: Simulations layout. A single dipole is situated 130 nm above a gold-coated substrate (reflector). The dipole emission is collected by the fiber and monitored with a frequency-domain field profile. The monitor is placed in the far-field, approximately 4λ *from the dipole. The cladding radius, fiber length, and substrate (glass) are semi-infinite. The values of the fixed parameters are given in the figure. The distance d between director and reflector is* $d = d_1 + d_2 - 20$ *nm.*

For simplicity, some of the following geometrical parameters are considered constant (see Fig. 5.8). The cladding radius is infinitely large. The distance between the reflector and dipole is $d_1 = 130$ nm (except Fig. 5.15). The frequency-domain field monitor for the overlap integral calculation is located far inside the fiber, but the exact position is not critical. The thicknesses of the reflector and director are assumed to be 100 nm and 20 nm, respectively. Changing the thickness of the director could also affect the coupling efficiency. For instance, when the director is 20 nm thick, the coupling efficiency into the fundamental mode of the fiber has a maximum value of 50%. However, this value reduces to 44% for 30 nm and 43% for 10 nm director thickness at a constant reflector-director distance, $d = 295$ nm. Further simulations show that having a thicker director increases the directionality, but the radiated power decreases [22].

The adhesion of the gold director on the tip of the fiber can be improved by adding a thin layer of titanium. Calculations show that the inclusion of a 2 nm-thick titanium film does not substantially increase losses. We find that, for the designs of Fig. 5.8, P_r drop by about 2%, when 2 nm of gold are replaced by 2 nm of titanium [92]. Adding an adhesion layer to the reflector does not affect the antenna's properties since the gold layer is thick, and light cannot pass through it.

Results and discussion

Coupling enhancement with a designed fiber

Coupling light radiated by a single dipole emitter into a commercial fiber (single mode, e.g., SM600) without any objective lens is challenging. This is due to the mismatch of fiber mode (see Fig. 5.9(a)) and a dipole field. The coupling efficiency can be increased by placing a reflecting layer behind the emitter (see in Fig. 5.9(c) the radiated field profile into the fiber), and it can be further improved by adding a director layer on the fiber tip (see Fig. 5.9(d)). The dipole is centered with respect to the fiber, and its emission has been set at $\lambda = 700$ nm. This represents the wavelength range of well-known near-infrared dyes and solid-state quantum emitters [164–166].

Alternatively, shrinking the core radius to 0.8 μm and using materials with higher refractive index contrast for the core and the cladding could also enhance the efficiency. Figure 5.9(b) shows the fundamental guided mode of such fiber, while Fig. 5.9(e) and 5.9(f) show the radiated field into the fiber after adding a gold reflector and a director, respectively. In Fig. 5.9, the reference fiber is a solid core optical fiber with the following parameters: core radius (R_core) = 1.6 μm, core refractive index (n_core) = 1.4949, cladding radius (R_cladding) = 50 μm and cladding refractive index (n_cladd) = 1.4533, which are approximate to the commercially available fiber from Thorlabs "UHNA3", high NA single mode fiber. The common single-mode fibers, such as Thorlabs SM600, has a coupling efficiency of less than 1% due to the low NA. For the customized fiber the parameters are: $R_\mathrm{core} = 0.8$ μm, $n_\mathrm{core} = 1.45$, $R_\mathrm{cladding} = 50$ μm and $n_\mathrm{cladd} = 1.3$.

Since the radiated field from the dipole in the planar Yagi–Uda antenna exhibits a small emission angle, the core size of the fiber should be smaller than that of commercial fibers. In addition, a high-NA enables greater light collection into the fiber. These conditions can be achieved by tapering the core of a commercial fiber adiabatically [167–169] or making photonic-crystal cladding fiber [170]. Figure 5.9(g) compares the coupling efficiency of reference fiber and custom fiber at different distances (d) between the reflector and the director.

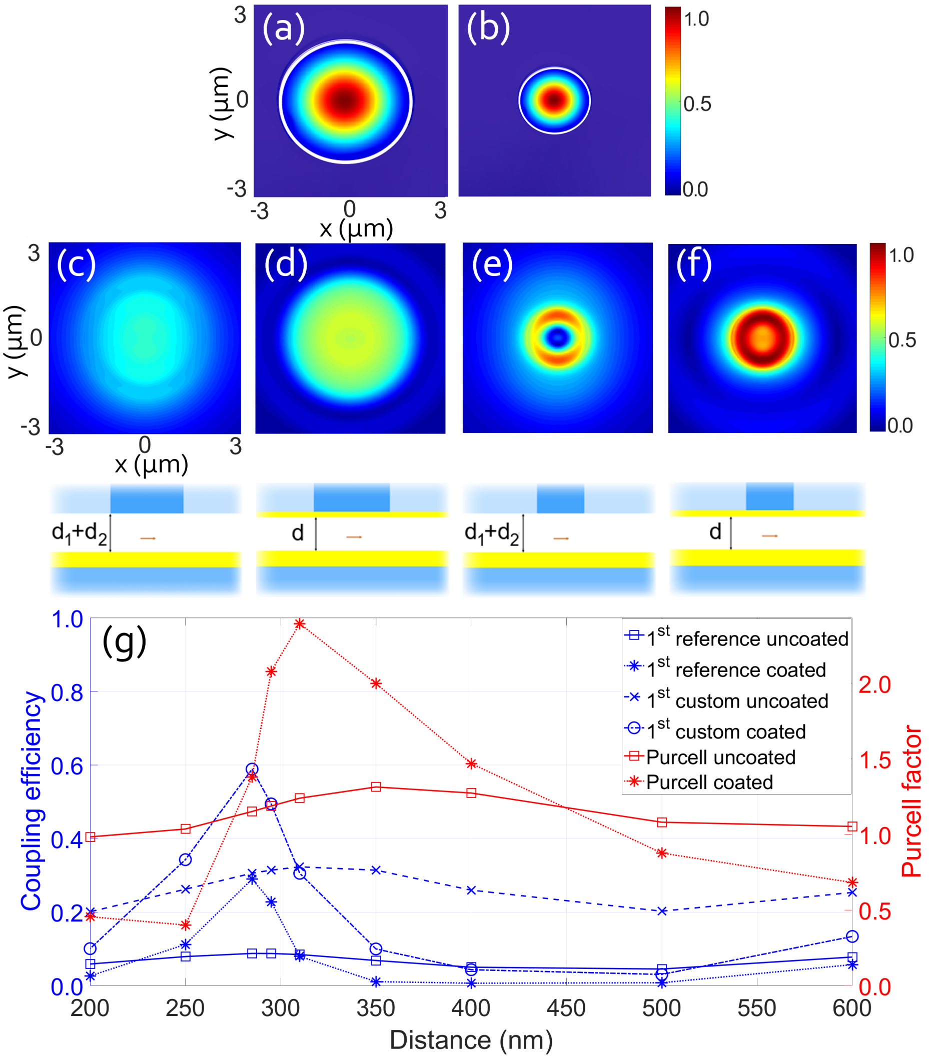

Figure 5.9: Propagation of fundamental mode in (a) reference fiber (R_{core} = 1.6 μm, $n_{\text{core}} = 1.4949$ and $n_{\text{cladd}} = 1.4533$) and (b) custom fiber ($R_{\text{core}}$ = 0.8 μm, $n_{\text{core}} = 1.45$ and $n_{\text{cladd}} = 1.3$) simulated by the commercial software Mode Analysis, Lumerical Inc. [90]. In (a) and (b), the white line shows the fiber core, and they have the same color bar. The radiated field of the dipole at 4λ away from the source for (c) reference fiber with reflector and distance $d_1 + d_2 = 295 + 20$ nm, (d) reference fiber with reflector-director and distance $d = 295$ nm, (e) custom fiber with reflector and $d_1 + d_2 = 295 + 20$ nm, and (f) custom fiber with reflector-director with distance $d = 295$ nm has been shown. (c)-(f) are normalized with respect to the maximum value in (f) and have the same color bar. In each case, the geometry of the simulation is depicted below the field image. (g) Plots of the radiated field into the fiber for the reference fiber (c), (d) and the custom (e), (f) configurations with respect to the reflector-director distances, normalized by the total emitted power P_t of the dipole. The right axis indicates the Purcell factor of the dipole, which can be multiplied by the coupling efficiency to determine the power coupled to the fiber. This indicates that, however, the mode reaches the maximum coupling (59%) at 285 nm, but a larger collected power is obtained at 295 nm due to the Purcell factor.

In Fig. 5.9, the coupling efficiency is simulated for different distances between 200 nm to 600 nm. For the custom-designed fiber with the director, despite the cavity effect at 350 nm and 700 nm, the maximum coupling is at 295 nm due to antenna effect [22]. More interestingly, even a dipole at the center of the active medium ($d_1 = 350$ nm) when $d = 700$ nm does not give a higher coupling efficiency for both custom-designed and the reference fiber.

Our analysis demonstrates that a custom fiber is capable of collecting a greater number of photons compared to those emitted by a dipole emitter in a vacuum. This is due to the Purcell factor, which reaches a value of 2.1 at $d = 295$ nm. By multiplying the coupling efficiency and the Purcell factor, one can find the coupling efficiency normalized with respect to the fixed value P_s. Consequently, the ratio between the power coupled into the fundamental mode (see Eq. (5.24) and (5.26)) and the source power (P_s) is $T_1/P_s = 1.06$.

Critical numerical aperture

Next, we investigate the relationship between the collection efficiency and the fiber NA. The numerical aperture of a fiber is calculated by

$$\mathrm{NA} = \sqrt{n_{\mathrm{core}}^2 - n_{\mathrm{cladd}}^2}\,, \tag{5.28}$$

where n_{core} and n_{cladd} are the refractive indices for the core and the cladding of the fiber, respectively [171].

A fiber with high NA could enhance the collected light from a single dipole, but this enhancement does not increase with the NA. For a fixed value of n_{core}, reducing the refractive index of the cladding below a certain value will not change the coupling efficiency as shown in Fig. 5.10. Using the n_{cladd} values depicted in Fig. 5.10, one can find the critical NA using Eq. (5.28).

In Fig. 5.10, $n_{\mathrm{core}} = 1.45$ and n_{cladd} varies from 1 (air) to 1.44 (close to the refractive index of the core). The graph indicates that below $n_{\mathrm{cladd}} = 1.3$, the coupling efficiency is almost constant. This is called critical NA, and for such fiber, it is equal to 0.64. Furthermore, the critical NA depends on the core size and its refractive index. This value is in the range between 0.45 to 0.65 for different sizes or refractive indices of the core in the free space medium. This shows that having a high-NA fiber is essential for the coupling, but fibers with very large NAs are not necessary.

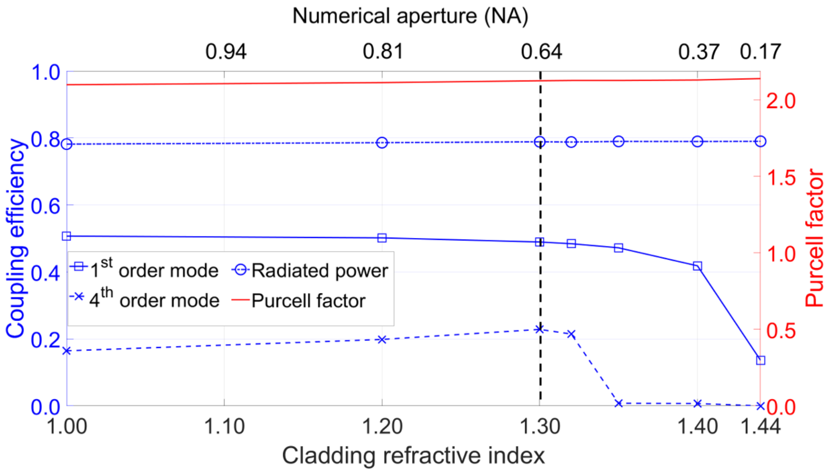

Figure 5.10: NA of the fiber, represented by varying cladding refractive index n_{cladd}. The core radius here is 0.8 μm and it has a refractive index of 1.45 (custom fiber configuration). This figure indicates that for high-NA fibers, there is more than one propagating mode. The curves show that for n_{cladd} smaller than 1.3, the coupling efficiency is nearly constant for the modes. By using Eq. (5.28), the critical NA is equal to 0.64 (black dashed line). The radiated power curve indicates the total out-coupled light from the reflector-director configuration in the propagation direction normalized by total emitted power P_t.

Fiber core radius and higher order mode coupling

As shown in Fig. 5.9 the coupling efficiency rises when the fiber is coated with a thin gold layer. This happens not only for the fundamental mode but also for some higher-order modes. The number of modes in a fiber depends on the core radius and the NA of the fiber. The high-NA fibers normally have a higher number of modes compared to the low-NA ones for the same geometry. Moreover, the number of modes increases with the size of the core radius.

Figure 5.11 indicates the coupling efficiency for the 1^{st}, 4^{th} and 9^{th} modes of the fiber with variable core radius. The other modes would just slightly change the coupling strength therefore, we can neglect them. The refractive indices of the core and cladding are 1.45 and 1.3, respectively. By increasing the core size from 0.6 to 2.1 μm, the coupling to a fundamental mode decreases, but the coupling to higher-order modes increases the density of states. This effect has also been shown for a single dipole evanescently coupled to a multimode fiber [148].

Figure 5.11 shows that the fiber with a core radius of 0.4 μm can be used as a single-mode fiber for coupling with more than 50% efficiency. However, the fiber with a slightly larger core size contains few higher-order modes with a reasonable amount of coupling efficiency. Therefore, in Fig. 5.11 the fiber with 1.2 μm core size has a total coupling efficiency of 70% (i.e. $(T_1 + T_4 + T_9)/P_s = 1.55$) due to the contribution of 1^{st}, 4^{th} and 9^{th} order modes.

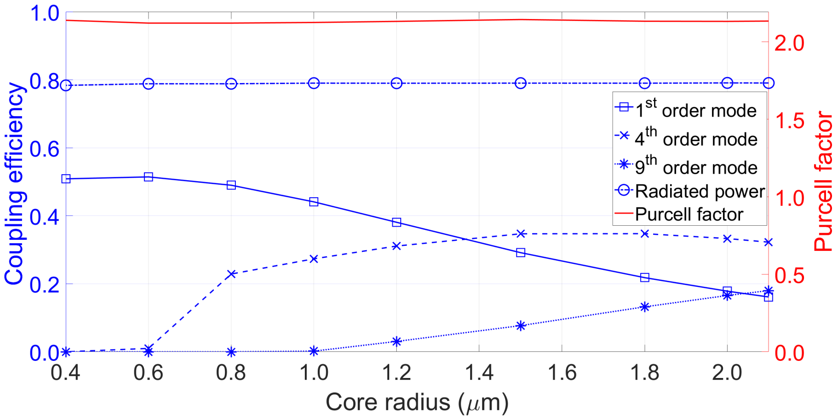

Figure 5.11: Coupling efficiency of different modes in the custom gold coated (director) fiber. The distance is fixed at $d = 295$ *nm. The* 1^{st}, 4^{th} *and* 9^{th} *modes with dipole emission are demonstrated. The red curve points out the Purcell factor (right axis). The radiated power shows that the out-coupled amount of light from the antenna structure does not depend on the size of the core or the cladding. For a core radius less than 1* μ*m, there are only four modes propagating through the fiber, and the fiber with less than 0.4* μ*m core radius is a single mode fiber.*

Distance between the reflector and the director

We have shown that the coupling efficiency is maximal at a specific distance between the reflector and the director (see Fig. 5.9), but actually, the coupling efficiency is relatively high also for determined larger distances. This can be exploited for detecting larger objects, like particles, or even cells in fluids.

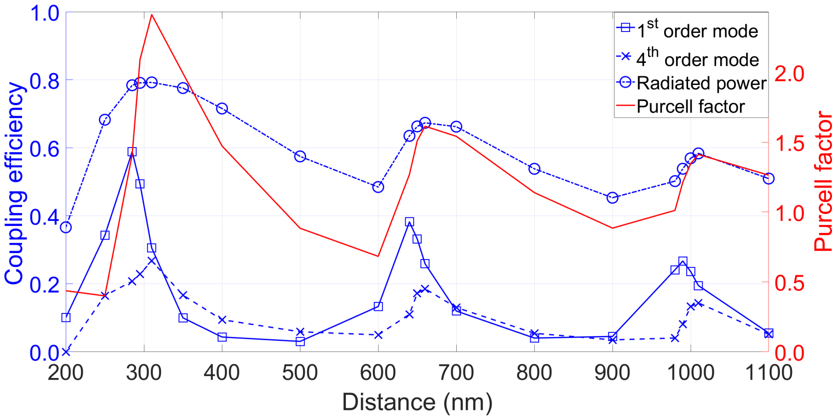

Figure 5.12: Coupling efficiency versus reflector-director distance. The coupling raises fast, but it gradually decreases by increasing the distance. The fluctuation of radiated power and mode coupling efficiency is like the Purcell factor. The distance between every two peaks is 350 nm, which corresponds to $\lambda/2$.

The Purcell effect and the coupling efficiency of the fiber vary when the distance between the director and the reflector changes. Figure 5.12 reveals this for the custom fiber as mentioned in Fig. 5.9. By increasing the distance between the reflector and the director, the coupling efficiency grows and then gradually decreases. This happens due to the transition of the antenna effect with the buildup of the cavity mode in the reflector-director configuration [22]. Moreover, the maximum coupling efficiency is not at the same distance for each mode.

As shown in Fig. 5.12, the coupling efficiency at larger distances is still higher than some other methods for direct fiber coupling. For example, here at $d = 990$ nm, the coupling efficiency of the fundamental mode is 27%, which is much higher than the other methods for direct fiber coupling [172, 173].

Wavelength dependence of dipole-fiber coupling

In all previous simulations, the dipole emitted at a fixed wavelength ($\lambda = 700$ nm). Here, the dipole wavelength is swept from 600 nm to 1200 nm. Figure 5.13 shows the wavelength dependency of the coupling for three different reflector-director distances. The fiber specifications are identical to those of the custom fiber in Fig. 5.9.

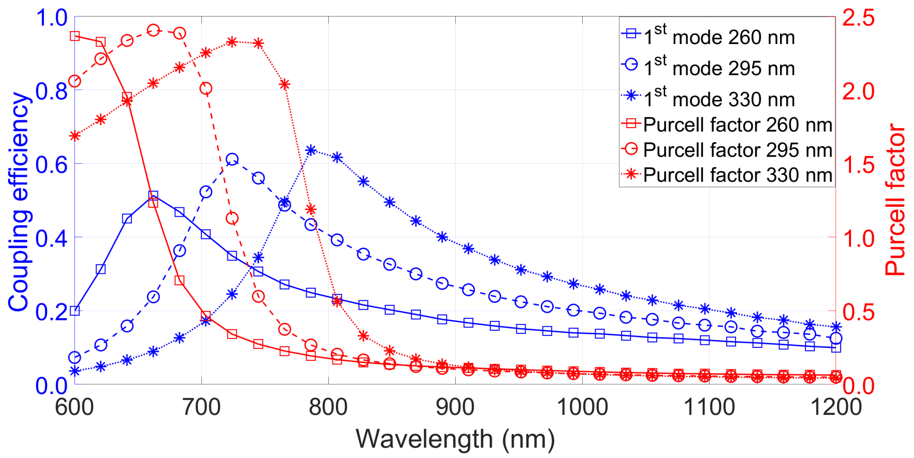

Figure 5.13: Maximum coupling efficiency as a function of wavelength for the reflector-director distance of 260, 295, and 330 nm. It is possible to tune the coupling for the desired wavelength by changing the reflector-director distance.

By increasing the distance between the reflector and the director, the maximum coupling occurs at larger wavelengths. This method can be helpful for spectroscopy measurements [174]. Moreover, it could be exploited to distinguish different fluorescent markers without color cameras or optical filters.

Coupling efficiency in different active media

Positioning a dipole with nanometer accuracy in the air between the reflector and the director is experimentally a challenging task. In addition, some organic molecules would need a liquid or a polymer matrix rather than air. As a result, varying the active medium between the director and the reflector provides an opportunity to explore different types of organic or inorganic emitters.

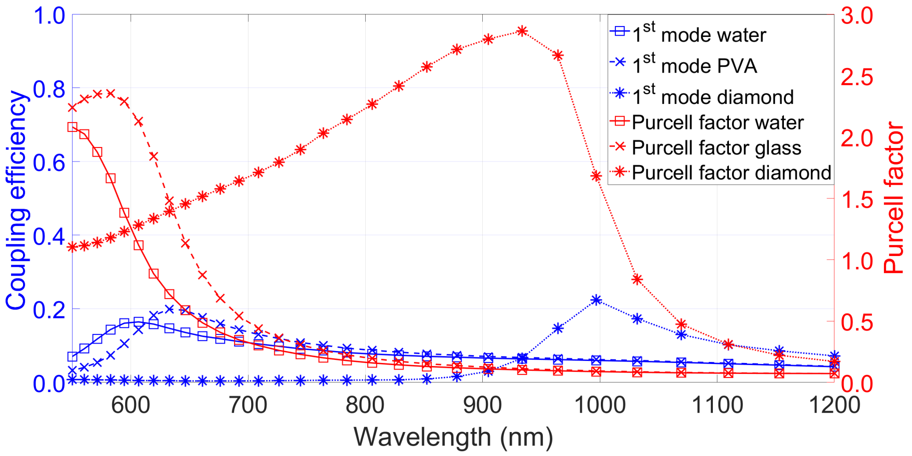

Figure 5.14: Maximum coupling efficiency as a function of wavelength for three different active media, with various refractive indices: $n_{\text{water}} \approx 1.33$*,* $n_{\text{PVA}} \approx 1.47$ *and* $n_{\text{dia.}} \approx 2.41$*. The media have 295 nm thickness.*

Figure 5.14 determines the coupling efficiency for three different materials as an active medium: water ($n_{\text{water}} \approx 1.33$), polyvinyl alcohol (PVA) ($n_{\text{PVA}} \approx 1.47$) and diamond ($n_{\text{dia.}} \approx 2.41$). However, the coupling efficiency is around 20% for these active media, but by changing the core size and material one could improve this efficiency for each case. As an example, the optimal coupling efficiency for PVA is simulated in Fig. 5.15. Here, the distance between the reflector and the dipole is 85 nm and the PVA has a thickness of 180 nm. The coupling efficiency is simulated for two different fibers, "custom", which is the same as the custom fiber in previous simulations ($R_{\text{core}} = 0.8\ \mu$m, $n_{\text{core}} = 1.45$ and $n_{\text{cladd}} = 1.3$) and "optimal" with $R_{\text{core}} = 0.6\ \mu$m, $n_{\text{core}} = 1.77$ and $n_{\text{cladd}} = 1.3$.

By increasing the refractive index of the fiber core the coupling efficiency increases. Moreover, for a large core refractive index, reducing the size of the core could also improve the coupling efficiency. The minimum core size depends on the core refractive index. In Fig. 5.15 the coupling efficiency of 1^{st} and 4^{th} modes of the "optimal" fiber at 700 nm is $\simeq 70\%$ and it can be increased for a higher core refractive index and smaller core size.

For active media, with larger refractive indices the coupling efficiency is not as high as in air due to the excitation of SPP modes at the interface between the gold layers with the dielectric material. This effect can be reduced by introducing intermediate layers with a lower refractive index with respect to active medium [62].

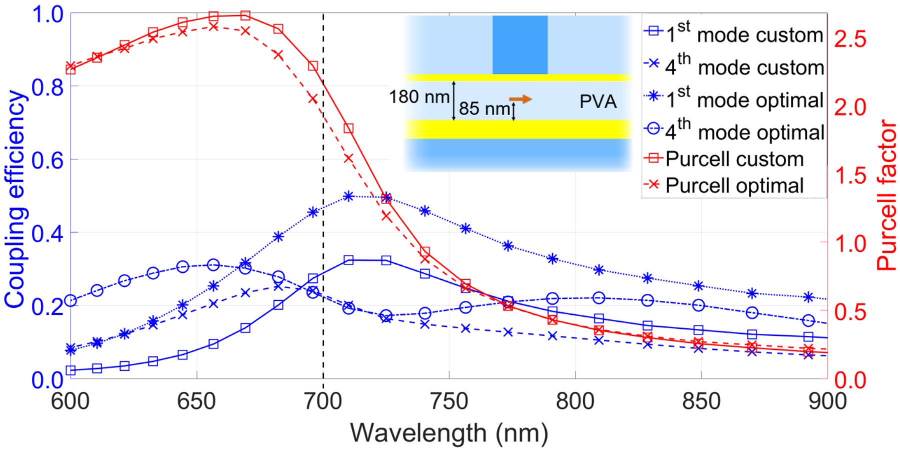

Figure 5.15: Maximum coupling efficiency as a function of wavelength for PVA active medium, with custom fiber (R_{core} = 0.8 μm and $n_{\text{core}} = 1.45$) and so-called optimal fiber (R_{core} = 0.6 μm and n_{core} = 1.77). The inset indicates the reflector-director distance and the dipole position. By adding a higher refractive index active medium, the reflector-director distance and the core radius should be decreased.

Dipole positioning and fiber tilting

The coupling efficiency of the fiber depends on the position of the fiber with respect to the dipole and reflector. By lateral displacement of the dipole from the center of the fiber the coupling efficiency is reduced. Figure 5.16 shows the radial displacement of the dipole from the center along the x-axis for custom design fiber.

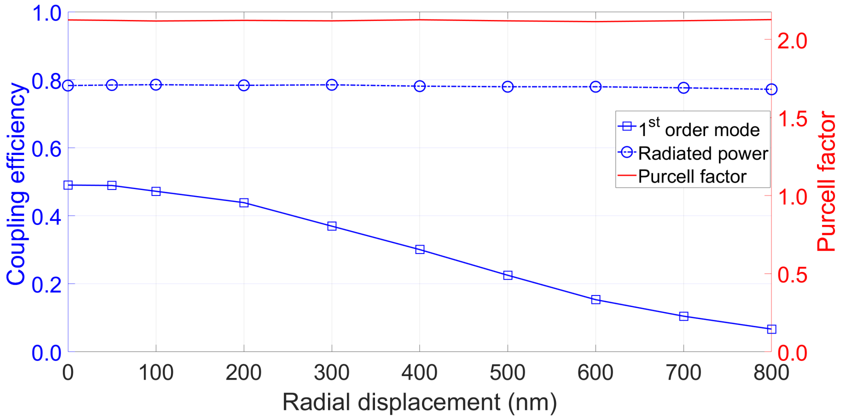

Figure 5.16: Radial distance of the dipole from the optical axis of custom design fiber. The signal has a Gaussian shape with around 800 nm full-width at half-maximum. The coupling efficiency for the higher-order modes is highly dependent on the position of the dipole (not shown).

The coupling-efficiency curve exhibits a Gaussian profile with a full width at half maximum of 800 nm. The sensitivity to the dipole position could thus add challenges to the experiment, but it could also turn out to be useful as a method for microscopy with low background noise.

Moreover, the tilting of the fiber could reduce the coupling efficiency. The coupling efficiency for the fiber without the director layer is almost constant with tilting. Here, the tilting angle (θ) is the angle between the reflector and the director. As shown in Fig. 5.17 the coupling efficiency into the fundamental mode of custom and reference fibers with director drops nearly by 4% for the one-degree tilt of the fiber. As the core radius of the fiber reduces, the tilting has less influence on the coupling efficiency. For a fiber with 0.8 μm core radius (custom fiber), 2 degrees tilting would reduce the coupling efficiency by only $\approx$ 10%.

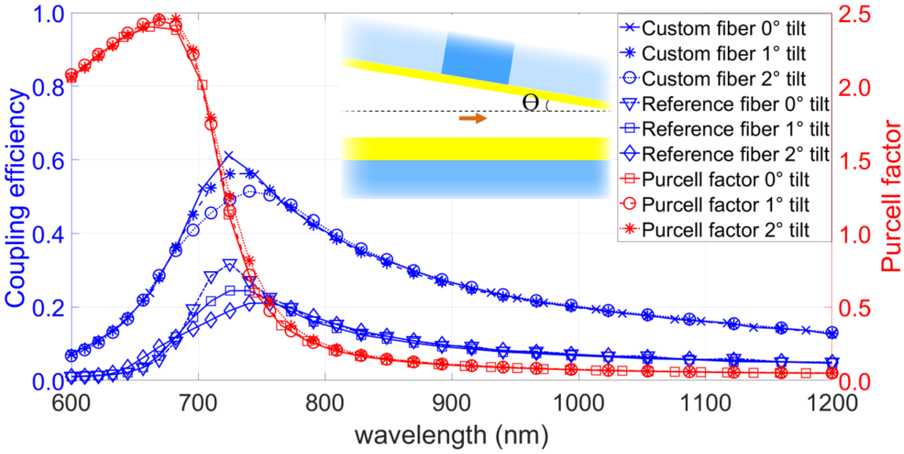

Figure 5.17: The coupling efficiency for the tilted fiber. The custom and reference fibers (Thorlabs "UHNA3") are tilted by 1 degree and afterward by 2 degrees, showing that the coupling is slightly reduced by small tilting. The inset shows the geometry of the tilted fiber. A comparison of custom and reference fiber illustrates that the system is more sensitive to the tiling for larger fiber cores.

Conclusions

Our study proposes novel optical fiber designs in combination with planar Yagi–Uda antennas for the efficient coupling of light with single emitters and nano-objects.

A gold substrate and a thin gold layer (director) on the tip of the fiber increase the power coupled into the fiber up to 1.5 fold more than the total emitted power of the dipole in free space. This is possible due to the combination of Purcell enhancement and antenna effect. Also, the choice of gold should not be seen as a limiting factor. Other materials like silver or aluminum would lead to similar findings. Such large coupling conditions could be obtained by fiber tapering [151], photonic-crystal cladding [170] or by soft glass material [175] to fulfill the critical NA condition. Moreover, a higher fiber core refractive index would increase the coupling efficiency when it is above the critical NA condition. Although the results have been presented for a specific wavelength, they are generally given the scale invariance of Maxwell's equations.

The proposed approach would be particularly attractive for the detection of quantum emitters at interfaces, such as fluorophores in bioassays based on surface chemistry, semiconductor nanocrystals, or fluorescence beads on thin films, and also for the design of efficient single-photon sources. Moreover, the significant coupling efficiency obtained even for micron-scale distances could be exploited for detecting entities like large viruses or bacteria, finding further applications in sensing, diagnostics, and light microscopy.

5.4 Auto-fluorescence and noise of optical fibers

Optical fibers are capable of guiding light with various wavelengths depending on their structure and refractive index. However, the monochromatic light that propagates within the fiber can create a broader spectrum of light, known as auto-fluorescence. This may overlap with the emission wavelength of fluorophores in fiber-based fluorescent imaging, leading to background noise. This background noise can be attributed to three main reasons. Firstly, dopants and impurities can emit unwanted signals. Secondly, Raman scattering can generate a broader spectrum, and thirdly, defects and multiple atomic structural units in amorphous materials such as glass can contribute to background noise.

5.4.1 Emission of dopants and impurities

The main reason for auto-fluorescence in commercial optical fibers is the doped silica material of fiber cores. In order to reduce the loss of fiber, one important aspect is the transparency and refractive index of the material at the working wavelength. This can be achieved by doping different molecules into SiO_2, which normally provide transparent materials with different refractive indices to create a weak waveguide.

However, these molecules often are fluorescent. For example, fiber cores containing Germania (GeO_2) cause electronic defects and color centers associated with the Ge-O bond. If the spectrum of the light, which is coupled into the fiber, overlaps with the excitation of doped molecules, they emit fluorescent light at longer wavelengths due to Stokes shift. In fiber-based fluorescence imaging, this background signal can be problematic if the fiber is used for excitation due to the high power of the excited laser. However, if the fiber is only used to collect the fluorescent light from the sample, the background from the doping or impurities cannot dominate. The auto-fluorescence background can be higher than the fluorescence signal from the sample, and as a result, the SNR is less than one.

To address this problem, one can either employ a pure silica fiber or choose a wavelength that falls outside the excitation range of the dopants. While some background noise may persist in these types of fibers, as discussed in Section 5.4.2 and Section 5.4.3, the overall level of noise can be significantly reduced. Another approach is to introduce a high-power laser (below the fiber's damage threshold) to bleach any fluorescent molecules in the fiber. To achieve this, the fiber must be continuously exposed to the laser for an extended period, typically around three hours, to saturate the fluorophores. The time required may vary depending on the wavelength, doping molecule, and output power of the light [176,177]. This process should be repeated before each experiment.

5.4.2 Raman scattering of silica

Raman scattering is a process whereby the interaction between electromagnetic waves and molecules causes a vibrational transition, which is dependent on the Raman cross-section, light frequency, and the volume of the material. This scattering process leads to a shift in the frequency and wavelength of the scattered light relative to the incident light and can contribute to optical noise in a fiber optic system. While not a fluorescence effect, Raman scattering can be a significant source of background or noise in fiber optic measurements.

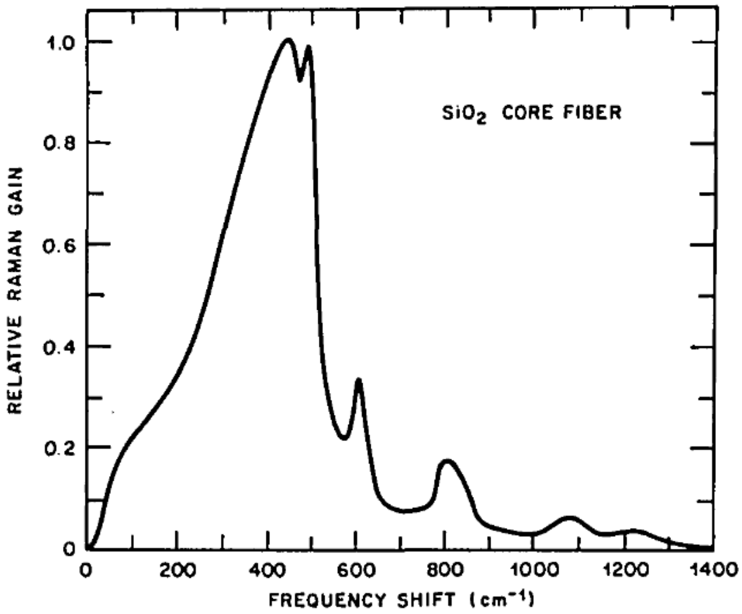

Figure 5.18: ***Raman gain curve of a silica-core single-mode fiber.*** *This curve is normalized to 1.0 at 440 cm^{-1}. Adopted with permission from [178] © Optica Publishing Group.*

In an optical fiber, the light should travel a longer distance inside the core material, and this will increase the chance of spontaneous Raman scattering. Although having a fused silica core fiber without any dopant or impurities reduces the autofluorescence significantly, this has a broad Raman spectrum as shown in Fig. 5.18. The relative Raman gain reaches its peak at around 490 cm^{-1} and then decreases significantly. As a result, the long-pass filters need to be designed with a cutoff wavelength that is no shorter than the point where the relative Raman gain starts to decrease sharply.

The two primary types of commercial fibers used in this chapter are described in detail in Table 5.1. To compare the effect of different source wavelengths on the background noise of the fiber, the SM1500SC was irradiated with laser light at wavelengths of 637 nm, 650 nm, and 690 nm (Fig. 5.19). The SM1500SC fiber fea-

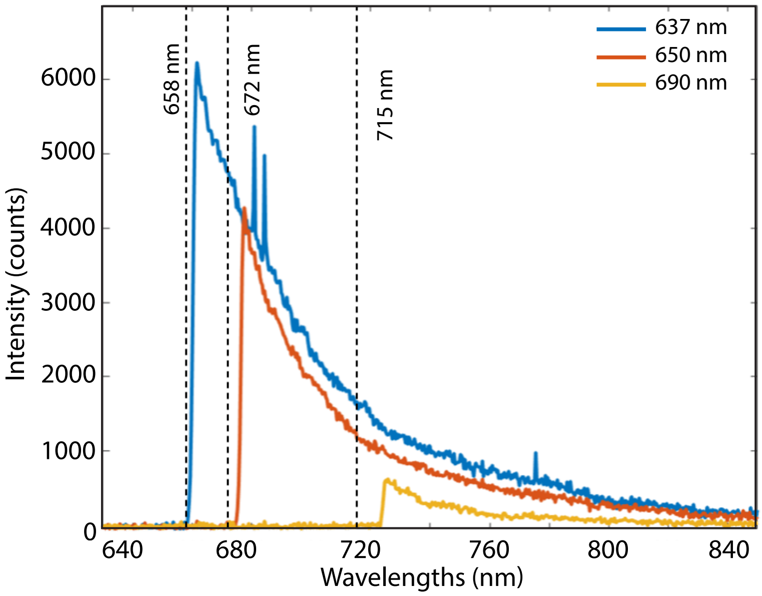

Figure 5.19: ***Background noise of SM1500SC fiber exposed to different light sources.*** *The fiber has pure silica and 54 μW coupling power. Dashed lines represent the maximum Raman scattering at each wavelength. To reduce the Raman effect, long-pass filters are chosen such that the Raman peak is blocked.*

Table 5.1: ***Commercial fibers used in the experiments***

Model	Company	Mode	Working λ	Core size	Core material	NA
SM1500SC	Newport	single	1400-2000 nm	$\sim$ 7 μm	pure silica	$\sim$ 0.17
SM600	Thorlabs	single	633-780 nm	$\sim$ 4.5 μm	Ge-doped	$\sim$ 0.14

tures a core made of pure silica, which helps to minimize auto-fluorescence resulting from dopants (the cladding has a dopant, and the light can weakly excite them via an evanescent field). Therefore, the auto-fluorescence of the fiber in Fig. 5.19 is primarily due to Raman scattering. To avoid the Raman peak, the corresponding wavelength of 490 cm^{-1} is calculated, and the cutoff filters are set after these peaks (dashed line in Fig. 5.19). As presented in Fig. 5.19, longer wavelengths exhibit reduced auto-fluorescence. Consequently, the use of shorter wavelengths for the detection of single molecules with the fiber-based planar antenna sensor is limited due to the higher auto-fluorescence observed.

5.4.3 Defects and atomic structural units of silica

One of the main characteristics of amorphous solids is the lack of regularly repeating groups of atoms, which are native to the crystalline materials [179]. In silica, Si and O atoms can have random structures, as it is shown in Fig. 5.20. Changing molecular structure can provide intermediate energy levels in the molecule. The electrons excited to this energy level will emit fluorescence light after the relaxation.

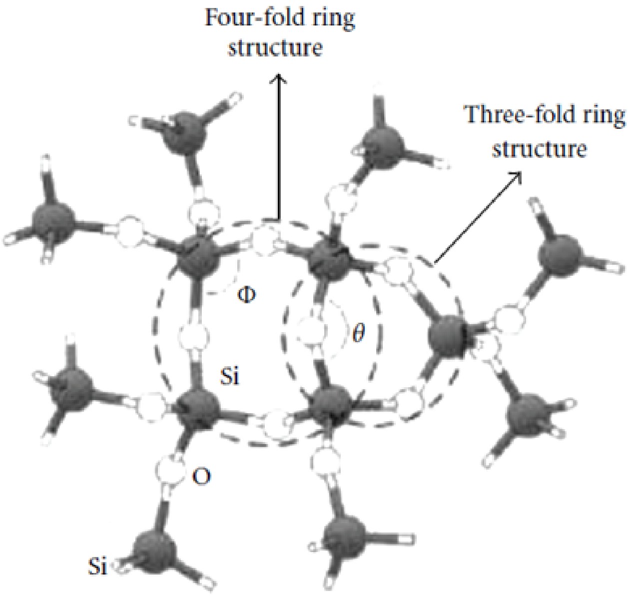

Figure 5.20: ***Ball and stick model of the random network in fused silica.*** *Encircled are three-fold and four-fold ring structures. Adopted with permission from [179] © International Manufacturing Science and Engineering Conference.*

Moreover, defects in fused silica such as laser-induced defects [180] or grinded fused silica [181] can cause fluorescence with different lifetime due to the formation of the Si nanostructures in SiO_2. For example, a green photoluminescence (PL) of oxygen-deficient silica glass when exposed to ultraviolet UV light has a lifetime of 20–30 ns, however green PL band in oxygen-surplus silica glass excited by visible and UV light experiences a lifetime of about 300 ns [182]

5.5 Thinning of optical fiber tips

As mentioned in Sec. 4.2, in order to reach the near-field emission of the emitter, we need a small-sized tip gold wire and for this reason, we etched the wire using HCl. This problem also applies to fiber, which is coated with a metal.

5.5.1 Fiber etching

Creating a small diameter tip (around 5-15 μm) on an optical fiber through etching requires different techniques compared to etching a gold wire. Here, we use hydrofluoric (HF) acid mixed with water (43% HF) as an etchant in the process. First, we remove the acrylate coating of the bare fiber and cleave it using a manual cleaver

(Newport F-CLX-0-3). Then, we vertically dip a few centimeters (1-2cm) of the fiber into the acid for a self-termination process [183]. After the immersion time, the fibers are removed from the HF acid, washed in deionized water, and left to dry in the air.

To understand the etching rate, a batch of six single-mode SM600 fibers is dipped into HF in different time periods, and their diameters are measured using the SEM imaging technique (Fig. 5.21(a)-(d)). The result shows that this process is mainly linear with the etching rate of 4.41µm/min (Fig. 5.21(e)).

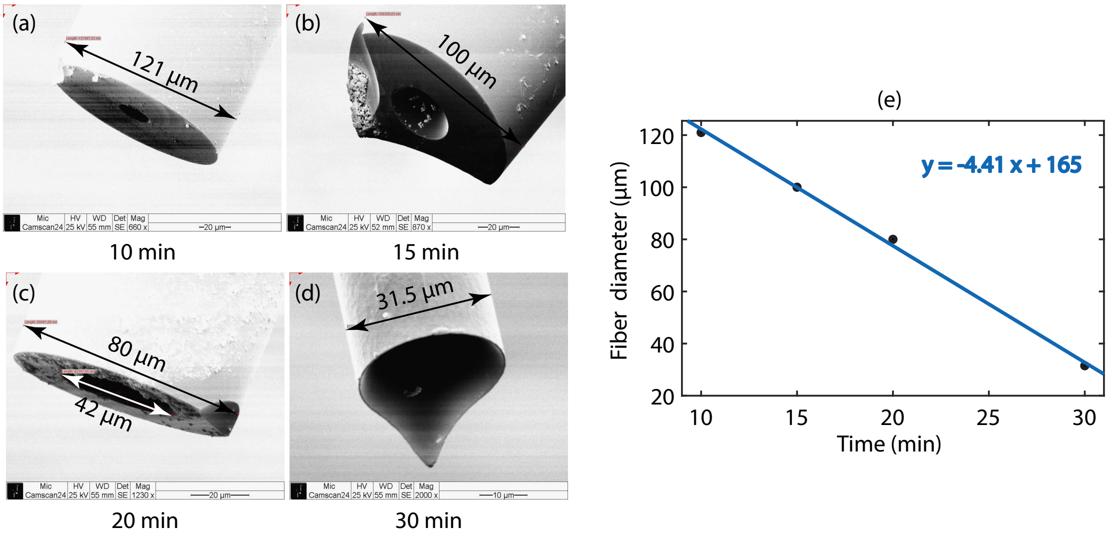

Figure 5.21: ***Time dependency of fiber etching with HF.*** *(a-d) SEM image of the SM600 fibers etched with 43% HF solution for different time periods. Due to the different refractive indices of the core and the cladding, the core is etched faster and forms a hole in the center of the fiber. (e) By fitting the data of fiber diameter and the etching time, one can determine the etching speed.*

By closer look at Fig. 5.21(a)-(d), it becomes apparent that there is a hole located at the center of the fibers. This hole is the result of the cladding and core regions having different etch rates [184]. Although the core and cladding material of SM600 is not given by the company (Thorlabs), the core of SM600 fibers normally contains germanium (Ge) (GeO_2) to a SiO_2 matrix, which can cause a faster etch rate due to weaker bond energy of Ge–O as compared to Si–O [185].

This process can be repeated for the fibers with different core and cladding materials, but the initial guess is the center part is etched faster for single-mode optical fibers in the VIS-NIR range. The reason is either the cores are doped with Ge, which we have already explained, or made of pure silica with a depressed cladding index profile, which means the cladding has two different refractive indices (Fig. 5.22). In the latter case, the inner cladding is normally made of fluorine (F) doped silica, which has a weaker bond energy as compared to pure silica and as a result, this part

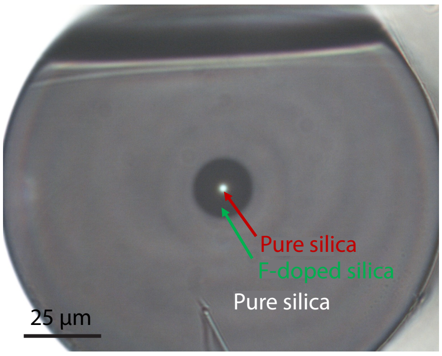

Figure 5.22: ***Cross section of pure silica single mode fiber.*** *A cross-section image of SM1500SC taken by optical microscope. The fiber consists of two claddings, with the inner one made of F-doped silica and the outer one made of pure silica.*

will be etched faster. Since the pure silica core will be more in contact with HF after the F-doped cladding is etched, the core also will be etched before the whole fiber diameter thins down to a few micrometers as we desire.

We also test the fiber etching with HF vapor. In this case, the fiber is located a few millimeters above the HF surface and has no direct contact with HF liquid (Fig. 5.23(a)). While this method may slow down the etching process, it may not entirely prevent the appearance of the center hole in the fiber during HF etching (Fig. 5.23(b)).

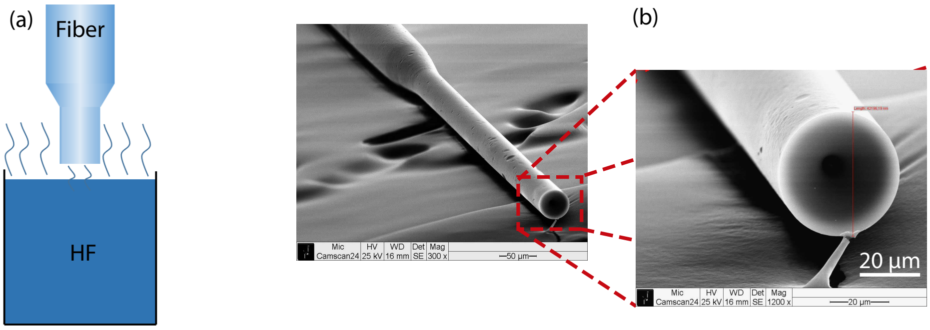

Figure 5.23: ***Etching of optical fiber using HF vapor.*** *(a) The SM600 fiber is located above the HF liquid and the HF vapor etches the fiber. (b) SEM image of the fiber after 60 minutes of vapor exposure. The fiber core is etched with a faster etching rate and forms a hole in the center of the fiber.*

Self-termination etching of glass fibers is a widely used technique for creating fiber tips with controlled geometries. The previous works [183, 186] in fiber etching for near-field spectroscopy show the tip formation in nano-scale. The same method can apply to single-mode fibers and afterward cut the tip with FIB milling in order to provide a flat surface in the range of 5-15 μm and eliminate the center hole.

A common method for achieving an almost homogeneous etching process is by etching the glass fiber at the meniscus between hydrofluoric acid (HF) and an organic overlayer (protecting layer which floats about HF). This approach is illustrated in Fig. 5.24. During the etching process, the fiber diameter is gradually reduced by the etchant, resulting in the formation of a tapered fiber. The taper is created due to the decreasing meniscus height, which is caused by the etching of the fiber. The organic overlayer used in this process can have a significant influence on the resulting tip geometry. The variation of the organic solvent can affect the surface tension at the meniscus and alter the shape of the taper.

It is worth noting that the resulting fiber tip does not necessarily need to be very fine, as it will be milled afterward. However, the taper's angle and length must be carefully controlled to ensure optimal milling conditions and achieve the desired final tip geometry. The process is highly selective, and the etch rate can be controlled by adjusting the concentration of the HF solution and the temperature. After a certain time, the etching process will stop due to a lack of contact between the HF and the fiber. Therefore, there is a minimum etching time required in this process. However, if the etching process continues for a longer period, there is not a significant effect on the shape of the fiber tip.

We submerged a single-mode SM600 fiber into a 43% solution of HF, with an organic oil overlayer (any organic oil is acceptable), for a depth of 3 cm. After approximately 80 minutes, the process halted automatically due to the lack of contact between the fiber and the HF. The oil layer acted as a barrier against further etching by HF vapor, preserving the fiber. This method produces a sharp tip on the fiber, but to obtain a flat surface, we use FIB milling.

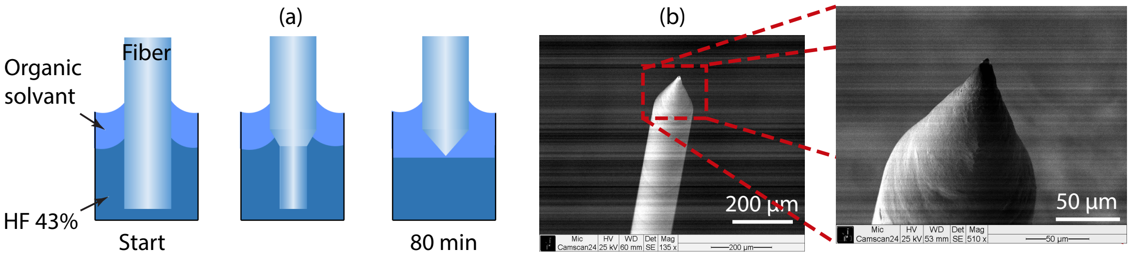

Figure 5.24: ***Self-terminating HF etching process of fiber using organic overlayer.*** *(a) The SM600 fiber is dipped 3 cm into a 43% HF solution with an oil layer on top. After 80 minutes, the fiber is etched into a tapered shape due to the meniscus formed by the HF, oil, and fiber. (b) SEM image of the fiber with a zoomed-in view of the tip of the fiber.*

5.5.2 Fiber tapering

Although finding a solid fiber with high NA and a low auto-fluorescence material (e.g., pure silica) with a small radius is difficult, tapered fiber would be an alternative to gain such a high-performance fiber. Tapering the fiber to the small radius (around 1 μm) can help us to fulfill the core radius and NA requirements for highly efficient coupling. In general, in tapered fiber, the transmission from the untapered part of the fiber to the tip can be very high (more than 95%) in a single-mode fiber. Considering the backward propagation, if the small fiber tip (1 μm radius) provides multimode, only light coupled to the fundamental mode will be transmitted back into the untapered fiber (as this fiber is indeed single mode), once again with 95% efficiency. For multimode fiber, it is possible to have a high forward transmission in case one excites approximately the fundamental mode of the fiber. However, very high-order modes, whose effective index is close to the cladding index, are most likely to be lost along the tapered region. Now, considering backward propagation, in case we make the taper long enough, there is indeed a chance that not only the fundamental mode but also some high-order modes will be transmitted back to the multimode fiber.

However, tapering commercial fibers can be challenging due to the depressed cladding index profile and double-cladding structure of the fiber. The depressed cladding index profile is not usually a concern when the fiber is used in a traditional way (not tapered). However, when the fiber is tapered, the double-cladding structure at the fiber tip creates new optical modes, making it more difficult for light to propagate adiabatically to the fiber core. Achieving an adiabatic transition, in this case, may require impractically long tapering lengths of over a few centimeters.

Furthermore, commercial fibers with a pure silica core typically have a cladding of fluorine-doped (f-doped) silica. When such fibers are tapered, the cladding material forms the tapered part, and this can lead to auto-fluorescence. However, as discussed earlier, this effect can be suppressed by bleaching the doped molecules with high laser power.

Overall, tapering commercial fibers requires careful consideration of these and other factors to achieve the desired results. It may be necessary to experiment with different tapering parameters and techniques to find the best approach for a particular application.

Chapter 6

Outlook: Fiber-based planar antenna sensor

Our current theoretical and experimental advancements have paved the way for the development of a fiber-based sensor utilizing the planar Yagi–Uda antenna. This technology offers highly efficient excitation and collection capabilities, enabling the detection of single molecules through fiber optics. In this chapter, we first explore the excitation and collection of fluorescent beads using a conventional high NA fiber, as well as the issue of auto-fluorescence in core-doped fibers. We then discuss various experimental methods and fiber designs that can enhance the signal-to-noise ratio (SNR) of the fiber. Finally, we introduce a raster scanning approach utilizing a fiber-based planar antenna, which can function as a lensless microscope for fluorescence imaging.

6.1 Excitation and collection with objectives and fibers

As explained in Sec. 5.3, having a fiber with high NA, low core diameter, and low auto-fluorescence in the range of UV-VIS wavelength is challenging. Unfortunately, such a solid core and cladding fiber are not commercially available. In general, the existing fibers either have a high auto-fluorescence or low NA, which reduces the SNR or collection efficiency, respectively. Moreover, adding a gold-coated facet makes the excitation more inefficient due to the high reflection of a gold film and provides more background noise, which causes poor SNR.

By modifying the experimental setup as shown in Fig. 6.1 we are able to measure the emission of fluorescent beads (ThermoFisher, 0.04 μm, dark red fluorescent 660/680) and the auto-fluorescence of the fiber with a high NA objective (Zeiss 0.95 NA air objective) and a single mode fiber (Thorlabs UHNA3) in different configurations. Here, we use a pulsed laser with a fixed 637 nm wavelength (TOPTICA,

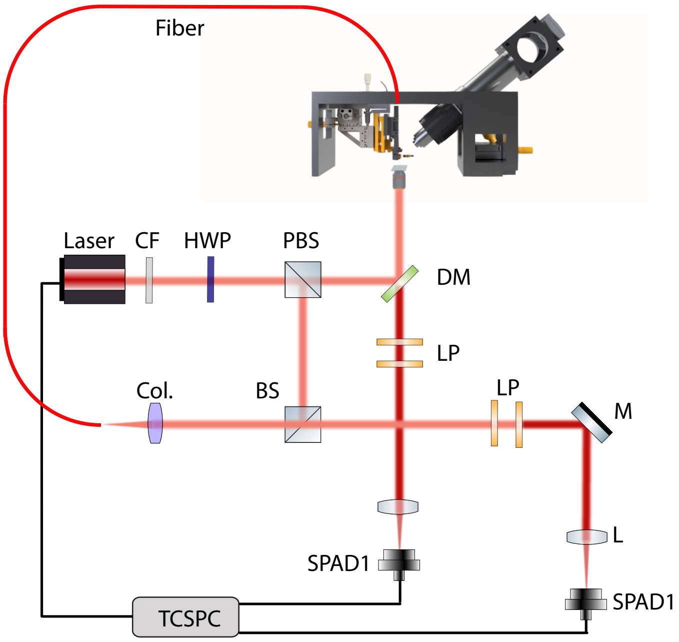

Figure 6.1: ***Excitation and emission with objective and optical fiber.*** *The laser light is divided into two paths by a polarized beam splitter (PBS), where one path is coupled into the objective and the other one coupled into the fiber. This structure enables us to excite or collect with the objective or the fiber. Collimator (Col.), 90:10 beam splitter (BS), half-wave plate (HWP), and long-pass filters (LP) with the cutoff at 675 nm.*

Femtofiber Pro tunable laser) and the previously described setup (Fig.4.7). In this experiment, the sample is excited through the fiber or objective, and the emission light is also collected by the fiber or the objective in 4 different configurations: 1. objective excitation and objective collection. 2. Objective excitation and fiber collection. 3. Fiber excitation and objective collection, and 4. Fiber excitation and fiber collection.

Figure 6.2 compares the detection of a fluorescent bead measured with the setup in Fig. 6.1 for different conditions. Here, in all measurements, the sample is raster scanned with the step size of 200 nm, while the position of the fiber and the objective is fixed. In Fig. 6.2(a)-(b), the bead is excited with the objective, and its emission is also collected via the same objective (inverted microscope configuration). The only difference between Fig. 6.2(a) and (b) is the fiber position. In Fig. 6.2(a), the fiber is completely retracted and located far from the sample. However, in Fig. 6.2(b), the fiber is in the vicinity of the bead ($\sim$800 nm above the glass coverslip). The presence of the fiber provides high background due to the auto-fluorescence of the fiber, and as a result, the SNR changes from 17.7 in Fig. 6.2(a) to 1.6 in Fig. 6.2(b).

Figure 6.2(c),(d) represent the excitation through the objective and collection with the fiber. The excitation power before the microscope in Fig. 6.2(c) is 320 nW, and the SNR is around 1.2. By increasing the excitation power to 6.5 μW in

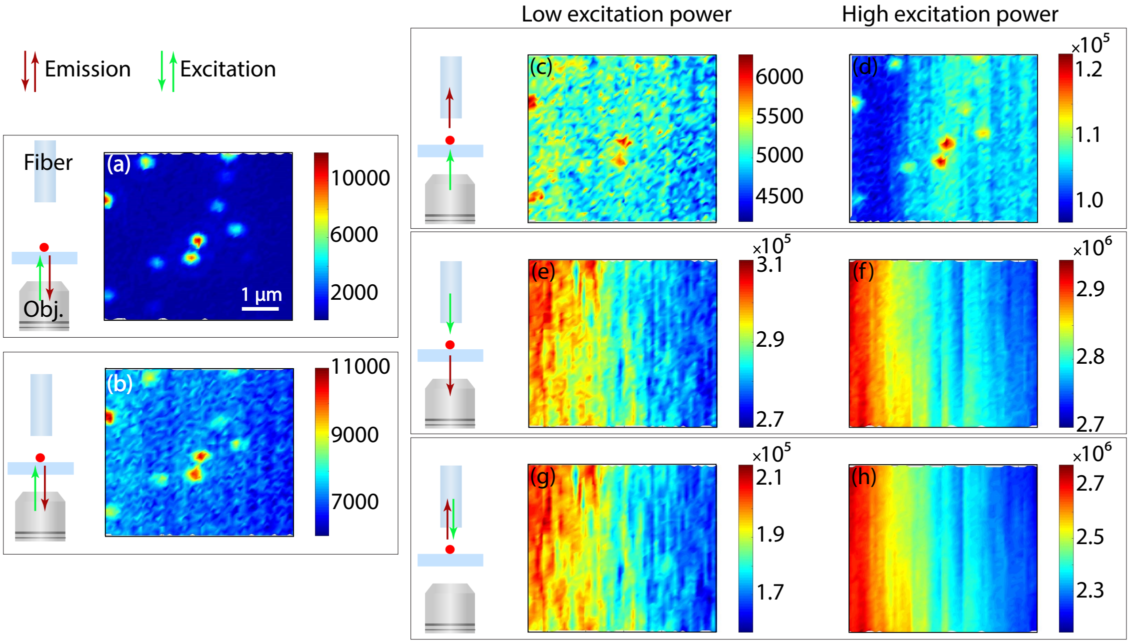

Figure 6.2: ***Different possibilities of excitation and collection with the fiber and the objective.*** *Excitation and emission collection of a fluorescent bead (a) when the optical fiber (UHNA3) is far away from the sample and (b) when the fiber is 800 nm above the glass coverslip substrate. In both cases, the excitation power is 320 nW before the entrance of the microscope. In (c) and (d), the beads are excited through the objective with 320 nW and 6.5 μW power, respectively. The emitted light is collected with the fiber. (e) and (f) show the excitation through the fiber and collection with the objective for 6.5 μW and 70 μW excitation power, respectively. In (g) and (h), both excitation and collection are through the fiber and with excitation powers of 6.5 μW and 70 μW, respectively. In all measurements, the laser wavelength is fixed at 640 nm, and for a better understanding of the figures, the method of excitation and emission is shown in separate boxes.*

Fig. 6.2(d), the SNR slightly increases and is equal to 1.3.

When the sample is excited through the fiber, whether the fluorescence signal is collected by the objective or the fiber itself (Fig. 6.2(e)-(h)), the background of the fiber is dominant due to auto-fluorescence. As a result, detection of the beads is not possible even with high excitation power due to poor SNR (Fig. 6.2(f,h)).

It is important to highlight that the distance between the fiber and the coverslip is around 800 nm in the closest distance, which is 5 fold larger than the antenna distance. The reason is we use an unetched fiber, which has a 125 μm tip diameter. As described before, a small tilt prevents the central part of such a fiber from reaching effective reflector-director distances. However, as it is presented in Fig. 5.9, the collection efficiency by a fiber without a director is almost constant when the distance changes. If the distance is in the antenna configuration range, then the raster scanning is challenging due to the system vibration and the probability of collision between the fiber and the substrate. This issue is further explained in

Sec. 6.5.

6.2 Single molecule detection using time tagging and FLIM

The results of the previous section clearly demonstrate that excitation of the sample through a core-doped fiber causes a very poor SNR. If the emission range of the fiber's auto-fluorescence does not overlap with the sample, it can be easily blocked by an optical bandpass filer. However, mostly the auto-fluorescence has a broad spectrum, and it is not easy to suppress it (see Sec. 5.4).

One method to overcome this problem is using the time tagging signal. With a time tagging signal, one can modify the detection scheme such that the detectors only collect photons in a specific time interval. This helps us to ignore auto-fluorescence photons, which have longer or shorter lifetimes than the fluorescence signal from our sample. However, if the dopant or impurity in the fiber has a lifetime close to the sample it is again difficult to distinguish them.

Another method is using deconvolution in signal post-processing. This method distinguishes the signal from the background (as mentioned in Sec. 4.2) and can be used in fluorescent lifetime imaging microscopy (FLIM) when the sample is raster scanned. However, this method also highly depends on the lifetime of dopant molecules inside the fiber and the doping concentration. Moreover, measuring the lifetime is normally far slower than measuring only the intensity, which turns this method into a slow way of detection, especially in biosensing.

Using optical fibers with pure silica core, which have a lower auto-fluorescent background, can enhance SNR. On the other hand, these fibers normally have lower NA. As mentioned in Sec. 5.3, they have low collection efficiencies (around 16% for 0.17 NA), which can be problematic in sensing a weak signal.

6.3 Excitation via objective

As mentioned earlier, auto-fluorescence is a common issue when using fiber excitation in samples. To overcome this problem, a practical approach is to use a partially transparent reflector and excite the molecules with the microscope objective, rather than the fiber, thereby reducing fiber auto-fluorescence (Fig. 6.3(a)). The reflector with 50 nm gold thickness has 2% transparency, which is enough to excite a molecule on top. As previously stated, a thicker layer of gold also exhibits reduced auto-fluorescence.

The surface plasmon polariton effect represents an alternative approach for exciting the molecules located below the fiber tip, as shown in Fig. 6.3(b). In this method, the focusing light on the gold stripes generates SPP, which can excite the

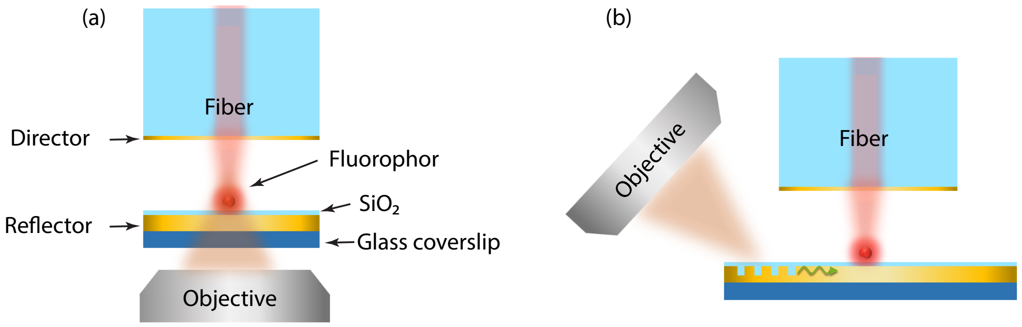

Figure 6.3: ***Fiber-based planar antenna with external molecule excitation.*** *(a) Excitation of fluorescent molecules through a partially transparent reflector (e.g., 50 nm thick gold with 2% transparency) using an inverted microscope objective. (b) SPP excitation of the molecules using gold stripes and tilted objective.*

molecule under the fiber. Afterward, fiber can collect the emission without any auto-fluorescence caused by a high-power excitation light. It is worth mentioning that due to the small distance between the reflector and the director, it is impossible to excite the molecules between them with high-angled excitation.

However, excitation with objective causes more complexity and cost to the setup, but if one uses surface plasmon polariton as mentioned in Fig. 6.3(b), there is no need for high-quality objective or well-focused light.

6.4 Designing high-NA fiber

The possibility to fabricate custom fibers is essential to obtain fiber-based antennas with the highest collection efficiency. Our collaborator at Max Planck Institute for the Science of Light (MPL) fabricates single-mode fibers with high NA and a small fiber tip by tapering a commercial fiber.

A single mode fiber (Newport F-SM1500SC-7/125) with a mode field diameter of 6.7 μm at 1550 nm is tapered down to 2 μm diameter at the fiber tip. The tapered part is about 2 cm long. However, in our work, the spectral range is in VIS-NIR; this fiber still counts as a single-mode fiber. After tapering, the fiber should be cut with FIB. Therefore, it should be coated with a conducting surface (gold) for FIB milling (some FIB devices work with a dielectric material as well). Although we were unable to continue the process due to technical difficulties and timing constraints, it is still feasible to produce a high-quality fiber.

One of the difficulties is, since the core and the cladding merge together in the tapered part of the fiber, the light can easily couple into the thin gold surface on the fiber and dissipate immediately. To overcome this, one can cover the fiber tip by dipping it into the liquid PVA (Polyvinyl alcohol) to form a thin soluble layer.

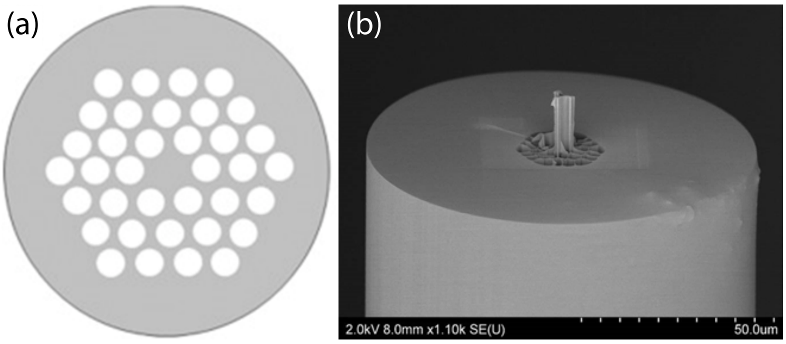

Figure 6.4: ***Photonic crystal cladding fiber with protruding solid core.*** *(a) Optical fiber with circular photonic crystal cladding structure. The holes in the cladding can have any shape as long as they provide a single-mode fiber with high NA. (b) The image of the protruded core fiber.*

Afterward, coat the fiber tip with gold and mill the tip to the desired tip diameter with FIB (as explained for gold wire). Then, again coat the tip of the fiber with titanium and gold to form the director layer, and in the end, remove gold around the tip with a solvent (e.g., water).

Another type of fiber that meets the requirements of a fiber-based Yagi–Uda antenna is the photonic crystal air-cladding fibers (Fig. 6.4). In this fiber, the core protrudes from the cladding, which has the advantage of positioning the fiber in the antenna range (∼100 nm distance from the sample) without etching or tapering the fiber. Moreover, this fiber has very high NA (more than 0.8) [170, 187]

This type of fiber also has the same gold coating problem and needs the same treatment. However, since the protruded core is small, one can cover the tip with a polymer, polish the tip, coat the tip of the core, and remove the residual gold afterward (Fig. 6.5)

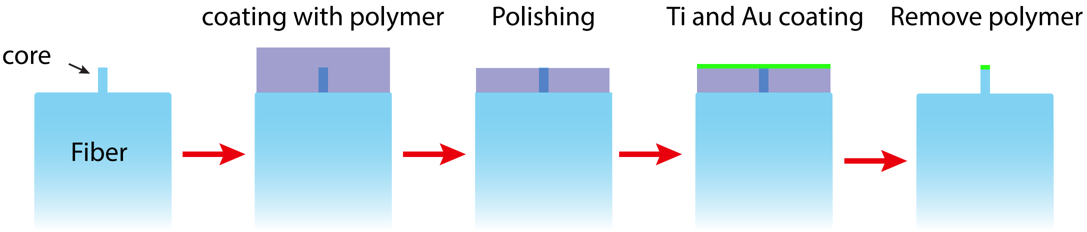

Figure 6.5: ***Coating process of photonic crystal fiber.*** *The coating process of photonic crystal fiber's protruding core with Au. The tip of the fiber is first coated with a polymer (e.g., PVA) such that the protruded core is fully covered. Then the surface is polished till the core is flat and out of polymer. The fiber is coated with Ti and Au in the next step, and finally, the residual gold is removed by dissolving the polymer.*

6.5 Raster scanning of the sample

Detecting a small number of fluorophores in the antenna configuration, whether with objective or fiber, needs a raster scanning technique (Sec. 4.2). The main reason is the small excitation area of the sample. To have an image of the sample and know the position of each molecule, one should scan the whole area step-wise. However, due to mechanical vibrations of the fiber (or wire), keeping the reflector-director distance in the optimal position is difficult. Besides, since this distance is tens of nanometers, it is possible that the fiber contacts with a part of the sample (especially if the peak-to-peak roughness of the sample is higher than the antenna distance) and either moves the sample or breaks the fiber tip.

Therefore, a practical approach is to scan in z-axis with the fiber at each xy position while the sample is raster scanned. In this technique, the fiber moves toward the sample until it contacts the sample and then retracts. The data was collected in both directions. After that, the sample moves one step in the lateral surface using a piezo or motorized stage, and the fiber moves towards the sample again. One could use a tuning fork or an external focused light on the reflector to understand the collision point. When they are in contact, the laser is defocused due to pressure from the fiber. Furthermore, by measuring the lifetime at each point, we can deconvolve the auto-fluorescence background from the fiber by double exponential fitting.

The piezo stack positioner reacts very fast to the applied voltage. Therefore, to avoid long-run measurement, one can write a more efficient program to connect piezo positioners and the APDs using external triggers. This will speed up the experiment and avoid photobleaching of the molecules. This type of lensless microscope has the potential to detect a single fluorescence molecule and helps scientists to determine disease in its early stages.

Chapter 7

Summary and conclusion

Fluorescence detection has emerged as an indispensable tool in the field of biology due to its ability to identify and quantify target molecules with high sensitivity and specificity. This has led to the development of high-performance diagnostic tools that are critical for delivering accurate and timely results in the healthcare system. Despite its utility, the high-performance fluorescence microscope is characterized by its bulky size and high cost. This poses a significant challenge for its adoption and integration into routine clinical practice, particularly in resource-limited settings.

To address this challenge, there have been efforts to miniaturize fluorescence detection technologies. However, downsizing the microscope can lead to decreased sensitivity, lower resolution, and limited detection capabilities, which can compromise its performance. Therefore, achieving a balance between size and performance is crucial in designing next-generation fluorescence detection technologies.

The focus of this work is to build and characterize a compact and sensitive fluorescence detection system, ideally down to a single molecule detection. A critical factor in measuring biological samples is the biocompatibility of the detection system. Therefore, to prevent the organic samples from drying out during the measurement, the proposed system should operate in fluid media. To address this, we introduce and demonstrate a planar optical antenna that enables large sensitivity in reading out dye-labeled bioassays with uncomplicated optics. The key innovation in photonics is the replacement of bulk optics with a photonic chip and a sensor head that utilizes the Yagi–Uda planar antenna concept. This system consists of the fluorescence sample, which is embedded between a reflector and a director element made of metal. Together, they direct fluorescence toward the sensor head, enhancing the limits of detection and improving excitation and emission when the metal surfaces are at the right distance (antenna resonance).

To characterize such a system, we consider the collected power and radiation pattern of the emitted light in relation to the distance between the reflector and the director. To accomplish this, we employ a fluorescence bead as an emitter and measure the radiated power and emission pattern using the back focal plane imaging technique. Our findings indicate that the emitted light exhibits directionality (45°) when the reflector-director distance is at resonance and that the fluorescence power is enhanced 2-3 fold compared to beads emitted on glass coverslips.

Moreover, we translate these findings into a fluorescence-based molecular assay for in-vitro diagnostics. Here, we immobilize ATTO-647N labeled dsDNA molecules with different concentrations in a planar antenna with T50 buffer as an active medium. The results of the directionality and decay rates are similar to the bead measurement. The limitation of our antenna is the detection of 1 nM sample concentration, which corresponds to less than 10 ATTO-647N labeled dsDNA molecules in the focal area. It should also be recalled that the gold auto-fluorescence is the main reason for such a limitation, and it can be largely suppressed by better antenna fabrication.

After reaching the proof of concept, we focus on designing a compact and portable system without requiring the conventional optical microscope. Therefore, we integrate the optical readout functionalities in a low-cost disposable unit by replacing the director with a gold-coated fiber tip. In this configuration, the molecule can be excited through the fiber, and the emission will be coupled into the same fiber afterward. A conventional method to couple laser light (excitation) into a fiber is the free-space fiber coupling, in which a lens coupler focuses the Gaussian beam laser. We derive analytical expressions for a focused Gaussian beam in the paraxial approximation, considering the lens filling factor. The results determine a broadening of the focal spot in a small lens filling factor, which reduces the coupling efficiency of the laser into a fiber with a core size smaller than the focal spot. In theory, the coupling efficiency of a horizontal dipole into a custom fiber is around 70% of the total emitted power. This coupling is 106% of the dipole emission in free space. Exceeding 100% is due to the Purcell enhancement of the molecules in the antenna setup. The coupling efficiency will scale by a factor of 2/3 for emitters with random orientation.

Although the theoretical results are very promising, working with fiber has some challenges, such as auto-fluorescence of the fiber, difficulty in alignment, and fiber manufacturing with special characterizations. We also propose potential methods to overcome these problems as an outlook of the project.

The proposed approach employs a fluorescence detection system, which is highly suitable for the detection of fluorophores in bioassays. By bundling such fibers, the sample can be imaged with a high resolution comparable to the diameter of the fibers.

In addition, the combination of a photo-stable single photon emitter, such as the

NV center, with a fiber-based planar Yagi–Uda antenna offers an efficient approach for designing single-photon sources. Such a system can significantly enhance spectroscopy systems have potential applications in fields such as quantum cryptography, quantum key distribution, and quantum sensing.

Bibliography

[1] K. D. Sattler, *Handbook of nanophysics: nanoparticles and quantum dots*. CRC press, 2016. (Cited on page 1)

[2] N. Taniguchi, "On the basic concept of nano-technology proceedings of the international conference on production engineering tokyo part ii japan society of precision engineering," *Pabbati et al*, 1974. (Cited on page 1)

[3] K. E. Drexler, *Engines of Creation: The Coming Era of Nanotechnology*. Anchor, 1987. (Cited on page 1)

[4] G. Binnig, H. Rohrer, C. Gerber, and E. Weibel, "Tunneling through a controllable vacuum gap," *Applied Physics Letters*, vol. 40, no. 2, pp. 178–180, 1982. (Cited on page 1)

[5] J. Tersoff and D. R. Hamann, "Theory of the scanning tunneling microscope," *Physical Review B*, vol. 31, no. 2, p. 805, 1985. (Cited on page 1)

[6] S. Iijima, "Helical microtubules of graphitic carbon," *nature*, vol. 354, no. 6348, pp. 56–58, 1991. (Cited on page 1)

[7] M. Ono, M. Saito, T. Yoshitomi, C. Fiegna, T. Ohguro, and H. Iwai, "A 40 nm gate length n-mosfet," *IEEE Transactions on Electron Devices*, vol. 42, no. 10, pp. 1822–1830, 1995. (Cited on page 1)

[8] B. Hoefflinger, "Irds—international roadmap for devices and systems, rebooting computing, s3s," *Nano-Chips 2030*, pp. 9–17, 2020. (Cited on page 1)

[9] S. Sargazi, I. Fatima, M. H. Kiani, V. Mohammadzadeh, R. Arshad, M. Bilal, A. Rahdar, A. M. Díez-Pascual, and R. Behzadmehr, "Fluorescent-based nanosensors for selective detection of a wide range of biological macromolecules: A comprehensive review," *International Journal of Biological Macromolecules*, vol. 206, pp. 115–147, 2022. (Cited on page 1)

[10] B. Casse, W. Lu, Y. Huang, E. Gultepe, L. Menon, and S. Sridhar, "Super-resolution imaging using a three-dimensional metamaterials nanolens," *Applied Physics Letters*, vol. 96, no. 2, p. 023114, 2010. (Cited on page 1)

[11] R. Yan, D. Gargas, and P. Yang, “Nanowire photonics,” *Nature Photonics*, vol. 3, no. 10, pp. 569–576, 2009. (Cited on page 1)

[12] V. Giannini, A. I. Fernández-Domínguez, S. C. Heck, and S. A. Maier, “Plasmonic nanoantennas: fundamentals and their use in controlling the radiative properties of nanoemitters,” *Chemical Reviews*, vol. 111, no. 6, pp. 3888–3912, 2011. (Cited on page 1)

[13] P. Biagioni, J.-S. Huang, and B. Hecht, “Nanoantennas for visible and infrared radiation,” *Reports on Progress in Physics*, vol. 75, no. 2, p. 024402, 2012. (Cited on page 1)

[14] C. A. Balanis, “Antenna theory: A review,” *Proceedings of the IEEE*, vol. 80, no. 1, pp. 7–23, 1992. (Cited on page 1)

[15] M. Agio and A. Alù, *Optical antennas.* Cambridge University Press, 2013. (Cited on page 2)

[16] H. F. Hofmann, T. Kosako, and Y. Kadoya, “Design parameters for a nano-optical yagi–uda antenna,” *New Journal of Physics*, vol. 9, no. 7, p. 217, 2007. (Cited on page 2)

[17] K. J. Vahala, “Optical microcavities,” *Nature*, vol. 424, no. 6950, pp. 839–846, 2003. (Cited on page 2)

[18] W. Chen, Ş. Kaya Özdemir, G. Zhao, J. Wiersig, and L. Yang, “Exceptional points enhance sensing in an optical microcavity,” *Nature*, vol. 548, no. 7666, pp. 192–196, 2017. (Cited on page 2)

[19] T. H. Taminiau, F. D. Stefani, and N. F. van Hulst, “Enhanced directional excitation and emission of single emitters by a nano-optical yagi-uda antenna,” *Optics Express*, vol. 16, no. 14, pp. 10858–10866, 2008. (Cited on pages 2 and 47)

[20] S. Lobanov, T. Weiss, D. Dregely, H. Giessen, N. Gippius, and S. Tikhodeev, “Emission properties of an oscillating point dipole from a gold yagi-uda nanoantenna array,” *Physical Review B*, vol. 85, no. 15, p. 155137, 2012. (Cited on page 2)

[21] L. Novotny and N. Van Hulst, “Antennas for light,” *Nature Photonics*, vol. 5, no. 2, pp. 83–90, 2011. (Cited on pages 2, 30 and 67)

[22] S. Checcucci, P. Lombardi, S. Rizvi, F. Sgrignuoli, N. Gruhler, F. B. Dieleman, F. S. Cataliotti, W. H. Pernice, M. Agio, and C. Toninelli, “Beaming light from a quantum emitter with a planar optical antenna,” *Light: Science &*

Applications, vol. 6, no. 4, pp. e16245–e16245, 2017. (Cited on pages 2, 37, 39, 46, 47, 54, 67, 69, 77, 97, 98, 99, 102 and 105)

[23] H. Galal, A. M. Flatae, S. Lagomarsino, G. Schulte, C. Wild, E. Wörner, N. Gelli, S. Sciortino, H. Schönherr, L. Giuntini, *et al.*, “Highly efficient light extraction and directional emission from diamond color centers using planar yagi-uda antennas,” *arXiv preprint arXiv:1905.03363*, 2019. (Cited on pages 2 and 46)

[24] N. Soltani, E. R. Esfahany, S. I. Druzhinin, G. Schulte, J. Müller, B. Butz, H. Schönherr, M. Agio, and N. Markešević, “Biosensing with a scanning planar yagi-uda antenna,” *Biomedical optics Express*, vol. 13, no. 2, pp. 539–548, 2022. (Cited on page 2)

[25] J. R. Lakowicz, *Principles of fluorescence spectroscopy.* Springer Science & Business Media, 2013. (Cited on pages 6, 9 and 13)

[26] G. L. Miessler and D. Tarr, *Inorganic Chemistry.* Pearson Education, Inc, 2013. (Cited on page 6)

[27] M. Agio, *Molecular scattering and fluorescence in strongly confined optical fields: spectroscopy, sensing and signal processing.* PhD thesis, Eidgenössische Technische Hochschule Zürich, Laboratorium für Physikalische ..., 2011. (Cited on pages 6, 7, 8, 24, 26 and 30)

[28] A. Hughes, “Zero-phonon transitions and vibrational structure,” *Le Journal de Physique Colloques*, vol. 28, no. C4, pp. C4–55, 1967. (Cited on page 8)

[29] ATTO-TEC GmbH, “specification of ATTO647N dye molecule.” `https://www.atto-tec.com/fileadmin/user_upload/Katalog_Flyer_Support/ATTO_647N.pdf`, 2021. Accessed: 2021-03-19. (Cited on page 11)

[30] C. J. Breshike, R. A. Riskowski, and G. F. Strouse, “Leaving forster resonance energy transfer behind: nanometal surface energy transfer predicts the size-enhanced energy coupling between a metal nanoparticle and an emitting dipole,” *The Journal of Physical Chemistry C*, vol. 117, no. 45, pp. 23942–23949, 2013. (Cited on page 13)

[31] M. Wachsmuth, “Molecular diffusion and binding analyzed with frap,” *Protoplasma*, vol. 251, no. 2, pp. 373–382, 2014. (Cited on page 15)

[32] H. F. Arnoldus and J. T. Foley, “Transmission of dipole radiation through interfaces and the phenomenon of anti-critical angles,” *JOSA A*, vol. 21, no. 6, pp. 1109–1117, 2004. (Cited on page 18)

[33] L. Novotny and B. Hecht, *Principles of Nano-Optics*. Cambridge, UK: Cambridge University Press, second ed., 2012. (Cited on pages 18, 20, 24, 32, 84, 89 and 90)

[34] J. Klohs, A. Wunder, and K. Licha, “Near-infrared fluorescent probes for imaging vascular pathophysiology,” *Basic Research in Cardiology*, vol. 103, no. 2, pp. 144–151, 2008. (Cited on page 19)

[35] C. R. Kagan, E. Lifshitz, E. H. Sargent, and D. V. Talapin, “Building devices from colloidal quantum dots,” *Science*, vol. 353, no. 6302, p. aac5523, 2016. (Cited on page 21)

[36] M. A. Reed, “Quantum dots,” *Scientific American*, vol. 268, no. 1, pp. 118–123, 1993. (Cited on page 20)

[37] Y. Guo, Z. Wang, H. Shao, and X. Jiang, “Hydrothermal synthesis of highly fluorescent carbon nanoparticles from sodium citrate and their use for the detection of mercury ions,” *Carbon*, vol. 52, pp. 583–589, 2013. (Cited on page 21)

[38] D. Bu, H. Zhuang, G. Yang, and X. Ping, “An immunosensor designed for polybrominated biphenyl detection based on fluorescence resonance energy transfer (fret) between carbon dots and gold nanoparticles,” *Sensors and Actuators B: Chemical*, vol. 195, pp. 540–548, 2014. (Cited on page 21)

[39] A. Litvin, I. Martynenko, F. Purcell-Milton, A. Baranov, A. Fedorov, and Y. Gun’Ko, “Colloidal quantum dots for optoelectronics,” *Journal of Materials Chemistry A*, vol. 5, no. 26, pp. 13252–13275, 2017. (Cited on page 21)

[40] L. Childress and R. Hanson, “Diamond nv centers for quantum computing and quantum networks,” *MRS bulletin*, vol. 38, no. 2, pp. 134–138, 2013. (Cited on page 21)

[41] J. Wang, F. Feng, J. Zhang, J. Chen, Z. Zheng, L. Guo, W. Zhang, X. Song, G. Guo, L. Fan, *et al.*, “High-sensitivity temperature sensing using an implanted single nitrogen-vacancy center array in diamond,” *Physical Review B*, vol. 91, no. 15, p. 155404, 2015. (Cited on page 21)

[42] J. M. Higbie, J. D. Perreault, V. M. Acosta, C. Belthangady, P. Lebel, M. H. Kim, K. Nguyen, V. Demas, V. Bajaj, and C. Santori, “Multiphoton-excited fluorescence of silicon-vacancy color centers in diamond,” *Physical Review Applied*, vol. 7, no. 5, p. 054010, 2017. (Cited on page 22)

[43] A. Gali and J. R. Maze, "Ab initio study of the split silicon-vacancy defect in diamond: Electronic structure and related properties," *Physical Review B*, vol. 88, no. 23, p. 235205, 2013. (Cited on page 22)

[44] C. Bradac, T. Gaebel, N. Naidoo, M. Sellars, J. Twamley, L. Brown, A. Barnard, T. Plakhotnik, A. Zvyagin, and J. Rabeau, "Observation and control of blinking nitrogen-vacancy centres in discrete nanodiamonds," *Nature nanotechnology*, vol. 5, no. 5, pp. 345–349, 2010. (Cited on page 22)

[45] U. Jantzen, A. B. Kurz, D. S. Rudnicki, C. Schäfermeier, K. D. Jahnke, U. L. Andersen, V. A. Davydov, V. N. Agafonov, A. Kubanek, L. J. Rogers, *et al.*, "Nanodiamonds carrying silicon-vacancy quantum emitters with almost lifetime-limited linewidths," *New Journal of Physics*, vol. 18, no. 7, p. 073036, 2016. (Cited on page 22)

[46] K. Q. da Costa, G. T. C. de Sousa, P. R. Amaral, J. L. Souza, T. D. S. Garcia, and P. N. dos Santos, "Wireless optical nanolinks with yagi-uda and dipoles plasmonic nanoantennas," in *Nanoplasmonics*, IntechOpen, 2019. (Cited on page 24)

[47] A. Mohammadi, F. Kaminski, V. Sandoghdar, and M. Agio, "Spheroidal nanoparticles as nanoantennas for fluorescence enhancement," *International journal of nanotechnology*, vol. 6, no. 10-11, pp. 902–914, 2009. (Cited on page 25)

[48] R. P. Zaccaria, A. Alabastri, F. De Angelis, G. Das, C. Liberale, A. Toma, A. Giugni, L. Razzari, M. Malerba, H. B. Sun, *et al.*, "Fully analytical description of adiabatic compression in dissipative polaritonic structures," *Physical Review B*, vol. 86, no. 3, p. 035410, 2012. (Cited on page 25)

[49] C. A. Balanis, *Antenna theory: analysis and design.* John wiley & sons, 2015. (Cited on page 25)

[50] T. Hanke, J. Cesar, V. Knittel, A. Trugler, U. Hohenester, A. Leitenstorfer, and R. Bratschitsch, "Tailoring spatiotemporal light confinement in single plasmonic nanoantennas," *Nano letters*, vol. 12, no. 2, pp. 992–996, 2012. (Cited on page 25)

[51] K. Tanabe, "Field enhancement around metal nanoparticles and nanoshells: a systematic investigation," *The Journal of Physical Chemistry C*, vol. 112, no. 40, pp. 15721–15728, 2008. (Cited on page 25)

[52] Y. Xu, R. K. Lee, and A. Yariv, "Quantum analysis and the classical analysis of spontaneous emission in a microcavity," *Physical review A*, vol. 61, no. 3, p. 033807, 2000. (Cited on page 26)

[53] M. A. Lieb, J. M. Zavislan, and L. Novotny, "Single-molecule orientations determined by direct emission pattern imaging," *JOSA B*, vol. 21, no. 6, pp. 1210–1215, 2004. (Cited on page 28)

[54] J. Enderlein, T. Ruckstuhl, and S. Seeger, "Highly efficient optical detection of surface-generated fluorescence," *Applied Optics*, vol. 38, no. 4, pp. 724–732, 1999. (Cited on pages 29 and 34)

[55] H. Yagi, "Beam transmission of ultra short waves," *Proceedings of the Institute of Radio Engineers*, vol. 16, no. 6, pp. 715–740, 1928. (Cited on page 30)

[56] T. Kosako, Y. Kadoya, and H. F. Hofmann, "Directional control of light by a nano-optical yagi–uda antenna," *Nature Photonics*, vol. 4, no. 5, pp. 312–315, 2010. (Cited on page 30)

[57] T. Kosako, *Study on Optical Yagi-Uda Antennas Utilizing Localized Surface Plasmon Resonance of Metal Nanoparticles*. PhD thesis, (Hiroshima University), 2016. (Cited on page 30)

[58] X.-L. Chu, T. J. Brenner, X.-W. Chen, Y. Ghosh, J. Hollingsworth, V. Sandoghdar, and S. Götzinger, "Experimental realization of an optical antenna designed for collecting 99% of photons from a quantum emitter," *Optica*, vol. 1, no. 4, pp. 203–208, 2014. (Cited on pages 31, 37, 46, 55 and 61)

[59] K. A. Neyts, "Simulation of light emission from thin-film microcavities," *JOSA A*, vol. 15, no. 4, pp. 962–971, 1998. (Cited on pages 33 and 47)

[60] X.-L. Chu, *Collecting photons with near-unity efficiency using a dielectric antenna*. PhD thesis, Friedrich-Alexander-Universität Erlangen-Nürnberg (FAU), 2019. (Cited on page 33)

[61] L. Gao, F. Lemarchand, and M. Lequime, "Comparison of different dispersion models for single layer optical thin film index determination," *Thin Solid Films*, vol. 520, no. 1, pp. 501–509, 2011. (Cited on page 36)

[62] H. Galal and M. Agio, "Highly efficient light extraction and directional emission from large refractive-index materials with a planar yagi-uda antenna," *Optical Materials Express*, vol. 7, no. 5, pp. 1634–1646, 2017. (Cited on pages 38, 40, 46, 97, 98 and 107)

[63] A. Drechsler, M. Lieb, C. Debus, A. J. Meixner, and G. Tarrach, “Confocal microscopy with a high numerical aperture parabolic mirror,” *Optics Express*, vol. 9, no. 12, pp. 637–644, 2001. (Cited on page 45)

[64] J. Enderlein, “Theoretical study of detection of a dipole emitter through an objective with high numerical aperture,” *Optics Letters*, vol. 25, no. 9, pp. 634–636, 2000. (Cited on page 45)

[65] H. Kaupp, T. Hümmer, M. Mader, B. Schlederer, J. Benedikter, P. Haeusser, H.-C. Chang, H. Fedder, T. W. Hänsch, and D. Hunger, “Purcell-enhanced single-photon emission from nitrogen-vacancy centers coupled to a tunable microcavity,” *Physical Review Applied*, vol. 6, no. 5, p. 054010, 2016. (Cited on pages 45, 96 and 98)

[66] H. A. Huckabay and R. C. Dunn, “Whispering gallery mode imaging for the multiplexed detection of biomarkers,” *Sensors and Actuators B: Chemical*, vol. 160, no. 1, pp. 1262–1267, 2011. (Cited on page 45)

[67] J. Claudon, J. Bleuse, N. S. Malik, M. Bazin, P. Jaffrennou, N. Gregersen, C. Sauvan, P. Lalanne, and J.-M. Gérard, “A highly efficient single-photon source based on a quantum dot in a photonic nanowire,” *Nature Photonics*, vol. 4, no. 3, pp. 174–177, 2010. (Cited on pages 45 and 96)

[68] T. M. Babinec, B. J. Hausmann, M. Khan, Y. Zhang, J. R. Maze, P. R. Hemmer, and M. Lončar, “A diamond nanowire single-photon source,” *Nature Nanotechnology*, vol. 5, no. 3, pp. 195–199, 2010. (Cited on page 45)

[69] A. Kinkhabwala, Z. Yu, S. Fan, Y. Avlasevich, K. Müllen, and W. Moerner, “Large single-molecule fluorescence enhancements produced by a bowtie nanoantenna,” *Nature Photonics*, vol. 3, no. 11, pp. 654–657, 2009. (Cited on page 45)

[70] L. Langguth, A. Szuba, S. A. Mann, E. C. Garnett, G. H. Koenderink, and A. F. Koenderink, “Nano-antenna enhanced two-focus fluorescence correlation spectroscopy,” *Scientific Reports*, vol. 7, no. 1, pp. 1–9, 2017. (Cited on page 45)

[71] K. J. Russell, T.-L. Liu, S. Cui, and E. L. Hu, “Large spontaneous emission enhancement in plasmonic nanocavities,” *Nature Photonics*, vol. 6, no. 7, pp. 459–462, 2012. (Cited on page 45)

[72] H. Sugimoto, S. Yashima, and M. Fujii, “Hybridized plasmonic gap mode of gold nanorod on mirror nanoantenna for spectrally tailored fluorescence enhancement,” *ACS Photonics*, vol. 5, no. 8, pp. 3421–3427, 2018. (Cited on page 45)

[73] S. Bidault, A. Devilez, V. Maillard, L. Lermusiaux, J.-M. Guigner, N. Bonod, and J. Wenger, "Picosecond lifetimes with high quantum yields from single-photon-emitting colloidal nanostructures at room temperature," *ACS Nano*, vol. 10, no. 4, pp. 4806–4815, 2016. (Cited on page 45)

[74] V. Flauraud, R. Regmi, P. M. Winkler, D. T. Alexander, H. Rigneault, N. F. van Hulst, M. F. García-Parajo, J. Wenger, and J. Brugger, "In-plane plasmonic antenna arrays with surface nanogaps for giant fluorescence enhancement," *Nano Letters*, vol. 17, no. 3, pp. 1703–1710, 2017. (Cited on pages 45 and 67)

[75] G. Acuna, F. Möller, P. Holzmeister, S. Beater, B. Lalkens, and P. Tinnefeld, "Fluorescence enhancement at docking sites of dna-directed self-assembled nanoantennas," *Science*, vol. 338, no. 6106, pp. 506–510, 2012. (Cited on page 45)

[76] X. Lu, G. Ye, D. Punj, R. C. Chiechi, and M. Orrit, "Quantum yield limits for the detection of single-molecule fluorescence enhancement by a gold nanorod," *ACS Photonics*, vol. 7, no. 9, pp. 2498–2505, 2020. (Cited on page 45)

[77] H. Aouani, O. Mahboub, N. Bonod, E. Devaux, E. Popov, H. Rigneault, T. W. Ebbesen, and J. Wenger, "Bright unidirectional fluorescence emission of molecules in a nanoaperture with plasmonic corrugations," *Nano Letters*, vol. 11, no. 2, pp. 637–644, 2011. (Cited on pages 45 and 67)

[78] G. M. Akselrod, C. Argyropoulos, T. B. Hoang, C. Ciracì, C. Fang, J. Huang, D. R. Smith, and M. H. Mikkelsen, "Probing the mechanisms of large purcell enhancement in plasmonic nanoantennas," *Nature Photonics*, vol. 8, no. 11, pp. 835–840, 2014. (Cited on page 45)

[79] S. Xia, T. Aoki, K. Gao, M. Arita, Y. Arakawa, and M. J. Holmes, "Enhanced single-photon emission from gan quantum dots in bullseye structures," *ACS Photonics*, 2021. (Cited on page 45)

[80] S. Kühn, G. Mori, M. Agio, and V. Sandoghdar, "Modification of single molecule fluorescence close to a nanostructure: radiation pattern, spontaneous emission and quenching," *Molecular Physics*, vol. 106, no. 7, pp. 893–908, 2008. (Cited on pages 45 and 67)

[81] A. G. Curto, G. Volpe, T. H. Taminiau, M. P. Kreuzer, R. Quidant, and N. F. van Hulst, "Unidirectional emission of a quantum dot coupled to a nanoantenna," *Science*, vol. 329, no. 5994, pp. 930–933, 2010. (Cited on pages 45 and 67)

[82] K. G. Lee, X. Chen, H. Eghlidi, P. Kukura, R. Lettow, A. Renn, V. Sandoghdar, and S. Götzinger, "A planar dielectric antenna for directional single-photon emission and near-unity collection efficiency," *Nature Photonics*, vol. 5, no. 3, pp. 166–169, 2011. (Cited on page 46)

[83] J. Miguel-Sánchez, A. Reinhard, E. Togan, T. Volz, A. Imamoglu, B. Besga, J. Reichel, and J. Estève, "Cavity quantum electrodynamics with charge-controlled quantum dots coupled to a fiber fabry–perot cavity," *New Journal of Physics*, vol. 15, no. 4, p. 045002, 2013. (Cited on page 46)

[84] H. Kelkar, D. Wang, D. Martín-Cano, B. Hoffmann, S. Christiansen, S. Götzinger, and V. Sandoghdar, "Sensing nanoparticles with a cantilever-based scannable optical cavity of low finesse and sub-λ 3 volume," *Physical Review Applied*, vol. 4, no. 5, p. 054010, 2015. (Cited on pages 46 and 57)

[85] D. Wang, H. Kelkar, D. Martin-Cano, D. Rattenbacher, A. Shkarin, T. Utikal, S. Götzinger, and V. Sandoghdar, "Turning a molecule into a coherent two-level quantum system," *Nature Physics*, vol. 15, no. 5, pp. 483–489, 2019. (Cited on page 46)

[86] B. Casabone, J. Benedikter, T. Hümmer, F. Oehl, K. de Oliveira Lima, T. W. Hänsch, A. Ferrier, P. Goldner, H. de Riedmatten, and D. Hunger, "Cavity-enhanced spectroscopy of a few-ion ensemble in eu^{3+}: Y$_2$o$_3$," *New Journal of Physics*, vol. 20, no. 9, p. 095006, 2018. (Cited on page 46)

[87] N. Soltani and M. Agio, "Planar antenna designs for efficient coupling between a single emitter and an optical fiber," *Optics Express*, vol. 27, no. 21, pp. 30830–30841, 2019. (Cited on pages 46, 47, 57 and 77)

[88] L. V. Rodríguez-de Marcos, J. I. Larruquert, J. A. Méndez, and J. A. Aznárez, "Self-consistent optical constants of sio$_2$ and ta$_2$o$_5$ films," *Optical Materials Express*, vol. 6, no. 11, pp. 3622–3637, 2016. (Cited on page 47)

[89] F. Kaminski, V. Sandoghdar, and M. Agio, "Finite-difference time-domain modeling of decay rates in the near field of metal nanostructures," *Journal of Computational and Theoretical nanoscience*, vol. 4, no. 3, pp. 635–643, 2007. (Cited on page 47)

[90] *Lumerical Inc. FDTD Solutions, Verion: 8.19.1541 and MODE Solutions, Version: 7.12.1731 (2018).* Vancouver, Canada, 2018. Verion: 8.19.1541. (Cited on pages 47, 97 and 101)

[91] R. Chance, A. Prock, and R. Silbey, "Molecular fluorescence and energy transfer near interfaces," *Advances in Chemical Physics*, vol. 37, pp. 1–65, 1978. (Cited on pages 49 and 54)

[92] W. S. Werner, K. Glantschnig, and C. Ambrosch-Draxl, "Optical constants and inelastic electron-scattering data for 17 elemental metals," *Journal of Physical and Chemical Reference Data*, vol. 38, no. 4, pp. 1013–1092, 2009. (Cited on pages 50 and 100)

[93] R. L. Olmon, B. Slovick, T. W. Johnson, D. Shelton, S.-H. Oh, G. D. Boreman, and M. B. Raschke, "Optical dielectric function of gold," *Physical Review B*, vol. 86, no. 23, p. 235147, 2012. (Cited on page 50)

[94] H. Sun, M. Yu, G. Wang, X. Sun, and J. Lian, "Temperature-dependent morphology evolution and surface plasmon absorption of ultrathin gold island films," *The Journal of Physical Chemistry C*, vol. 116, no. 16, pp. 9000–9008, 2012. (Cited on pages 50 and 79)

[95] B. Ren, G. Picardi, and B. Pettinger, "Preparation of gold tips suitable for tip-enhanced raman spectroscopy and light emission by electrochemical etching," *Review of Scientific Instruments*, vol. 75, no. 4, pp. 837–841, 2004. (Cited on page 51)

[96] B. Buchler, T. Kalkbrenner, C. Hettich, and V. Sandoghdar, "Measuring the quantum efficiency of the optical emission of single radiating dipoles using a scanning mirror," *Physical Review Letters*, vol. 95, no. 6, p. 063003, 2005. (Cited on pages 54 and 62)

[97] L. Zhu, D. Zhang, R. Wang, X. Wen, P. Wang, H. Ming, R. Badugu, and J. R. Lakowicz, "Out-of-focal plane imaging by leakage radiation microscopy," *Journal of Optics*, vol. 19, no. 9, p. 095004, 2017. (Cited on page 55)

[98] M. Brunstein, A. Salomon, and M. Oheim, "Decoding the information contained in fluorophore radiation patterns," *ACS Nano*, vol. 12, no. 12, pp. 11725–11730, 2018. (Cited on page 55)

[99] A. Dasgupta, J. Deschamps, U. Matti, U. Hübner, J. Becker, S. Strauss, R. Jungmann, R. Heintzmann, and J. Ries, "Direct supercritical angle localization microscopy for nanometer 3d superresolution," *Nature Communications*, vol. 12, no. 1, pp. 1–9, 2021. (Cited on page 55)

[100] A. Devilez, B. Stout, and N. Bonod, "Compact metallo-dielectric optical antenna for ultra directional and enhanced radiative emission," *ACS Nano*, vol. 4, no. 6, pp. 3390–3396, 2010. (Cited on pages 55 and 61)

[101] Y. Colombe, T. Steinmetz, G. Dubois, F. Linke, D. Hunger, and J. Reichel, “Strong atom–field coupling for bose–einstein condensates in an optical cavity on a chip,” *Nature*, vol. 450, no. 7167, pp. 272–276, 2007. (Cited on page 57)

[102] C. Toninelli, Y. Delley, T. Stöferle, A. Renn, S. Götzinger, and V. Sandoghdar, “A scanning microcavity for in situ control of single-molecule emission,” *Applied Physics Letters*, vol. 97, no. 2, p. 021107, 2010. (Cited on page 57)

[103] O. S. Wolfbeis, “Materials for fluorescence-based optical chemical sensors,” *Journal of Materials Chemistry*, vol. 15, no. 27-28, pp. 2657–2669, 2005. (Cited on page 58)

[104] J. Benedikter, H. Kaupp, T. Hümmer, Y. Liang, A. Bommer, C. Becher, A. Krueger, J. M. Smith, T. W. Hänsch, and D. Hunger, “Cavity-enhanced single-photon source based on the silicon-vacancy center in diamond,” *Physical Review Applied*, vol. 7, no. 2, p. 024031, 2017. (Cited on page 58)

[105] G. Gagliardi and H.-P. Loock, eds., *Cavity-enhanced spectroscopy and sensing*. Springer, 2014. (Cited on page 58)

[106] D. Shotton and N. White, “Confocal scanning microscopy: three-dimensional biological imaging,” *Trends in Biochemical Sciences*, vol. 14, no. 11, pp. 435–439, 1989. (Cited on page 58)

[107] K. Santra, J. Zhan, X. Song, E. A. Smith, N. Vaswani, and J. W. Petrich, “What is the best method to fit time-resolved data? a comparison of the residual minimization and the maximum likelihood techniques as applied to experimental time-correlated, single-photon counting data,” *The Journal of Physical Chemistry B*, vol. 120, no. 9, pp. 2484–2490, 2016. (Cited on page 60)

[108] A. Grinvald and I. Z. Steinberg, “On the analysis of fluorescence decay kinetics by the method of least-squares,” *Analytical biochemistry*, vol. 59, no. 2, pp. 583–598, 1974. (Cited on page 60)

[109] V. Logeeswaran, M.-L. Chan, Y. Bayam, M. S. Islam, D. Horsley, X. Li, W. Wu, S. Wang, and R. Williams, “Ultra-smooth metal surfaces generated by pressure-induced surface deformation of thin metal films,” *Applied Physics A*, vol. 87, no. 2, pp. 187–192, 2007. (Cited on page 61)

[110] A. L. Mattheyses and D. Axelrod, “Fluorescence emission patterns near glass and metal-coated surfaces investigated with back focal plane imaging,” *Journal of Biomedical Optics*, vol. 10, no. 5, p. 054007, 2005. (Cited on page 62)

[111] A. J. Haes, L. Chang, W. L. Klein, and R. P. Van Duyne, "Detection of a biomarker for Alzheimer's disease from synthetic and clinical samples using a nanoscale optical biosensor," *Journal of the American Chemical Society*, vol. 127, no. 7, pp. 2264–2271, 2005. (Cited on page 67)

[112] Y. Lu, S. Peng, D. Luo, and A. Lal, "Low-concentration mechanical biosensor based on a photonic crystal nanowire array," *Nature Communications*, vol. 2, no. 1, pp. 1–6, 2011. (Cited on page 67)

[113] S. M. Borisov and O. S. Wolfbeis, "Optical biosensors," *Chemical Reviews*, vol. 108, no. 2, pp. 423–461, 2008. (Cited on page 67)

[114] I. Kucherenko, O. Soldatkin, D. Y. Kucherenko, O. Soldatkina, and S. Dzyadevych, "Advances in nanomaterial application in enzyme-based electrochemical biosensors: A review," *Nanoscale Advances*, vol. 1, no. 12, pp. 4560–4577, 2019. (Cited on page 67)

[115] E. Mauriz and L. M. Lechuga, "Plasmonic biosensors for single-molecule biomedical analysis," *Biosensors*, vol. 11, no. 4, p. 123, 2021. (Cited on page 67)

[116] S. Handschuh-Wang, T. Wang, S. I. Druzhinin, D. Wesner, X. Jiang, and H. Schönherr, "Detailed study of BSA adsorption on micro-and nanocrystalline diamond/β-sic composite gradient films by time-resolved fluorescence microscopy," *Langmuir*, vol. 33, no. 3, pp. 802–813, 2017. (Cited on page 67)

[117] S. Firdous, S. Anwar, and R. Rafya, "Development of surface plasmon resonance (SPR) biosensors for use in the diagnostics of malignant and infectious diseases," *Laser Physics Letters*, vol. 15, no. 6, p. 065602, 2018. (Cited on page 67)

[118] P. Zijlstra, P. M. Paulo, and M. Orrit, "Optical detection of single non-absorbing molecules using the surface plasmon resonance of a gold nanorod," *Nature Nanotechnology*, vol. 7, no. 6, pp. 379–382, 2012. (Cited on page 67)

[119] G. Qiu, Z. Gai, Y. Tao, J. Schmitt, G. A. Kullak-Ublick, and J. Wang, "Dual-functional plasmonic photothermal biosensors for highly accurate severe acute respiratory syndrome coronavirus 2 detection," *ACS Nano*, vol. 14, no. 5, pp. 5268–5277, 2020. (Cited on page 67)

[120] S. Laing, L. E. Jamieson, K. Faulds, and D. Graham, "Surface-enhanced Raman spectroscopy for in vivo biosensing," *Nature Reviews Chemistry*, vol. 1, no. 8, pp. 1–19, 2017. (Cited on page 67)

[121] M. A. Ettabib, A. Marti, Z. Liu, B. M. Bowden, M. N. Zervas, P. N. Bartlett, and J. S. Wilkinson, "Waveguide enhanced Raman spectroscopy for biosensing: A review," *ACS Sensors*, 2021. (Cited on page 67)

[122] Y. Guo, H. Li, K. Reddy, H. S. Shelar, V. R. Nittoor, and X. Fan, "Optofluidic Fabry–Pérot cavity biosensor with integrated flow-through micro-/nanochannels," *Applied Physics Letters*, vol. 98, no. 4, p. 041104, 2011. (Cited on page 67)

[123] A. Portela, O. Calvo-Lozano, M.-C. Estevez, A. M. Escuela, and L. M. Lechuga, "Optical nanogap antennas as plasmonic biosensors for the detection of miRNA biomarkers," *Journal of Materials Chemistry B*, vol. 8, no. 19, pp. 4310–4317, 2020. (Cited on page 67)

[124] J. Larkin, R. Y. Henley, V. Jadhav, J. Korlach, and M. Wanunu, "Length-independent DNA packing into nanopore zero-mode waveguides for low-input DNA sequencing," *Nature Nanotechnology*, vol. 12, no. 12, pp. 1169–1175, 2017. (Cited on page 67)

[125] A. P. Demchenko, "Photobleaching of organic fluorophores: quantitative characterization, mechanisms, protection," *Methods and applications in fluorescence*, vol. 8, no. 2, p. 022001, 2020. (Cited on page 67)

[126] N. Soltani, E. Rabbany Esfahany, S. I Druzhinin, G. Schulte, J. Müller, B. Butz, H. Schönherr, N. Markešević, and M. Agio, "Scanning planar Yagi–Uda antenna for fluorescence detection," *Journal of the Optical Society of America B*, vol. 38, no. 9, pp. 2528–2535, 2021. (Cited on pages 68, 70, 71, 73, 76 and 80)

[127] M. P. Busson, B. Rolly, B. Stout, N. Bonod, and S. Bidault, "Accelerated single photon emission from dye molecule-driven nanoantennas assembled on DNA," *Nature Communications*, vol. 3, no. 1, pp. 1–6, 2012. (Cited on page 68)

[128] B. M. Reinhard, S. Sheikholeslami, A. Mastroianni, A. P. Alivisatos, and J. Liphardt, "Use of plasmon coupling to reveal the dynamics of DNA bending and cleavage by single EcoRV restriction enzymes," *Proceedings of the National Academy of Sciences*, vol. 104, no. 8, pp. 2667–2672, 2007. (Cited on pages 69 and 79)

[129] M. P. Busson, B. Rolly, B. Stout, N. Bonod, E. Larquet, A. Polman, and S. Bidault, "Optical and topological characterization of gold nanoparticle dimers linked by a single DNA double strand," *Nano Letters*, vol. 11, no. 11, pp. 5060–5065, 2011. (Cited on pages 69 and 79)

[130] S. Ernst, D. M. Irber, A. M. Waeber, G. Braunbeck, and F. Reinhard, “A planar scanning probe microscope,” *ACS Photonics*, vol. 6, no. 2, pp. 327–331, 2019. (Cited on page 70)

[131] P. E. Lombardi, A. E. Giannetti, P. Cecchi, F. E. Chiavaioli, S. Howitz, N. Soltani, F. Sonntag, C. Toninelli, and M. Agio, “Sepsis biomarker detection through lensless fiber-based planar antennas,” in *Optical Sensors 2021*, vol. 11772, p. 117720N, International Society for Optics and Photonics, 2021. (Cited on page 77)

[132] A. Giannetti, P. Cecchi, F. Chiavaioli, S. Howitz, P. Lombardi, N. Soltani, F. Sonntag, C. Toninelli, and M. Agio, “Sepsis biomarker detection through fiber-based planar antennas (conference presentation),” in *Biophotonics in Point-of-Care*, vol. 11361, p. 113610Q, International Society for Optics and Photonics, 2020. (Cited on page 77)

[133] A. Mooradian, “Photoluminescence of metals,” *Physical Review Letters*, vol. 22, no. 5, p. 185, 1969. (Cited on page 79)

[134] B. E. Saleh and M. C. Teich, *Fundamentals of photonics*. john Wiley & sons, 2019. (Cited on page 86)

[135] M. Born and E. Wolf, *Principles of Optics*. Cambridge, UK: Cambridge University Press, seventh (expanded) ed., 1999. (Cited on page 89)

[136] B. Richards and E. Wolf, “Electromagnetic Diffraction in Optical Systems. II. Structure of the Image Field in an Aplanatic System,” *Proc. Royal Soc. London A*, vol. 253, no. 1274, pp. 358–379, 1959. (Cited on pages 89 and 90)

[137] C. J. R. Sheppard and P. Török, “Efficient calculation of electromagnetic diffraction in optical systems using a multipole expansion,” *J. Mod. Opt.*, vol. 44, pp. 803–818, Apr. 1997. Publisher: TAYLOR & FRANCIS LTD. (Cited on page 89)

[138] C. J. R. Sheppard and K. G. Larkin, “Optimal Concentration of Electromagnetic Radiation,” *J. Mod. Opt.*, vol. 41, no. 7, pp. 1495–1505, 1994. Publisher: Taylor & Francis. (Cited on page 89)

[139] S. Arisa, H. Endo, M. Sasaki, Y. Takayama, R. Shimizu, and M. Fujiwara, “Coupling efficiency of laser beam to multimode fiber for free space optical communication,” in *International Conference on Space Optics — ICSO 2014* (B. Cugny, Z. Sodnik, and N. Karafolas, eds.), (Tenerife, Canary Islands, Spain), p. 162, SPIE, Nov. 2017. (Cited on page 89)

[140] O. E. Olarte, J. Andilla, E. J. Gualda, and P. Loza-Alvarez, "Light-sheet microscopy: a tutorial," *Advances in Optics and Photonics*, vol. 10, p. 111, Mar. 2018. (Cited on page 89)

[141] S. Mishra and V. Yadava, "Laser Beam MicroMachining (LBMM) – A review," *Optics and Lasers in Engineering*, vol. 73, pp. 89–122, Oct. 2015. (Cited on page 89)

[142] M. Abramowitz and I. A. Stegun, eds., *Handbook of mathematical functions*. New York: Dover, tenth ed., 1972. (Cited on pages 90 and 91)

[143] A. W. Snyder and J. Love, *Optical waveguide theory*. Springer Science & Business Media, 2012. (Cited on pages 96 and 98)

[144] O. Kahl, S. Ferrari, V. Kovalyuk, G. N. Goltsman, A. Korneev, and W. H. Pernice, "Waveguide integrated superconducting single-photon detectors with high internal quantum efficiency at telecom wavelengths," *Scientific Reports*, vol. 5, p. 10941, 2015. (Cited on page 96)

[145] B. Schmidt, V. Almeida, C. Manolatou, S. Preble, and M. Lipson, "Nanocavity in a silicon waveguide for ultrasensitive nanoparticle detection," *Applied Physics Letters*, vol. 85, no. 21, pp. 4854–4856, 2004. (Cited on page 96)

[146] S. A. Maier, P. G. Kik, H. A. Atwater, S. Meltzer, E. Harel, B. E. Koel, and A. A. Requicha, "Local detection of electromagnetic energy transport below the diffraction limit in metal nanoparticle plasmon waveguides," *Nature Materials*, vol. 2, no. 4, p. 229, 2003. (Cited on page 96)

[147] H. Mukundan, A. Anderson, W. K. Grace, K. Grace, N. Hartman, J. Martinez, and B. Swanson, "Waveguide-based biosensors for pathogen detection," *Sensors*, vol. 9, no. 7, pp. 5783–5809, 2009. (Cited on page 96)

[148] N. Verhart, G. Lepert, A. Billing, J. Hwang, and E. Hinds, "Single dipole evanescently coupled to a multimode waveguide," *Optics Express*, vol. 22, no. 16, pp. 19633–19640, 2014. (Cited on pages 96 and 103)

[149] M. I. Davanco and K. Srinivasan, "An efficient, optical fiber-based waveguide interface to a single quantum dipole," in *Frontiers in Optics*, p. FMG2, Optical Society of America, 2009. (Cited on page 96)

[150] M. Fujiwara, K. Toubaru, T. Noda, H.-Q. Zhao, and S. Takeuchi, "Highly efficient coupling of photons from nanoemitters into single-mode optical fibers," *Nano letters*, vol. 11, no. 10, pp. 4362–4365, 2011. (Cited on page 96)

[151] S. Chonan, S. Kato, and T. Aoki, “Efficient single-mode photon-coupling device utilizing a nanofiber tip,” *Scientific Reports*, vol. 4, p. 4785, 2014. (Cited on pages 96, 97 and 108)

[152] P. Then, G. Razinskas, T. Feichtner, P. Haas, A. Wild, N. Bellini, R. Osellame, G. Cerullo, and B. Hecht, “Remote detection of single emitters via optical waveguides,” *Physical Review A*, vol. 89, no. 5, p. 053801, 2014. (Cited on page 96)

[153] K. Kurihara, H. Ohkawa, Y. Iwasaki, O. Niwa, T. Tobita, and K. Suzuki, “Fiber-optic conical microsensors for surface plasmon resonance using chemically etched single-mode fiber,” *Analytica Chimica Acta*, vol. 523, no. 2, pp. 165–170, 2004. (Cited on page 96)

[154] T. Schröder, M. Fujiwara, T. Noda, H.-Q. Zhao, O. Benson, and S. Takeuchi, “A nanodiamond-tapered fiber system with high single-mode coupling efficiency,” *Optics Express*, vol. 20, no. 10, pp. 10490–10497, 2012. (Cited on page 96)

[155] R. A. Lieberman, L. Blyler, and L. G. Cohen, “A distributed fiber optic sensor based on cladding fluorescence,” *Journal of Lightwave Technology*, vol. 8, no. 2, pp. 212–220, 1990. (Cited on page 96)

[156] M. Davanço and K. Srinivasan, “Efficient spectroscopy of single embedded emitters using optical fiber taper waveguides,” *Optics Express*, vol. 17, no. 13, pp. 10542–10563, 2009. (Cited on page 96)

[157] M. Davanço and K. Srinivasan, “Fiber-coupled semiconductor waveguides as an efficient optical interface to a single quantum dipole,” *Optics Letters*, vol. 34, no. 16, pp. 2542–2544, 2009. (Cited on page 96)

[158] L. Liebermeister, F. Petersen, A. v. Münchow, D. Burchardt, J. Hermelbracht, T. Tashima, A. W. Schell, O. Benson, T. Meinhardt, A. Krueger, A. Stiebeiner, A. Rauschenbeutel, H. Weinfurter, and M. Weber, “Tapered fiber coupling of single photons emitted by a deterministically positioned single nitrogen vacancy center,” *Applied Physics Letters*, vol. 104, no. 3, p. 031101, 2014. (Cited on page 96)

[159] R. S. Daveau, K. C. Balram, T. Pregnolato, J. Liu, E. H. Lee, J. D. Song, V. Verma, R. Mirin, S. W. Nam, L. Midolo, S. Stobbe, K. Srinivasan, and P. Lodahl, “Efficient fiber-coupled single-photon source based on quantum dots in a photonic-crystal waveguide,” *Optica*, vol. 4, no. 2, pp. 178–184, 2017. (Cited on page 96)

[160] J. Li, A. Salandrino, and N. Engheta, “Shaping light beams in the nanometer scale: A yagi-uda nanoantenna in the optical domain,” *Physical Review B*, vol. 76, no. 24, p. 245403, 2007. (Cited on page 97)

[161] J. Homola, *Surface Plasmon Resonance Based Sensors*, vol. 4. Springer, 2006. (Cited on page 97)

[162] A. Taflove and S. C. Hagness, *Computational electrodynamics: the finite-difference time-domain method.* Artech house, 2005. (Cited on page 97)

[163] W. L. Stutzman and G. A. Thiele, *Antenna theory and design.* John Wiley & Sons, 2013. (Cited on page 97)

[164] S. Lagomarsino, A. M. Flatae, S. Sciortino, F. Gorelli, M. Santoro, F. Tantussi, F. De Angelis, N. Gelli, F. Taccetti, L. Giuntini, and M. Agio, “Optical properties of silicon-vacancy color centers in diamond created by ion implantation and post-annealing,” *Diamond and Related Materials*, vol. 84, pp. 196–203, 2018. (Cited on page 100)

[165] A. M. Flatae, F. Tantussi, G. C. Messina, A. Mohammadi, F. De Angelis, and M. Agio, “Plasmonic gold nanocones in the near-infrared for quantum nano-optics,” *Advanced Optical Materials*, vol. 5, no. 22, p. 1700586, 2017. (Cited on page 100)

[166] X. Gao, Y. Cui, R. M. Levenson, L. W. Chung, and S. Nie, “In vivo cancer targeting and imaging with semiconductor quantum dots,” *Nature Biotechnology*, vol. 22, no. 8, p. 969, 2004. (Cited on page 100)

[167] J. Love and W. Henry, “Quantifying loss minimisation in single-mode fibre tapers,” *Electronics Letters*, vol. 22, no. 17, pp. 912–914, 1986. (Cited on page 100)

[168] S. Ravets, J. Hoffman, P. Kordell, J. Wong-Campos, S. Rolston, and L. Orozco, “Intermodal energy transfer in a tapered optical fiber: optimizing transmission,” *JOSA A*, vol. 30, no. 11, pp. 2361–2371, 2013. (Cited on page 100)

[169] R. Nagai and T. Aoki, “Ultra-low-loss tapered optical fibers with minimal lengths,” *Optics Express*, vol. 22, no. 23, pp. 28427–28436, 2014. (Cited on page 100)

[170] W. J. Wadsworth, R. M. Percival, G. Bouwmans, J. C. Knight, T. A. Birks, T. D. Hedley, and P. S. J. Russell, “Very high numerical aperture fibers,” *IEEE Photonics Technology Letters*, vol. 16, no. 3, pp. 843–845, 2004. (Cited on pages 100, 109 and 124)

[171] B. E. Saleh, M. C. Teich, and B. E. Saleh, *Fundamentals of photonics*, vol. 22. Wiley, 1991. (Cited on page 102)

[172] D. Cadeddu, J. Teissier, F. R. Braakman, N. Gregersen, P. Stepanov, J.-M. Gérard, J. Claudon, R. J. Warburton, M. Poggio, and M. Munsch, "A fiber-coupled quantum-dot on a photonic tip," *Applied Physics Letters*, vol. 108, no. 1, p. 011112, 2016. (Cited on page 105)

[173] A. Schlehahn, S. Fischbach, R. Schmidt, A. Kaganskiy, A. Strittmatter, S. Rodt, T. Heindel, and S. Reitzenstein, "A stand-alone fiber-coupled single-photon source," *Scientific Reports*, vol. 8, no. 1, p. 1340, 2018. (Cited on page 105)

[174] J. Li, A. Salandrino, and N. Engheta, "Optical spectrometer at the nanoscale using optical yagi-uda nanoantennas," *Physical Review B*, vol. 79, no. 19, p. 195104, 2009. (Cited on page 105)

[175] E. Snitzer and R. Tumminelli, "Sio 2-clad fibers with selectively volatilized soft-glass cores," *Optics Letters*, vol. 14, no. 14, pp. 757–759, 1989. (Cited on page 109)

[176] E. J. Friebele and M. E. Gingerich, "Photobleaching effects in optical fiber waveguides," *Applied Optics*, vol. 20, no. 19, pp. 3448–3452, 1981. (Cited on page 110)

[177] G. Sigel, E. Friebele, M. Marrone, and M. Gingerich, "An analysis of photobleaching techniques for the radiation hardening of fiber optic data links," *IEEE Transactions on Nuclear Science*, vol. 28, no. 6, pp. 4095–4101, 1981. (Cited on page 110)

[178] R. H. Stolen, C. Lee, and R. Jain, "Development of the stimulated raman spectrum in single-mode silica fibers," *JOSA B*, vol. 1, no. 4, pp. 652–657, 1984. (Cited on page 111)

[179] S. Vukelic, B. Gao, S. Ryu, and Y. Yao, "Structural modification of amorphous fused silica under femtosecond laser irradiation," in *International Manufacturing Science and Engineering Conference*, vol. 48517, pp. 227–236, 2008. (Cited on pages 112 and 113)

[180] H. Zhang, Z. Yuan, J. Zhou, J. Dong, Y. Wei, and Q. Lou, "Laser-induced fluorescence of fused silica irradiated by arf excimer laser," *Journal of Applied Physics*, vol. 110, no. 1, p. 013107, 2011. (Cited on page 113)

[181] J. Neauport, P. Cormont, P. Legros, C. Ambard, and J. Destribats, "Imaging subsurface damage of grinded fused silica optics by confocal fluorescence microscopy," *Optics Express*, vol. 17, no. 5, pp. 3543–3554, 2009. (Cited on page 113)

[182] Y. Sakurai and K. Nagasawa, "Green photoluminescence band in γ-irradiated oxygen-surplus silica glass," *Journal of Applied Physics*, vol. 86, no. 3, pp. 1377–1381, 1999. (Cited on page 113)

[183] A. Sayah, C. Philipona, P. Lambelet, M. Pfeffer, and F. Marquis-Weible, "Fiber tips for scanning near-field optical microscopy fabricated by normal and reverse etching," *Ultramicroscopy*, vol. 71, no. 1-4, pp. 59–63, 1998. (Cited on pages 114 and 115)

[184] C. J. Tuck, R. Hague, and C. Doyle, "Low cost optical fibre based fabry–perot strain sensor production," *Measurement Science and Technology*, vol. 17, no. 8, p. 2206, 2006. (Cited on page 114)

[185] R. C. Weast, M. Astle, and W. Beyer, "Crc handbook of chemistry and physics, ed," *WH Beyer (Boca Baton, FL: Chemical Rubber Company Press, 1999)*, pp. 12–192, 1982. (Cited on page 114)

[186] R. Stöckle, C. Fokas, V. Deckert, R. Zenobi, B. Sick, B. Hecht, and U. P. Wild, "High-quality near-field optical probes by tube etching," *Applied Physics Letters*, vol. 75, no. 2, pp. 160–162, 1999. (Cited on page 115)

[187] W. Wadsworth, R. Percival, G. Bouwmans, J. Knight, , and P. S. J. Russell, "High power air-clad photonic crystal fibre laser," *Optics Express*, vol. 11, no. 1, pp. 48–53, 2003. (Cited on page 124)